Drying and Cracking Behavior of Aqueous Particulate Coatings

A THESIS
SUBMITTED TO THE FACULTY OF THE GRADUATE SCHOOL
OF THE UNIVERSITY OF MINNESOTA
BY

Yan Wu

IN PARTIAL FULFILLMENT OF THE REQUIREMENTS
FOR THE DEGREE OF
DOCTOR OF PHILOSOPHY

Lorraine Francis, Advisor

March, 2018

Acknowledgements

I would like to thank many people who helped me during the past six years of graduate school and made my time at the University of Minnesota rewarding and memorable. It is their support that brought me where I am today and made this work possible.

I would like to thank my advisor, Prof. Lorraine Francis, for her continued guidance, patience and constant encouragement. Lorraine provided me with invaluable insight and great freedom through my study, which gave me the solid support to move forward and explore my research projects with different directions and scopes. Her enthusiasm and academic rigor had profoundly influenced my research attitude and taught me how to be a qualified researcher. Acknowledgements also go out to the Coating Process Fundamentals Programs (CPFP) of the Industrial Partnership for Research in Interfacial and Materials Engineering (IPRIME) at the University of Minnesota and AAA for the financial support. I would also like to thank Gary Fugitt with WestRock company, for the contribution and support throughout these research projects.

I am fortunate to have the opportunity to interact with so many talented and fantastic people during the past years. I specifically would like to thank Dr. Kyle Price for the hands-on help and inspiring suggestions of my research. Also, I would like to sincerely thank the help from Chris Frethem and Hanseung Lee for the training and assistance of all those long days working on CryoSEM imaging. Wieslaw Suszynski, who always has solutions to my request of experiment design, thank you for all the CAD designs, equipment trainings and apparatus buildup. I also would like to acknowledge Prof. Satish Kumar and Prof. Alon McCormick for useful suggestions to my projects, Dr. David Giles and Dr. James Marti for the training and support on rheology and particle analysis, Michelle Smeaton for teaching me nano-particle synthesis, and all current members and alumni in my research groups, including Motao Cao, Yuyang Du,

Noah Holzman, Woo Jin Hyun, Krystopher Jochem, Alex Jordan, Alireza Mohammad Karim, Bob Lade, Tuoqi Li, Sooman Lim, Ankit Mahajan, Vincent Pang, Kyle Price, Bryce Williams, Dennis Wagner, Jyun-Ting Wu, Heng Zhang, and Wanlu Zhang, thank you for all of your contributed ideas and and help.

Finally, I would like to thank my friends and family, without your love and support I never would have made it here. Yiming, special thanks to you for being such a wonderful friend and sticking by me through so many ups and downs. Tuoqi, Lian, Qile, Jun, Yuyang, En, Hongyun, Tianqi, Motao, Weihua, Boxin, Xueshun and Jarron. I am gratefully to know all of you, and thank you for adding tremendous joy and happiness in my life. Mom and Dad, you deserve my deepest acknowledgement, thank you for always supporting me and believing me.

Abstract

The goal of this work is to understand the connections between stress, structural and mechanical property development during the drying of particulate coatings containing rigid particles, and the how these conditions are impacted by coating formulation variables and processing conditions. The motivation is to better predict and control the coating performance by optimizing the formulation design and drying condition. Characterizing drying behavior and correlating the stress development with microstructure evolution are critical in this research. In Chapter 3, drying characterization approaches are introduced. To extend the capability of stress measurement, walled substrates with different dimensions and materials were designed. And a shrinkage measurement method allowing convenient correlation of the microstructure change with stress development was developed using laser profilometry technique. Chapters 4-6 focus on investigating the role of formulation variables on the drying and cracking of coatings prepared with micron-sized particles. Chapter 4 focuses on studying the effect of particle size distribution. The study showed that with similar average particle size, coatings prepared from particles with a wide particle size distribution form a more compact microstructure, but are prone to cracking due to high tensile stress development on drying. Chapters 5 and 6 study the effect of particle shape on coatings cracking resistance. Different levels of clay particles were added to particulate coating systems prepared from the irregular-shaped ground calcium carbonate (GCC) particles and the spherical-shaped silica particles. The different geometry constraints of the mixed particles have altered impacts on the drying shrinkage and mechanical strength of the coatings, thus different cracking behaviors were observed. Finally, in Chapter 7 attention is shifted from the particulate coatings with the micron-sized particle to those prepared from nano-sized particles. Formulation variables of particle size and shape were characterized using coatings of nano-silica particles, nano-zinc oxide particles, and fumed-silica.

Contents

List of Tables

List of Figures

Chapter 1

Introduction

1.1 Overview

The coating industry provides real value to the world economy and develops with amazing growth rate. In 2016, the product shipments by U.S. paint and coatings producers reached an estimated $30.2 billion, rising 10% from 2015 [3]. The importance of the coating can be told not only from its multi-billion dollars international market but also its ubiquity in our everyday life. With profound performance in protecting and preserving objects, traditional coatings are commonly applied to prolong the lifespan of consumer products [4, 5, 6]. But as new materials and techniques develop, the coating industry evolves with market trends. Coatings now can be designed to alter more surface functionalities, which expands the applications to electronic devices [7], optical lens, food [8, 9], and medical devices [10, 11].

The formulation design is one of the most critical and complex steps to engineer the coating with desired properties. For a typical particulate coating formulation, the compositions include solvent, particles and additives. The variety of choices for each component makes it possible for a coating to provide different functions to the substrate, including mechanical strength, reflectivity [12], printability [13], electrical and magnetic properties. The solvent, which is either organic or aqueous for solvent-based and water-based coatings, is used for dissolving or dispersing the other two components. It provides the coating with tunable viscosity, volatility, morphology of other components and solidification mechanism. For example, solvent-based paints [14] can

be solidified via chemical reaction with oxygen, which are less susceptible to the environment and able to serve the anti-corrosion function, while the evaporation of the water-based paints is influenced by humidity and temperature, making them impractical in some climates. The particles contained in particulate coatings are pigments and binders. Pigments are usually rigid inorganic particles, such as titanium dioxide, zinc oxide and silver particles, which provide color, optical [15, 16], and electrical [17, 18] properties of the coating layer. Latex particles are commonly used as binders which provide good binding of the particluate network. Additives include varied compounds such as rheological modifiers [19, 20], surfactants [21] and stabilizers [22], which are added to alter coating specific properties.

Designing the coating application step with proper processing method is as important as the formulation design. The coatings with varied formulations and functions are applied to the target surface via diverse processing techniques [23]. For instance, vacuum deposition method [16] is often used for coatings of optical and semiconductor devices where the nano-scale thickness is preferred. Slot-die and blade coating are the most common methods used to apply the liquid coating onto flexible substrates. Spray coating [24, 25] and spin coating [26] can be used to coat objects with a discrete shape or irregular surface.

To achieve good performance, the control of the solidification process is the other essential step of the coating product design. The mechanism of how coating turns into a solid state from a liquid form can be varied due to different formulations. Regardless of whether the solidification is driven by solvent removal [27, 28] or reaction [29, 30], major changes in coating structure and properties take place during this step [31]. Controlling of these changes and establishing the desired coating functions requires the proper solidification condition chosen based on a thorough understanding of the solidification behavior. For particulate coatings, the focus of this work, understanding the drying behavior and cracking behavior is the key to obtaining a high performance coating.

1.2 Motivation

Particulate coatings, which take the largest share of the coating market [3], have a vast diversity of industrial applications due to the wide choices for coating formulation and processing conditions. By choosing particles of different materials and sizes, coatings are given different properties. For example, the clay and calcium carbonate particles provide paper coatings with good opacity and printability [13, 32]; nano-silica particles give optical coatings the anti-reflective property [12, 33]; and latex particles enhance the adhesion and mechanical strength of barrier coatings [34, 35]. The types and levels of solvent and additives are also critical in a coating formulation design. Water-based coatings are the primary choice of indoor coatings due to the health and environment concerns. But the regulations of volatile organic compounds (VOCs) limit the utility of additives like ethylene and propylene glycol [36, 37], which are used to help the film formation of coatings containing high molecular weight polymers. The workability of the coatings can be greatly reduced since the low VOCs level shorten the open time and wet edge time of many aqueous coatings [38]. Driven by the growing demand for good performance of engineered functions and green products, good knowledge of the impacts of each formulation variable is needed to optimize coating formulation.

As coating composition greatly influences the particulate coatings properties, the microstructure is just equally critical to coating performance. For water-based particulate coatings, drying is the crucial process influencing microstructure formation, stress development, properties evolution and defect formation. As deposited, the liquid suspension is stress-free, but as water is removed, the drying stress developed may cause defects [8-11], such as cracking, curling or delamination. And coatings prepared from non-deformable pigments, which retain their shapes during the drying process, are more likely to experience cracking problems due to the weak particle-particle interaction. Characterizing the dynamic changes of microstructure and drying stress helps to understand the drying behavior of particulate coatings. Investigating the final coating properties and crack formation reveals the insight of the coating cracking behavior.

The research proposed here is driven by the need to improve the properties and performance of a class of coatings prepared from suspensions of mainly non-deformable

particles such as ceramics, polymer latex particles with high glass transition temperature (T_g), some metals and nanocrystals. These suspensions are deposited onto substrates, dried and sometimes sintered at high temperature. Technical problems with these coatings, such as cracking, delamination and porosity control, require scientific investigation to reveal the sources of the weaknesses and relevant variables in coating design. More importantly, the drying and cracking behavior of coatings investigated in this work reveals the fundamental knowledge of microstructure and stress development of particulate coatings, which can be used for coating formulation and processing design.

1.3 Thesis Outline

This thesis is devoted to investigating drying and cracking behavior of particulate coatings and understanding the effects of different formulation and processing variables. Characterizing the dynamic changes in stress development and microstructure formation during the drying process is also crucial to understanding the drying of particulate coatings.

The work presented in this dissertation is organized into seven chapters. Chapter 1 provides an overview of the coating industry and briefly introduces the three steps in coating design, which are formulation design, coating processing and solidification. The motivation to study water-based particulate coating is explained by illustrating its wide applications and growing demand for improvement.

Chapter 2 introduces the essential background to understand the drying process of water-based particulate coatings. The general theory of drying, stress development and cracking are discussed. The purpose of this chapter is to make connections between stress development, microstructure formation and cracking behavior and to provide a foundation of the studies presented in the later chapters.

Chapter 3 presents the fundamental principles and modified designs of some important characterization methods and experimental techniques used in this work. Beam deflection method, the most important technique used for measuring the stress development, is discussed in detail. The capability of this technique is improved by controlling drying condition of the sample chamber and using walled cantilever substrates of the different design. CryoSEM is used as a powerful tool to capture the dynamic particulate

microstructure changes with the presence of water (frozen ice). And laser profilometry is used to characterize coating thickness change during drying, which provides shrinkage data correlating to the stress development.

Chapter 4 describes the effect of particle size and particle size distribution on drying of ground calcium carbonate (GCC) coatings. The drying process for coatings prepared from aqueous suspensions of GCC with tailored particle size and particle size distribution, as well as different types of binder, was investigated. Coating with pigments of wide particle size distribution is found to form non-uniform microstructure without the presence of the binder, but develop higher stress and denser microstructure with binder addition.

Chapter 5 discusses the effect of blending clay particles with the irregular pigments on coatings drying and cracking behavior. Using model paper coating system prepared from GCC pigments and binder, increasing the level of clay addition is found to enhance the cracking resistance. Further drying characterization reveals that the rising clay addition hinders the coating shrinkage and slightly decreases stress development.

Chapter 6 further investigates the impact of adding clay particles on the drying and cracking of particulate coatings using spherical pigments. Using coatings prepared from silica pigments and binder, the increase of clay content reduces the coating cracking resistance. Additional work of characterizing the stress development and shrinkage was done to explain this cracking behavior.

Chapter 7 investigates the stress development of particulate coatings prepared with nano-sized pigments. The stress development, microstructure and cracking behavior were studied using nanoparticle coatings of silica, zinc oxide and fumed-silica. The limitations of current drying characterization approaches used on thin nanoparticle coatings are also discussed.

And finally, chapter 8 offers some possible future research directions.

Chapter 2

Background

2.1 Introduction

Understanding and controlling the solidification process is essential to engineer coatings with desired properties and functions. The solidification of a water-based particulate coating is driven by water evaporation [39, 27]. Major changes in composition and important properties take place during drying. For example, properties like porosity, strength, gloss, particulate order, and concentration gradients are all determined by the way the particles come together, distribute and deform as the coating dries. Section 2.2 discusses the general theory of the microstructure formation during drying. With similar water removal process, the type, shape and size of particles and other additives may all influence the particulate network formation and thus impact the coating properties.

As the aqueous coating is deposited onto the substrate, the loss of water leads to volume shrinkage. As drying continues, the coating layer acquires solid-like nature and can support elastic stress development, resulting from shrinkage that is constrained by substrate adhesion. The origin and mechanism of stress development have been studied by many researchers using different coating systems. Here in Section 2.3, the fundamental background of stress development will be discussed specifically for water-based particulate coatings with varied compositions.

The cracking defect is one of the most common concerns of water-based particulate coatings, especially for the coatings with rigid particles. The cracking behavior is complex because it is determined by both the stress development and the material

response, which are both changing throughout the drying process. Considering the non-uniformity in drying and difficulty in measuring the mechanical properties of thin coatings, crack formation is difficult to analyze. In Section 2.4, the past research investigating the fundamental background of thin film cracking is introduced and the experimental approaches for characterizing the cracking behavior are illustrated.

2.2 Drying of Particulate Coatings

2.2.1 Particle and Water Distribution

Drying begins as soon as the liquid coating is deposited on the substrate and ends when all volatile liquids, such as water or solvents, are removed. In real applications, solvent removal can be done by either evaporation at the coating surface or absorption at the bottom through porous substrates. In this thesis, evaporation from the water-air interface is the only case considered, and the coating unless otherwise noted is referred to water-based particulate coating. As illustrated in Figure 2.1, the drying of particulate coatings can be categorized into three stages in general. In the supersaturated stage, the coating is rich in water and particles are well-dispersed, and brought together form loose network due to water removal. In the saturated stage, the particulate network reaches maximum packing and the water-air interface remains flat. And in the unsaturated stage, curved menisci penetrate into the coating and further compact the particulate network, in which stage deformation or coalescence of the soft particles can occur.

The evaporation rate determines the rate of which the coating′s free surface descends before the concertation reaching saturated stage [27]. Evaporation is a diffusion controlled process [40, 41]. The rate, E, can be expressed using Equation 2.1:

$$E = K_m(p^{sat} - p^{part}) \tag{2.1}$$

where K_m is a mass transfer coefficient of the water vapor over the air-coating interface, p^{sat} is the saturated vapor pressure of the water, and p^{part} is the partial pressure of the water in the ambient air (or the gas stream used for controlling drying condition). For the case of large coating area, the evaporation rate only depends on temperature and humidity and is therefore uniform over the coating surface in the initial stages of drying.

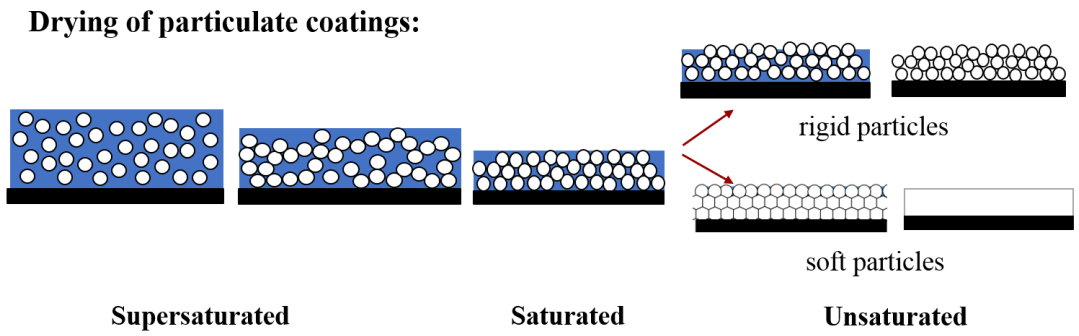

Figure 2.1: Schematic diagram of the particulate coating drying process, including three stages: supersaturated stage, saturated stage and non-saturated stage.

Evaporation can be influenced by the shape of the air-water interface [42] which will be discussed when introducing lateral drying.

The distribution of the particles in the vertical direction of the coating layer is controlled by evaporation, diffusion and sedimentation. Beneath the coating surface, particles move around under Brownian diffusion. The diffusion coefficient, D_0, is estimated using equation 2.2 with the particle radius R; the fluid viscosity μ; the Boltzmann constant k, and temperature T.

$$D_0 = \frac{kT}{6\pi\mu R} \tag{2.2}$$

In sedimentation motion, dense particles settle to the bottom with a velocity of U_0 under the combined effect of gravitation and buoyancy:

$$U_0 = \frac{2R^2 g(\rho_P - \rho_L)}{9\mu} \tag{2.3}$$

where ρ_P and ρ_L are the density of particle and liquid, g is the gravitational acceleration. The vertical particle distributions for coatings of varied relative strengths of evaporation, diffusion and sedimentation are illustrated in Figure 2.2. Many models are built to simulate the particle distribution during drying [43, 44, 45].

The drying regime map drawn by Cardinal and coworkers [46] provides the prediction of the particle distribution combining the three factors mentioned above using

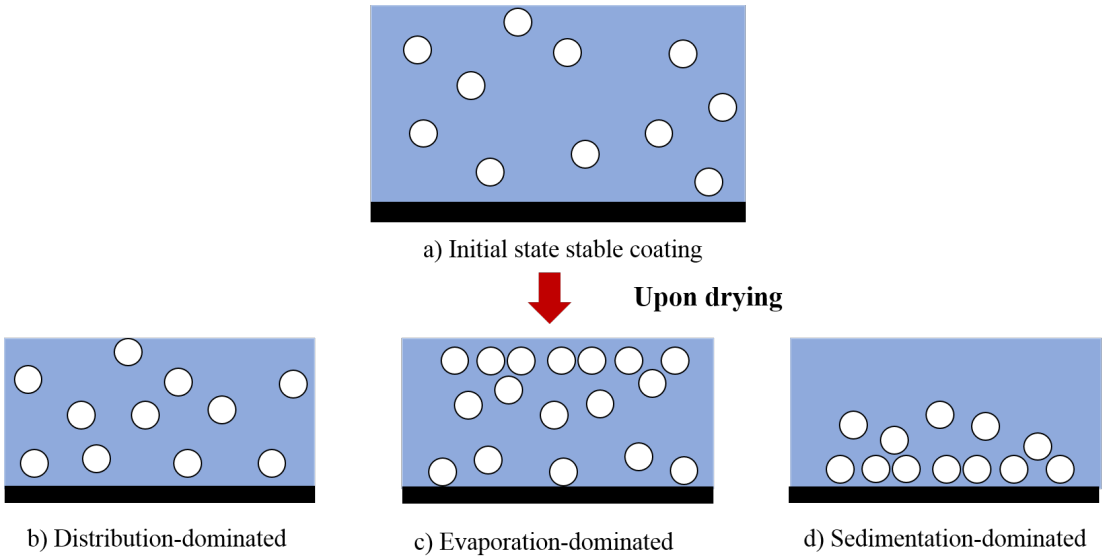

Figure 2.2: Vertical particle distribution upon drying of a coating. The drying of a) initially uniform distributed particulate suspension can be b) dominated by diffusion and stay uniform, c) dominated by evaporation and form a consolidation front, or d) dominated by sedimentation and accumulated at the bottom.

dimensionless numbers Peclet number, Pe, and sedimentation number, N_s. Peclet number (Equation 2.4) is balancing the evaporation rate with the diffusion rate and is used to predict the formation of consolidation front [47, 48], while the sedimentation number describes the strength of sedimentation to evaporation (Equation 2.5).

$$Pe = \frac{EH_0}{D_0} \tag{2.4}$$

$$U_0 = \frac{U_0}{E} \tag{2.5}$$

where H_0 which is the initial height of the coating thickness.

The different particle distributions in the vertical direction at the supersaturated stage result in particulate microstructures of different particle microstructure and porosity. As indicated by equation 2.4 and 2.5, formulation variables including particle size, density, coating viscosity and initial thickness all influence the particle distribution [49, 50], thus the microstructure formation. The microstructure with particle size gradient along thickness direction due to wide particle size distribution is discussed in detail

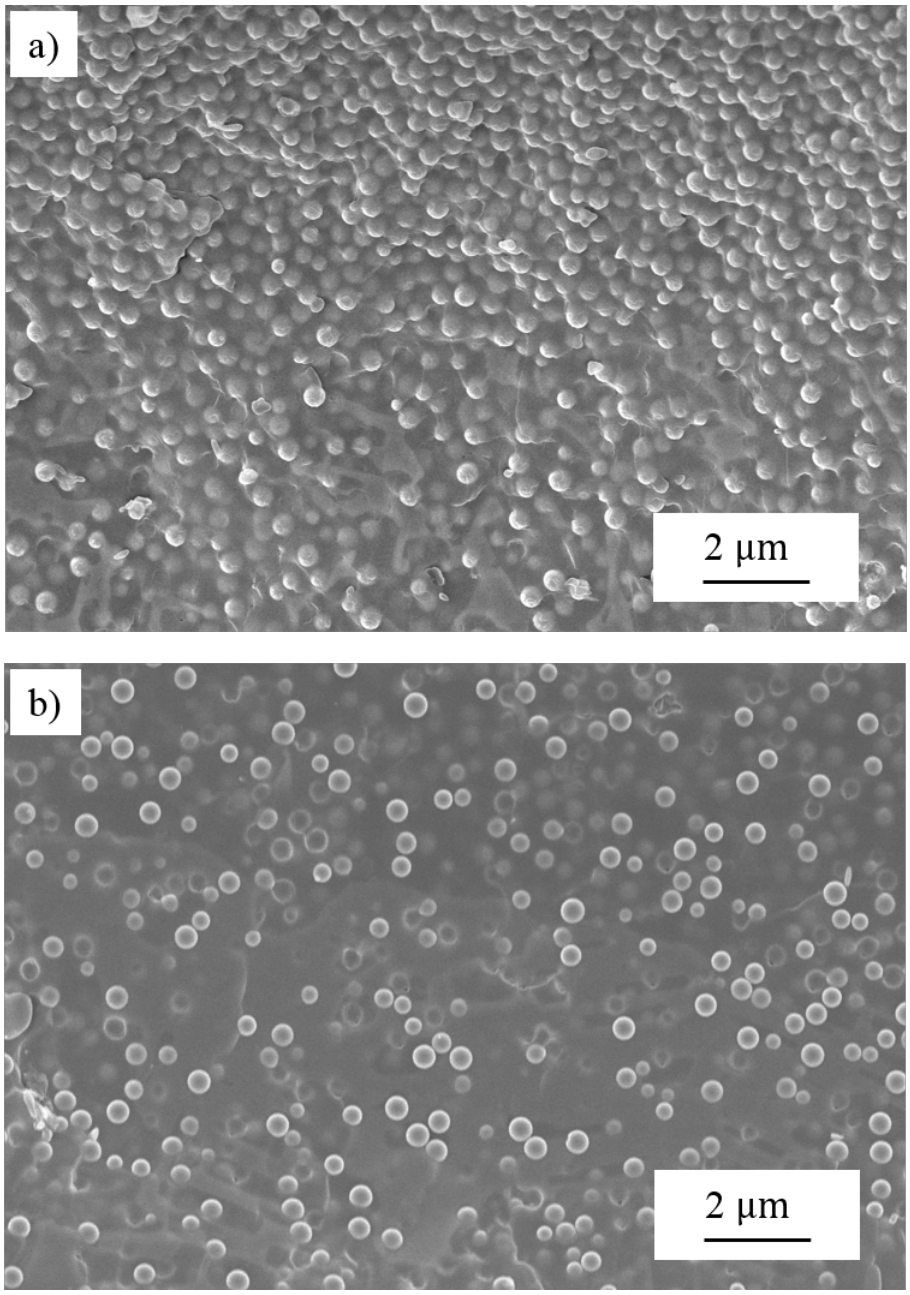

Figure 2.3: CryoSEM cross-sectional micrograph of coatings prepared from silica particles with size of 400 nm. Coating samples are frozen after drying for 3 min under a) 65 °C which particles accumulate near the top surface, and b) 25 °C which particles are uniformly distributed.

in Chapter 4. Different evaporation rates controlled by adjusting processing variables like temperature and flow rate also alter the particle distribution [51, 52, 53]. For example, the cryoSEM images (Figure 2.3) show the coatings with same formulation exhibit different particle distribution due to different drying temperature.

As evaporation continues, the particles are brought together and form a particulate network. Further water removal after the network reaches maximum packing drives curved menisci formation and air invasion into the coating particulate structure. In this unsaturated stage, the water evaporation rate is limited by the internal mass transfer, the transportation of the volatile liquid to the evaporation surface, instead of the external mass transfer in the gas region [54, 55]. As soon as the menisci form, the meniscus curvature, which is determined by the liquid surface tension, size and geometry of the open space between particles [56] leads to a water pressure gradient, Δ p (capillary pressure): [57]

$$\Delta p = \frac{2\gamma}{r} cos(\theta) \tag{2.6}$$

where p is the pressure, γ is the surface tension, r is the radius of the menisci curvature and θ is the contact angle. When the pressure gradient is large enough to drive the menisci to descend into the porespace, the interface undergoes a"Haines jump" [58, 59] to the next available porespace to remain the curvature and thus the pressure [60, 27]. With repeated motions of "Haines jumps", the remaining water re-distributes to equalize the local pressure.

Upon evaporation, the water phase eventually vanishes and residual remaining water forms pendular rings [60], which is a bridge of water located between the adjacent particles. The size of the pendular ring is found to be related the drying humidity and related to mechanical properties of the final coatings [61, 62].

2.2.2 Particle Deformation

During the drying process, soft particles, such as latex binders with T_g lower than drying temperature deform [6], which closes the pore space and provides adhesion to the particulate structure. Many forces can possibly contribute to the deformation of the latex particles upon different drying condition [63, 64], including wet sintering [65,

66], dry sintering [67], Sheetz deformation [68], van der Waals force [69] and capillary pressure [28].

According to the deformation map developed by Routh and Russel [63, 64], the major contributing factor of the particle deformation for the particulate coatings studied in this work are sintering and capillarity. The driving forces of the wet sintering and dry sintering are the interfacial tensions of latex-water [65] and latex-air [67, 66], respectively. The tensions eliminate the interfacial area of the latex particles in contact and deform the particles. The latex deformation induced by capillary pressure is studied by many researchers [62, 28, 61]. As mentioned in the earlier section, with curved air-water interface concaving toward the air, the water beneath the surface has lower pressure than the air and exerts a force on the wetted particle surface. The estimated magnitude of forces acting on the particle during drying is compared in the work of Pekurovsky [70].

2.2.3 Pigment Volume Concentration (PVC)

The pigment volume concentration (PVC) [71] is an important parameter for coating porosity structure formation, thus the performance of gloss, mechanical strength, ink absorption and permeability. As mentioned, the latex binder particles deform and fill the pores in between pigments during the drying process. The critical pigment volume concentration (CPVC), defined as the PVC value that sufficient polymer binders fill all the open spaces in the pigments matrix, is where coating experiences dramatic changes in porosity related properties. Coatings with PVC higher than CPVC are designed to have porous microstructure, such as paper coatings [72, 73], thermal barrier coatings [74] and anti-reflective coatings [12, 75]. Taking the paper coating as an example, the clay content is usually higher than the CPVC; therefore, an increase in binder level can reduce voids and lead to higher flexibility and lower permeability [76, 77]. The coating systems studied in this work, including the ground calcium carbonate (GCC)-based coatings, silica-based coatings and nano-particle coatings all have PVC above CPVC. The coatings with PVC lower than CPVC forms continuous films with polymer being the primary phase. In these coatings, the pigments as the minority particles are usually added as a filler to enhance properties like color coverage [78], thermal insulation [79] and hydrophobicity [80].

CPVC of the particulate coating is related to the formulation variables influencing the packing efficiency like particle size, shape, pigment-binder size ratio [81, 82]. In the work of Lei *et al.* [82], the pigment-binder coatings prepared with smaller latex are found to have higher CPVC as well as better mechanical strength due to improved binding between the porous structures. Basically, the particles with shape and size (or particle size distribution) [83] that have more contact area are favorable in forming a continuous phase [84], which alters the CPVC.

2.2.4 Lateral Drying

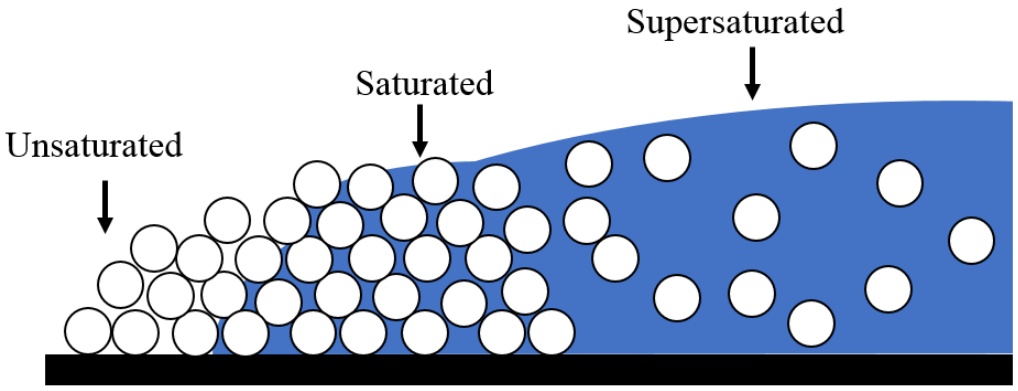

Figure 2.4: Schematics showing the regions of different stages at the drying front of a non-uniform drying particulate coating.

The drying introduced in the previous section considers the water removal to be uniform over the entire coating area, but in real cases lateral drying is often observed. The lateral drying phenomena describes the drying front propagation from the thinner edge towards the middle area of the coating during the drying process [85, 86]. During the lateral drying, particles accumulate at the edge of the free surface as shown in Figure 2.4, where all three stages described above can be observed at the same time at different coating regions. In the coatings containing soft latex particles, lateral drying can be easily identified due to the significant appearance change from opaque to transparent [87, 88]; while in the case of particulate coatings prepared with primary rigid particles,

the coating appearance change due to drying is less obvious, but the drying front can sometimes be recognized by different shades of the whiteness [89] and formation of the cracking [85, 88]. CryoSEM is also considered as a powerful tool to study the particulate microstructure under lateral drying. For example, Figure 2.5 is a cryoSEM image presenting the non-uniform particle distribution during drying due to lateral drying.

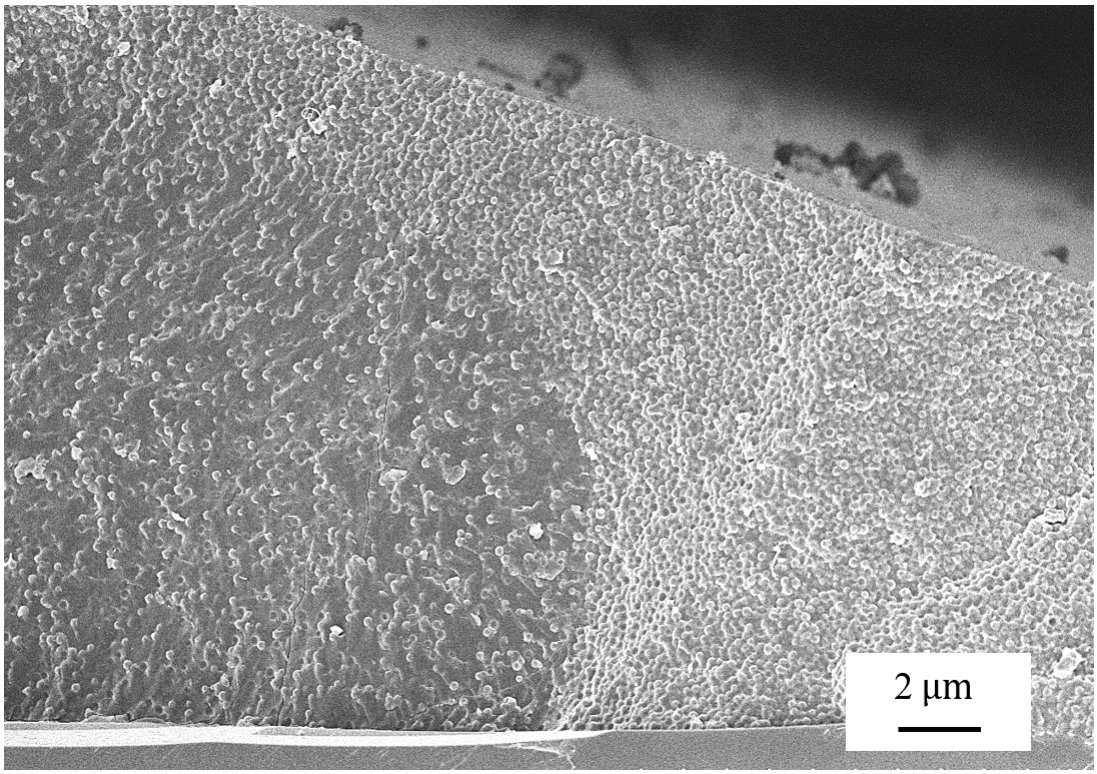

Figure 2.5: CryoSEM images of a silica coating prepared on a silicon substrate and frozen after 2 minutes of drying. The particles are more densely packed at the coating edge.

Lateral drying of particulate coatings often leads to non-uniform microstructure; for example, the "coffee rings effect", where the particles are accumulated at the edge of the coating area, leaving the coating with a thicker edge. Many models have been built by researchers [42, 86, 41, 90, 40] to investigate this complex process produced by the interplay of fluid dynamics, surface tension, evaporation, diffusion, capillarity, and more. Briefly, the edge of the coating experiences higher evaporation rate due to the lower

thickness and interface curvature. When the edge is pinned, evaporation from the edge leads to a flow carrying particles to the edge from the middle to replenish the removed water, thus resulting in this coffee ring. Coatings drying with higher evaporation rate [91] or formulated with particles with smaller size [86] and higher aspect ratio [92] shape are found to promote the lateral drying.

Even though the lateral drying has positive effects in a few applications [93, 94], it complicates the drying and cracking behavior of particulate coating, which makes drying characterization challenging. In this study, many methods were used to improve the drying uniformity during characterization.

2.3 Stress Development of Particulate Coatings

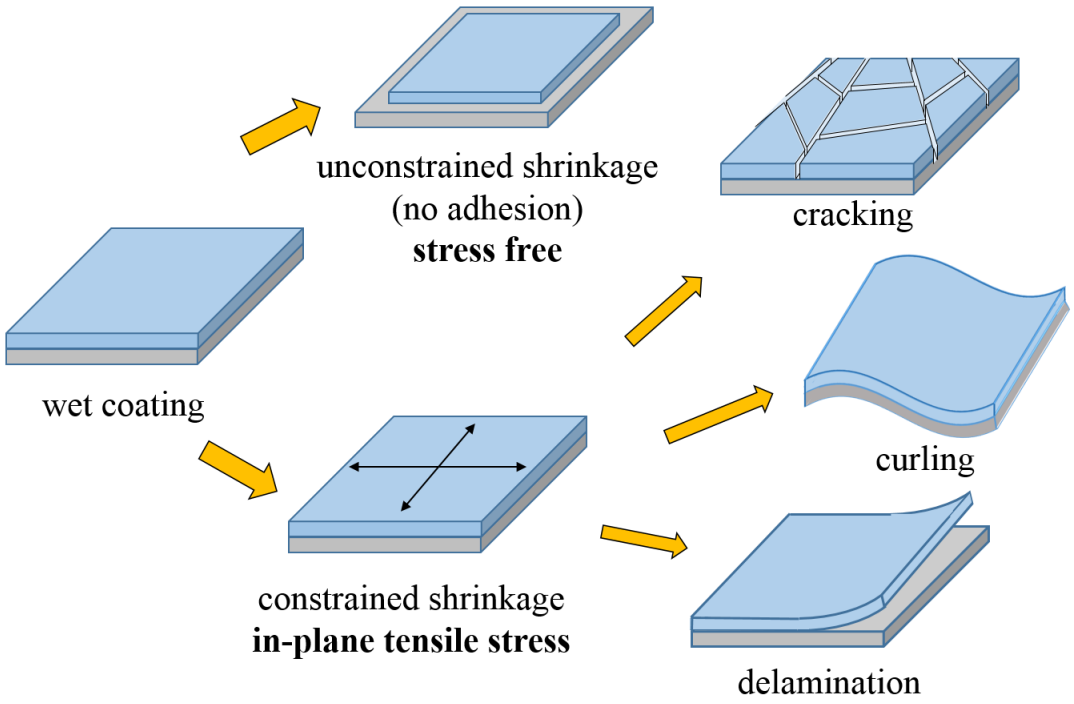

Figure 2.6: Schematic diagram of stress development in a drying coating with or without adhesion to the substrate, including three types of coating defects: curling, cracking and delamination.

Much research has been done to investigate the stress development [31, 95, 96, 97] during drying to gain better control of the coating performance and eliminate defects. Stress itself is not the major concern for coating applications, but the defects induced by the stress are important [31, 98, 99], as shown in Figure 2.6. If a coating is applied to a flexible substrate, coating stress can make the substrate deform, which is also called curling [98]. If a brittle coating is under a stress which exceeds the coating strength, cracks form [95, 100, 101]. When the adhesion between coating and substrate is not sufficiently strong, coating stress leads to cracks at the interface, which is also known as delamination [101, 96, 1]. Regardless of the type of defects, the engineered functions of the coating will be sabotaged due to the damage to the structure. Therefore, being able to predict and control the stress development during drying ensure the success in producing defect-free coatings.

In brief, the stress development in the coating layer is induced by constrained shrinkage which can be capillary induced or particle deformation induced. In the supersaturated stage of drying, as shown in Figure 2.1, the coating suspension is stabilized with its particles dispersed. As drying proceeds, particles are brought closer to each other and have less room to move freely. But in this stage, the coating is still liquid-like and can accommodate water loss by viscous flow [102]. As drying continues, particles are rearranged to accommodate the thickness decrease due to the further water loss and form a particulate network. Because of the coating adhesion to the substrate [31], subsequent volume shrinkages in this saturated drying stage can only occur in the thickness direction until the particulate network is densely packed. Up to this point, as illustrated in Figure 2.7, in region labelled as Phase I, no stress is developed for particulate coating containing only rigid particles. But for coating containing soft particles, particles that are deformed due to wet sintering may contribute to the constrained in-plane shrinkage and lead to the in-plane tensile stress development.

As liquid removal process continues, curved menisci form between particles and descend into the particulate network. As introduced in the previous section, capillary force, the dominating force in actions of draining liquid in the pores and removing liquid between particles, pulls particles closer and generates further constrained shrinkages. In this unsaturated stage, the stress development of coating containing only rigid particles and coating containing soft particles are different. In rigid particulate coatings, the

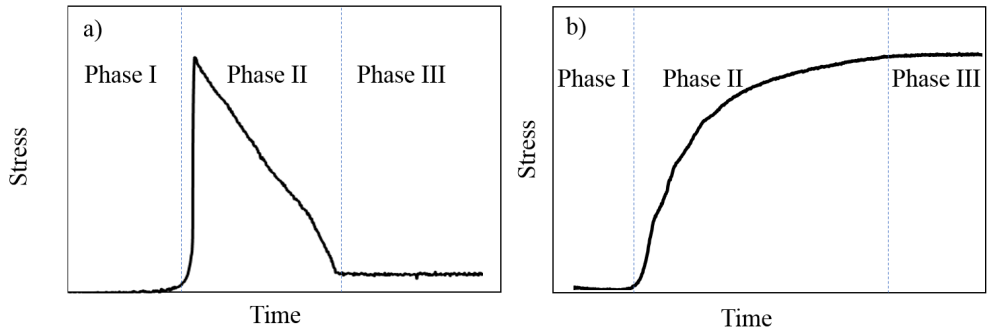

Figure 2.7: Two example stress developments curves representing a) coating containing only rigid particles and b) coating containing both soft and rigid particles. Each plot is divided into three phases: Phase I, coating is in the supersaturated stage; Phase II, coating is in the saturated and unsaturated stages; Phase III, coating is completely dried.

constrained shrinkage is solely due to the capillary effect. As shown in Figure 2.7a, the stress rapidly increases as soon as the curved menisci formed (Phase II) and slowly relaxed when menisci retreat into the particulate network since some particles are free from the capillary effect. When all the water is removed, the stress of rigid particulate coating drops back to zero (Figure 2.7a, Phase III). However, in coatings containing soft particles, the stress is attributed to both capillary effect and particle deformation. The stress develops gradually under the combined effect of curved menisci and particle deformation, as shown in Figure 2.7b Phase I. The stress keeps increasing for coating of soft particles during unsaturated stage (Figure 2.7b Phase II) and retains its value when drying completes (Figure 2.7b Phase III). The deformed particles act like "glue" and provide binding of particulate structure which can hold the constraint shrinkage.

The stress development introduced above happens under uniform drying. With lateral drying, the stress development is more complex depending on the drying front. The approaches inhibiting lateral drying during the coatings characterization [103] simplify the solidification process and allow us to better interpret the stress measurement data. Being able to study the effects of processing condition and formulation variables on coating stress development gives better prediction and control of the coating performance.

2.4 Cracking

Cracking is the most important defect seen in rigid particulate coatings, reducing the performance of coating engineered properties. Understanding the crack formation can help develop strategies to suppress crack formation and make coating products with desired functions. The relationship between the mechanical properties and stress development is important for cracking formation investigation. Due to the high modulus of the rigid particles, little particle deformation limits the particle-particle contact area, and thus the particle-particle interaction is weak. As introduced in the previous section, stress develops during drying. And the stress relaxation is the driving force for cracking propagation. Cracking indicates the developed stress exceeds a critical stress value, which depends on the coating thickness, elastic properties and fracture toughness [101, 100].

Determining the critical cracking thickness (CCT) [85], the thickness below which films do not crack, is considered as a convenient approach to studying cracking due to the difficulty in measuring the thin film mechanical properties. Many relations have been proposed to describe the CCT [104, 105, 106, 85, 107] including capillary pressure, particle size and shape, drying condition, substrates and additives. All these relevant variables influence the microstructure formation of the coatings, and thus both the stress development and mechanical properties are impacted. With the ability to measure stress development, CCT can then be used as an alternative approach to determining the mechanical properties of the coating layer. Therefore, the CCT measurement is utilized as a convenient method to estimate the coating fracture toughness.

Cracking behavior can also be characterized using other approaches. For example, the relationship between the cracking space and critical stress is presented in the work of Thouless [101]. Characterizing the cracking patterns using microscopy can then be used to analyze coating critical stress for cracking.

2.5 Summary

This chapter introduces many important features of the drying process, including the general drying of particulate coatings, the microstructure formation, stress development and cracking. Many processing variables and formulation variables can influence this

drying process. The purpose of this chapter is to make connections between the stress development, microstructure formation and cracking behavior. The knowledge of these concepts provides the foundation of the work presented in this thesis and can greatly benefit the coating design.

Chapter 3

Experimental Methods

Abstract—The purpose of this thesis is to investigate the drying behavior of aqueous particulate coatings and understand the impacts of important formulation and processing variables. Experimental methods that capture the dynamic changes of coating stress development, particulate shrinkage, and microstructure evaluation during drying process are indispensable. The coating systems studied in this thesis include mainly ceramic particles and latex particles, size ranging from 2.5 μm to 20 nm. To well characterize the drying process, many experimental techniques are used including beam-deflection stress measurement, scanning electron microscopy, digital microscopy, laser profilometry, nano-indentation, dynamic light scattering and extensional dynamic mechanical analysis test. Some of these techniques are commonly used in studying coatings and thin film materials. this chapter will highlight techniques that have modified procedures or are rarely used in coating characterization.

3.1 Stress Development Measurement

As discussed in Chapter 2, stress development during drying can lead to many coating defects such as cracking, curling and delamination, which hinder the coating performance. Many techniques have been studied to measure the stress development in thin coatings[108, 109, 97]. The beam deflection theory proposed by Stoney [110] and later improved by Corcoran [2] provides a convenient approach to measuring the dynamic coating stress without knowing the exact value of coating modulus, thickness and solid content. For coatings applied on a rigid substrate with good adhesion, the stress that develops in the coating layer during drying can lead to the substrate to curl. The curvature or deflection of the substrate in response to the drying stress can be measured and used for stress calculation [111, 112, 113]. The following section introduces the theory behind the beam deflection technique and the solutions to overcome some limitations of this technique.

3.1.1 Background: Beam Deflection Theory

In the classic beam deflection theory developed by Stony [110], the uniform stress causing deflection of the coated cantilever:

$$\sigma = \frac{E_s t^2 d}{3cL^2} \tag{3.1}$$

where E_s is the substrate modulus (but since the coating layer modulus is assumed to be similar to the substrate, the E_s is actually the E_{plate}); t and c are the thickness of the substrate and coating, respectively; d is the deflection detected from the cantilever free end; and L is the length of the free-hanging section of the cantilever. In this model, the deflection is assumed to be caused by the stress developed in the uniaxial direction only. Additionally, the coating thickness needs to be smaller than the substrate thickness to prevent shifting of the neutral axis from the center position. Using plate theory, Corcoran[2] modified the stress-deflection relationship into Equation 3.2 using bi-axial deformation.

$$\sigma = \frac{E_s t^3}{6c(t+c)(1-\upsilon_s)r} + \frac{E_c(t+c)}{2(1-\upsilon_c)r} \tag{3.2}$$

where E is the elastic modulus and υ is the Poisson ratio. The subscripts s and c denote the substrate and the coating layer, respectively. t and c represent the thickness of the

substrate and the coating, and the average coating stress σ is related to the curvature of the coated substrate r.

The second term of Equation 3.2 expresses the stress relief in the coating due to bending of the substrate. However, this term also requires knowledge of coating properties of modulus and Poisson ratio, which change through the drying process and are hard to obtain. In the work of Corcoran [2], it is shown that the second term can be neglected if $E_s \gg E_c$ and $t \gg c$. As shown in the Figure 3.1, the error of dropping the second term increases with the target coating thickness. For the stress analysis conducted using the standard walled cantilever of a silicon wafer (thickness of 520 μm, modulus of 170 GPa and Poissons ratio 0.064 [114]), the error is estimated to be 13% for a 500 μm-thick coating with 1.5 GPa modulus and Poissons ratio 0.3. Therefore, the material and thickness of the substrate are important for the beam deflection analysis.

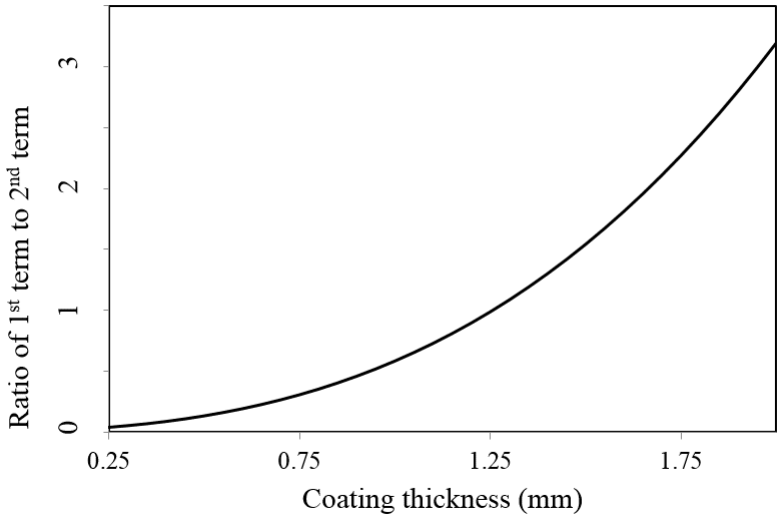

Figure 3.1: Error of dropping the 2nd term of the Corcoran equation at different coating thickness. Results are shown for E_s=170 GPa and E_c=1.5 GPa.

Additionally, some built-in assumptions for the Corcoran Equation lead to some limitations for the technique application. Since the deflection of the cantilever is analyzed as elastic deformation, the magnitude of the deflection needs to be within 10-25% of

the substrate thickness [111]. Also, as shown in Figure 3.2, the deflection, d, needs to be small for the curvature, r, to be estimated as:

$$r = \frac{L^2}{2d} \tag{3.3}$$

Thus Equation 3.2 can be expressed as:

$$\sigma = \frac{dE_s t^3}{3cL^2(t+c)(1-\upsilon_s)} + \frac{dE_c(t+c)}{L^2(1-\upsilon_c)} \tag{3.4}$$

when the deflection gets larger, the difference between L and X increases.

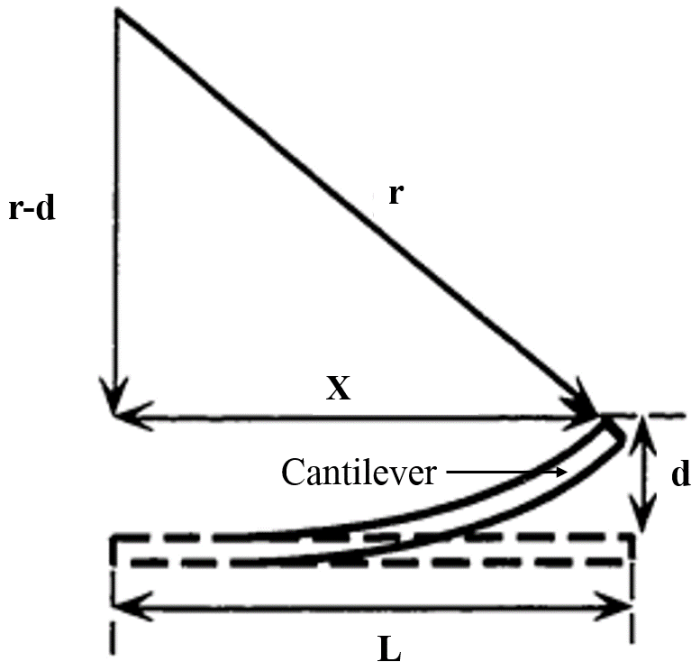

Figure 3.2: Curvature estimation of the cantilever beam. During calculation, X is approximated to be equal to L.

Another important assumption of the Corcorans Equation is that the stress is uniformly distributed through the entire coating area [2]. Thus, non-uniform (lateral) drying [87, 88] and the edge effect of the stress distribution [1] need to be taken into consideration when doing the experiment design. As discussed in Chapter 2, lateral

drying has great influence on the coating stress development, thus substrates with polydimethylsiloxane (PDMS) walls around the coating area[87] are used in the beam deflection technique to suppress the drying front movement. A correction factor, the ratio of substrate width, w_s, to the width of the coated area, w_c, is added to the Corcorans Equation (Equation 3.2) to account for the coating area reduction caused by borders used to limit lateral drying. The Corcorans Equation can be modified as follows:

$$\sigma = \frac{dE_s t^3}{3L^2 c(t+c)(1-\upsilon_s)} \frac{w_s}{w_c} \tag{3.5}$$

where the cantilever deflection, d, is measured throughout the drying process and used to estimate the average stress developed in the coating layer.

The width of the substrate cantilever is carefully designed to ensure the in-plane stress is the dominating contributor to the beam deflection and accuracy of the biaxial deflection measurement. Figure 3.3 shows the stress distribution near the free edge of a thin film studied by Hoffman [1]. To compromise the edge effect, which is the large peeling stress and shear stress at the film edge, the width of the substrate needs to be at least 2 times of the coating thickness. Therefore, the "edge section" dominated by the peeling stress is small enough comparing to rest of the coating area, making the in-plane stress to be the major contributor to the cantilever deflection. Also, according to the work done by Payne [112], the width-ratio need to be less than 18% to ensure that curvature over the cantilever cross-section would not greatly affect the deflection measurement between experiments if the laser was not accurately positioned to the center of the substrate.

3.1.2 Experiment Apparatus and Procedure

The stress measurement apparatus using beam deflection method was built by Payne [112] and adapted by Vaessen [115] and Price [113]. This apparatus was designed with a controlled environment chamber to clamp the long cantilever with coated liquid, where the dynamic deflection of the cantilever is measured. The equipment setup is very adaptable to coatings with different dimensions and drying conditions. A schematic diagram of the stress measurement shown in Figure 3.4. For the current research, some modifications are made to the experiment to improve the capability of the measurement.

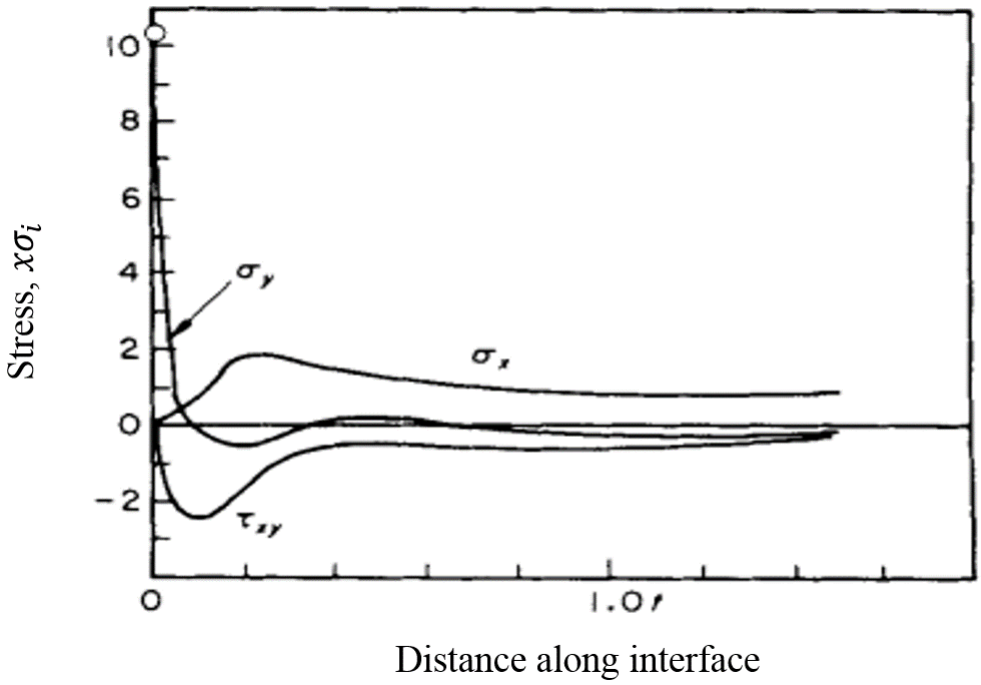

Figure 3.3: Normal and shear stresses distribution near the free edge of a film. σ_x is the in-plane stress, σ_y is the peeling stress and τ_{xy} is the shear stress. [1]

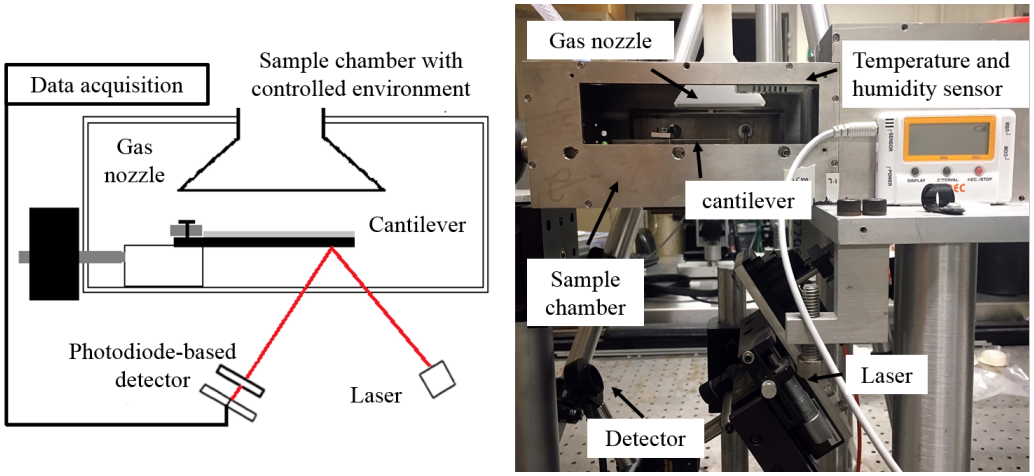

Figure 3.4: Schematic diagram (left) and equipment photograph (right) of the stress measurement apparatus used in this work to characterize the stress development in coating during drying.

In a typical experiment, a liquid coating is applied onto the standard walled cantilever substrate, which is the 520 μm-thick silicon substrate with a PDMS wall around the coating area. As shown in Figure 3.5, the silicon substrate is 6 $\times$ 60 mm with coating area of 5 $\times$ 44 mm; the non-coating area is left for clamping during testing. The PDMS (Sylgard 184, Dow Corning) wall added as the border of the coating area is prepared using elastomer base and curing agent with a ratio of 10:1. Also, after testing both square-edged and round-edged PDMS wall, the square-edged wall produces more reproducible results.

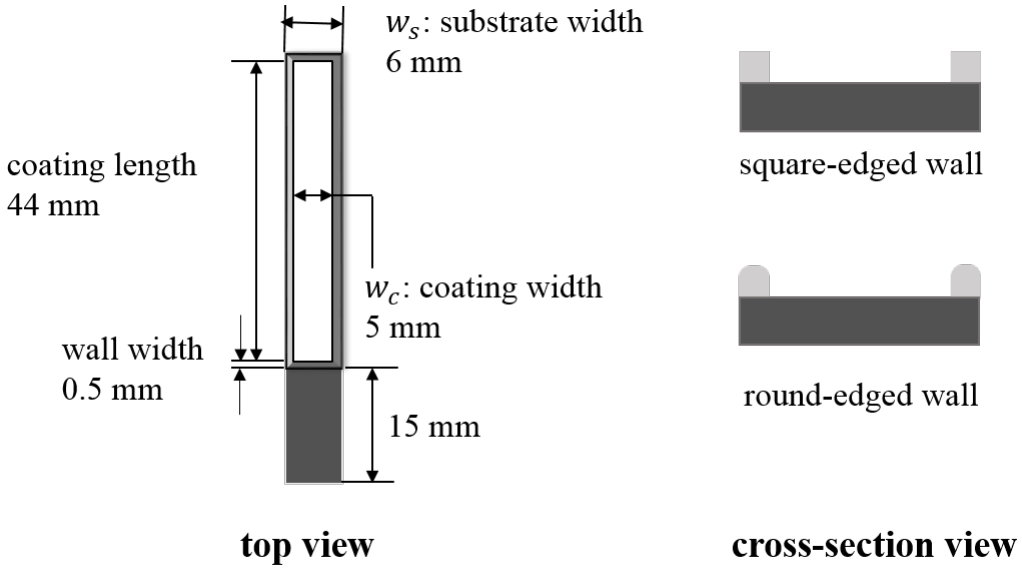

Figure 3.5: The schematic representation of the standard walled cantilever (left: top view, right: cross-section view) designed to improve the drying uniformity and reproducibility of the thickness measurement.

A stability test is required for each trial prior to testing to ensure proper clamping of the cantilever. During the five minutes of stability test, the reading of the laser deflection should be within 2.5 (laser Y position reading) with no trend of gradual increase or decrease. Otherwise, the cantilever needs to be re-clamped and the stability test repeated. To convert the laser reading to the actual cantilever deflection, a calibration test needs to be done. The free end of the cantilever is placed on the calibration bar

and lifted (See Figure 3.6). For every micrometer lifted by the calibration bar, the reading of the lasers vertical position is recorded. The plot of lifting value versus laser reading gives the slope used for deflection conversion. Before depositing coating liquid, the substrate is plasma cleaned for two minutes to improve liquid wetting. If the test is conducted under controlled condition, nitrogen flow with the right temperature and humidity needs to be circulated into the drying chamber for at least 10 minutes before liquid deposition. As soon as the coating liquid is evenly distributed onto the cantilever and transferred into the chamber, the laser position needs to be recorded.

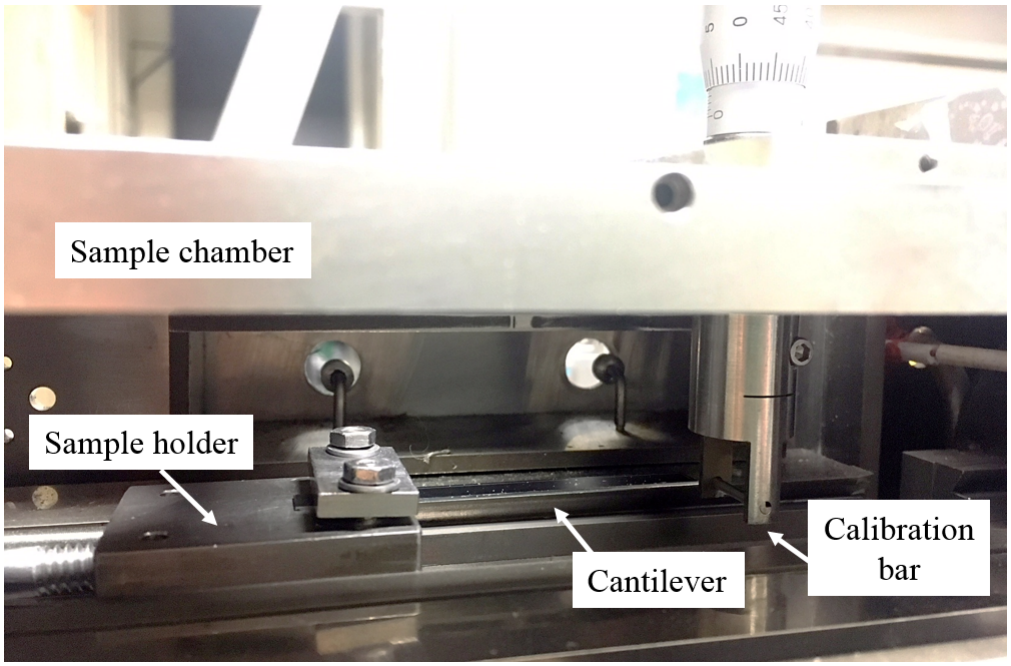

Figure 3.6: Photograph of the calibration step conducted to covert the free end lifting to the laser vertical position reading.

3.1.3 Drying Condition Control

Most coating samples studied in this work are aqueous particulate suspensions; therefore water evaporation has a substantial impact on the dynamic changes occurring during the solidification process. The drying conditions including temperature, humidity and air flow rate, which influence the rate of water removal, need to be carefully monitored

and controlled when testing the *in-situ* stress development. The condition of the sample chamber shown in Figure 3.4 is controlled using nitrogen flow. One setup for only the humidity control is shown in Figure 3.7, where one stream of nitrogen flow goes through the water bottle and gets humid while another stream remains dried. The two streams of flows can be mixed with a varied ratio to obtain the desired relative humidity. Using this setup, the mixed nitrogen flow is at room temperature, which is 23 °C ± 1°C.

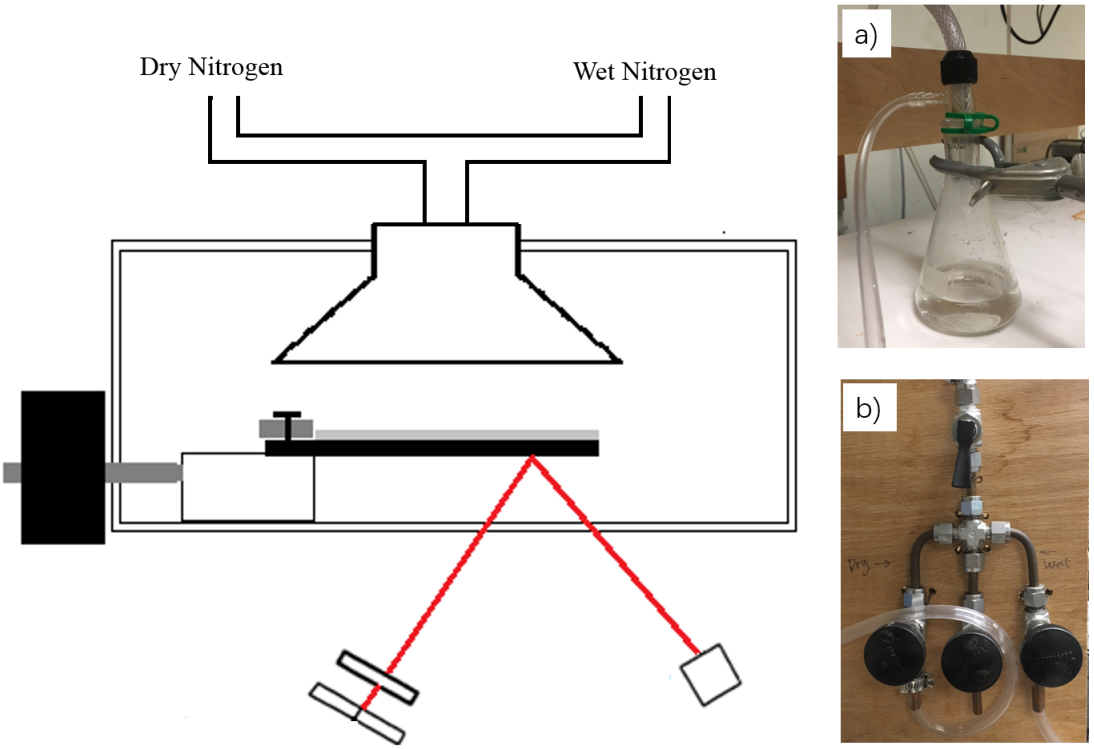

Figure 3.7: Setup of simple drying condition control using nitrogen flow with only humidity regulation. a) Photograph of the wet nitrogen flow setup used to prepare the flow with high humidity. b) Photograph of the gas flow regulator designed to adjust the mixture of dry and wet nitrogen flow.

Another setup for controlling drying condition including both temperature and humidity is shown in Figure 3.8. In this case, the humid stream of compressed air reaches 100% relative humidity by going through the water columns. The humidity can then be controlled by varying the mixing ratio of humid and dried air streams. The mixed

stream then flows through the heating tube with a temperature controller. The air with desired temperature and humidity can be circulated into the drying chamber and maintain the drying condition during the stress measurement.

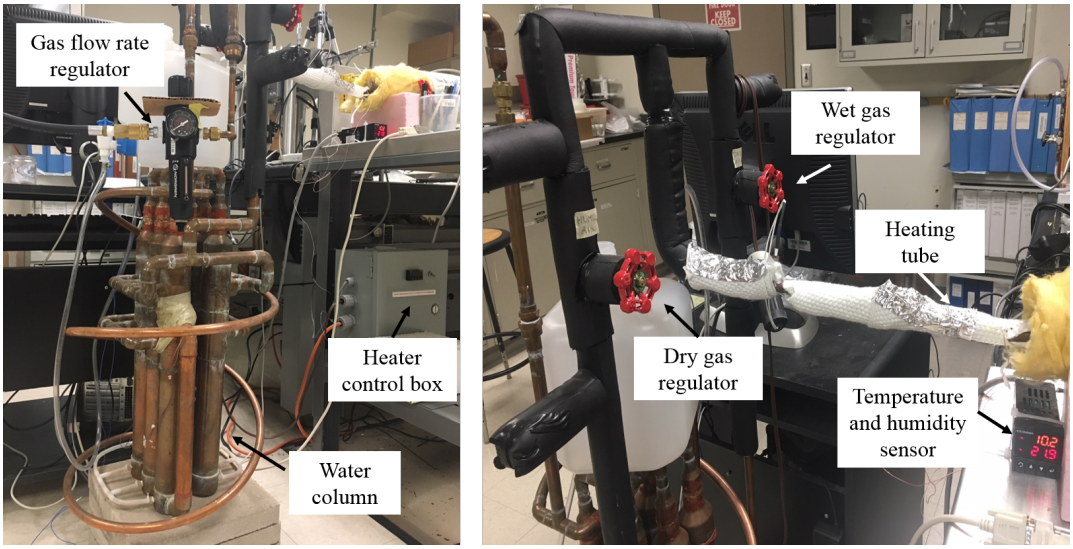

Figure 3.8: Photographs of the setup of drying condition control using air flow with both temperature and humidity regulations. Left: water columns used to prepare 100% relative humid air flow; Right: regulators for mixing dry and wet air flows and the heating tube.

3.1.4 Cantilever Design

As introduced in Section 3.1.1, the important assumptions made in the Corcorans Equation bring limitations to the substrate cantilever design, including the material modulus, thickness and length-width ratio.

The material of the substrate needs to be selected by evaluating its modulus and thickness. To eliminate the second term of the Corcoran equation (Equation A.2), which represents the stress relief in the coating layer, to avoid the need to measure the modulus and Poisson ratio of the coating layer, the ratios of the coating modulus to the substrate modulus and coating thickness to the substrate thickness need to be kept small. For a typical coating sample measured using this technique, the thickness is around 80 μm and modulus is approximately 5 GPa. The standard silicon wafer with a thickness of

520 μm and modulus of 160 GPa [114] can be used as the cantilever, which results in little error when applying modified Corcoran Equation (Equation 4.1). However, in the case that coating layer develops the high level of stress and leads to substantial bending, steel substrate can be used as the cantilever to prevent the large magnitude of beam deflection. (More discussion about deflection magnitude limitation can be found in Appendix A) The deflection of the substrate needs to be small enough to keep the plate theory [2] valid for the stress analysis, but still large enough to be distinguished from the systematic instability by the laser detector. Figure 3.9 gives some examples of the cantilever substrates with different material, dimension and wall design used for this beam deflection technique.

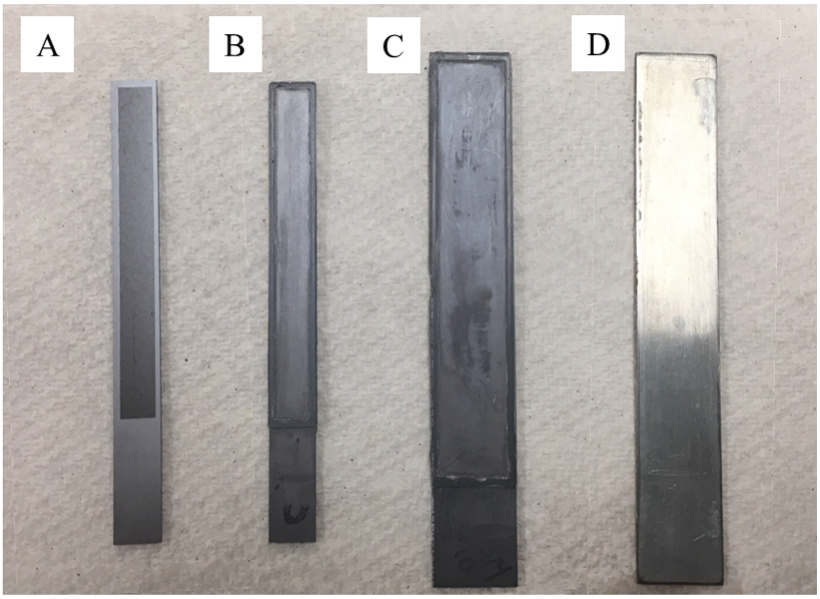

Figure 3.9: Photographs of cantilevers designed with different material, dimension and wall used for the beam deflection technique. Sample A: 520 μm-thick silicon substrate with etched-in wall design using photolithography; Sample B: Standard silicon walled substrate with thickness of 520 μm and PDMS wall; Sample C: Large silicon substrate with thickness of 800 μm (coating area 47.5 mm $\times$ 8 mm) with PDMS wall; Sample D: Large steel substrate (coating area 47.5 mm $\times$ 8 mm), will add PDMS wall and gold sputtering backside of the substrate before using.

To characterize the stress development of thick coatings, cantilevers with large dimension were used, such as sample C shown in Figure 3.9. (The detail work of designing

larger cantilever for thicker sample is given in Appendix A.) The width of the substrate is chosen to be four times the target coating thickness, which ensures the portion of the in-plane stress to be the major contributor of the cantilever deflection [1]. The width-length ratio is 0.18 according to the work done by Payne [112], which provides great accuracy of measured deflection and prevents errors due to the edge curling.

The height of the wall of the cantilever is designed based on the wet coating thickness. The PDMS wall made using aluminum mold has the height of 0.3 mm and 1.5 mm for the standard and large cantilever design. To characterize the stress development of coating of nano-scale particles and small thickness, the 0.3 mm-high PDMS wall is too large for the small liquid deposition. Walls that are much higher than the wet coating thickness can cause the formation of large pinning edges near the wall and could lead to non-uniform drying [87, 116, 117]. Walls with lower height can be made by using photolithography technique to edge the coating area. An example cantilever is shown in Figure 3.9 (Sample A).

3.1.5 Finite Element Simulation of Cantilever Deflection

Before applying walled substrate in stress measurement, simulations using *ANSYS* software were done to estimate the effect of PDMS wall on bending of the silicon cantilever [103, 87]. Two factors were considered: the addition of the PDMS wall with varied width, and the reduction of the coating area. According to the simulation results, the error caused by adding the PDMS wall can be minimized to within 3% by designing the wall of 0.5 mm-wide on a standard silicon substrate and analyzing deflection with a correction factor.

The simulation is based on the thermal stress model, where the coating generates constrained shrinkage due to mismatched thermal expansion during temperature changes. In the simulation setup, the wall-substrate has one end fixed and a coating applied to its top surface, same conditions as in beam deflection technique, as shown in Figure 3.10. The mechanical properties of the substrate and the wall were set to be the actual values of silicon wafers [114] and PDMS material [118], except the thermal expansion coefficients were zeroes, thus the coating would be the only source of shrinkage. The coating was considered as a 150 μm-thick slab with Youngs Modulus of 1.5 GPa, Poissons ratio of 0.3, a density of 2.65 g/cm^3 and the thermal expansion

coefficient of 300 C^{-1}. By choosing proper temperature change, the magnitude of the cantilever deflection is controlled to be approximated 7-8 μm, close to the experimental measurement.

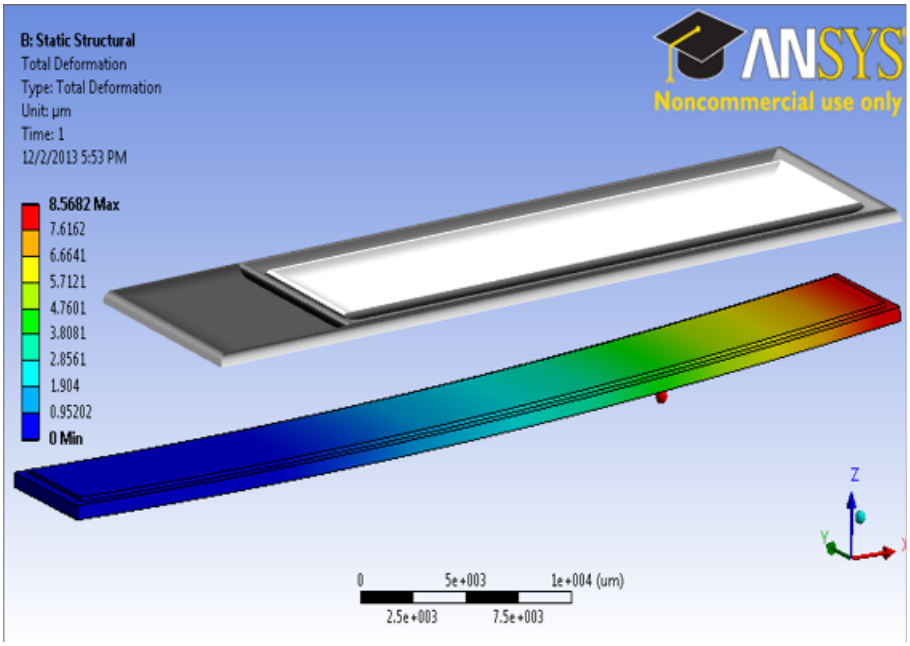

Figure 3.10: The deformation of standard silicon cantilever with PDMS wall simulated using Finite Element method.

Figure 3.11: Schematic diagram for the cross section view of coating samples run using finite element method.

The PDMS wall was designed to be 200 μm in height with a width varying between 0 to 1.25 mm. For a given temperature drop, simulations were run using both reduced area sample and reduced area with wall sample, as shown in Figure 3.11 for each wall width. And the deflection differences are plotted in Figure 3.12. As expected, the error increases with the wall width. Therefore, a 0.5 mm-wide PDMS wall is chosen to be

used in the beam deflection experiment, with the error of only 3%.

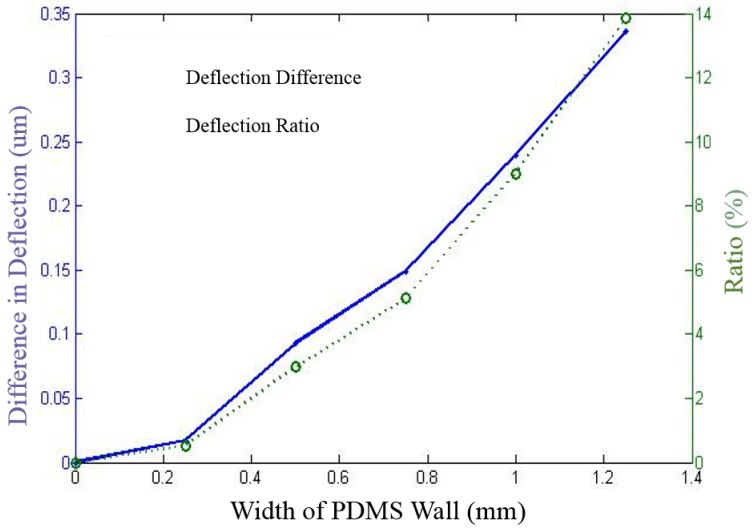

Figure 3.12: Deflection differences between walled and non-walled substrates covered with reduced area coatings and simulated under the same thermal stress model. The ratio of the deflection difference to total deflection using non-walled substrate is plotted in dash line.

As discussed in the previous section, the coating is considered to cover the entire surface of the substrate for the defection-stress analysis of Corcoran equation [2]. Adding walls to the substrate leads to the reduction of the coating area, which needs to be explored to determine its impact on the cantilever deflection. Simulations comparing the deflection difference between the fully coated sample and reduced area sample (see Figure 3.11) were executed. According to the simulation results, shown in Table 3.1, a correction factor $\frac{w_s}{w_c}$ can be applied to the equation to correct the calculated stress value from the reduction area.

3.2 Cryogenic Scanning Electron Microscopy (cryoSEM)

One of the most important objectives of investigating the drying behavior of a coating is to understand the evolution of the structure-property relationship. The formation of

Table 3.1: Finite element simulation of deflection results for fully coated sample and reduced area sample. The deflection ratio and correction factor are also listed.

Wall Width (mm)	Deflection of Reduced Area (μm)	Deflection of Fully Coated (μm)	Deflection Ratio	Correction Factor
0	8.34	8.34	1.00	1.00
0.25	7.64	8.34	1.09	1.09
0.50	6.84	8.34	1.22	1.20
0.75	6.12	8.34	1.36	1.33
1.00	5.38	8.34	1.55	1.50

the microstructure plays a key role in determining coating properties and performance. Being able to capture the dynamic changes during the drying process with the presence of the solvent, for example, the movement and distribution of particles, makes cryogenic scanning electron microscopy (cryoSEM) a powerful method in coating drying characterization. CryoSEM uses the same working principles as the conventional scanning electron microscopy (SEM), which is commonly used to image the microstructure of fully dried samples.

3.2.1 Introduction

SEM is one of the most widely used instruments for obtaining high-resolution images of the morphologies of solid material. The Field Emission SEM (FESEM), which is used in this work (Hitachi SU-8230 FESEM), can reach a resolution of 1.1 nm [119]. The image is generated by scanning a focused beam of accelerated electrons across the sample surface. The contrast of the image illustrates the topography of the solid surface, as well as the electron density. However, due to the high vacuum environment of the sample chamber (around 10^{-6} Pa), no liquid-containing sample can be imaged without solvent evaporation and microscope contamination.

The cryoSEM technique provides a solution to visualize the sample with the presence of liquid. In cryoSEM, the sample is vitrified to preserve the microstructure and imaged using the SEM equipped with a cryo-stage to maintain the low temperature (-140 to -180 °C) using liquid nitrogen. In addition, cryoSEM is also used on samples that are soft and beam sensitive [120, 121, 122], because the low temperature reduces the damage

resulting from the beam interaction and allows better resolution [123].

3.2.2 Experiment Apparatus and Procedure

In this work, the Hitachi SU-8230 FESEM equipped with a cryo-stage (ACE 600) was used for the cryo-imaging. The preparation of the sample was conducted using similar methods as previous researchers [46, 124, 125, 126, 87]. Coatings were prepared on 5 mm $\times$ 7 mm silicon substrates which were pre-scored to achieve more reliable fracture. Similar deposition procedures as that used to prepare coated cantilevers for stress measurement were used here. For CryoSEM samples, coatings were left drying for different times and plunged into liquid ethane to vitrify the specimens [87]. Liquid ethane is chosen to be the more effective cryogen than liquid nitrogen due to its high cooling rate (around 1.2×10^4 K/s) [127, 128]. The violent boiling of the liquid nitrogen generates a gas layer between the sample and cryogen leading to less efficient heat transfer and lower freezing rate. Then the frozen samples were transferred to liquid nitrogen and mounted in a specimen holder. The holder, at liquid nitrogen temperature, was transferred to the cryo-preparation system where the coatings were fractured and sputtered with platinum under the protected environment (Leica EM VTC 100). Approximately 10 nm of platinum was sputtered onto the coating surfaces to reduce charging during imaging.

In some cases, the sublimation process is conducted between the sample fracture and sputter steps. In sublimation process, the temperature of the cryo-preparation chamber is raised to -96 °C, which etches away the vitreous ice at the rate of 10 nm/s [129]. The sample with low solid concentration, for example, the coating shown in Figure 3.13, etching away some of the frozen water from the fracture surface increases the topographic contrast and help recognize the particle morphologies. However, when the amount of the remaining water is critical, such as the example given in Figure 3.14, sublimation can alter the result considerably.

It is important to minimize the exposure of the frozen sample to ambient air during cryo preparation. Frost contamination due to condensation of the air moisture onto the sample can substantially alter the surface topography by forming decorations or covering the entire fracture surface.

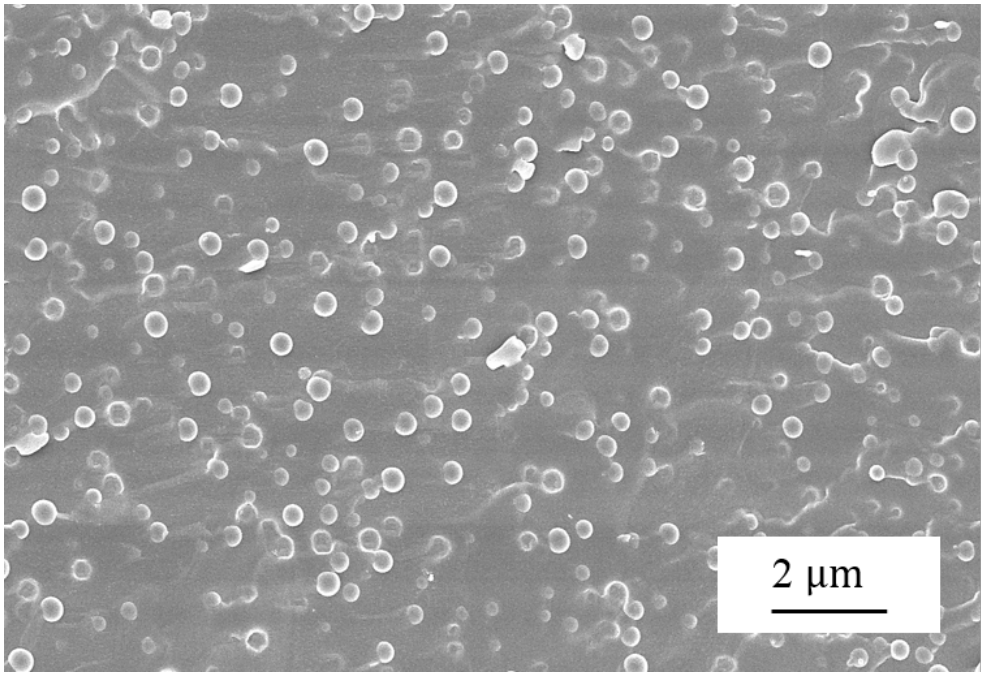

Figure 3.13: CryoSEM cross-sectional micrograph of sample preparing from polystyrenes with size of 400 nm. Sample is frozen at early stage of drying when the coating is rich in water.

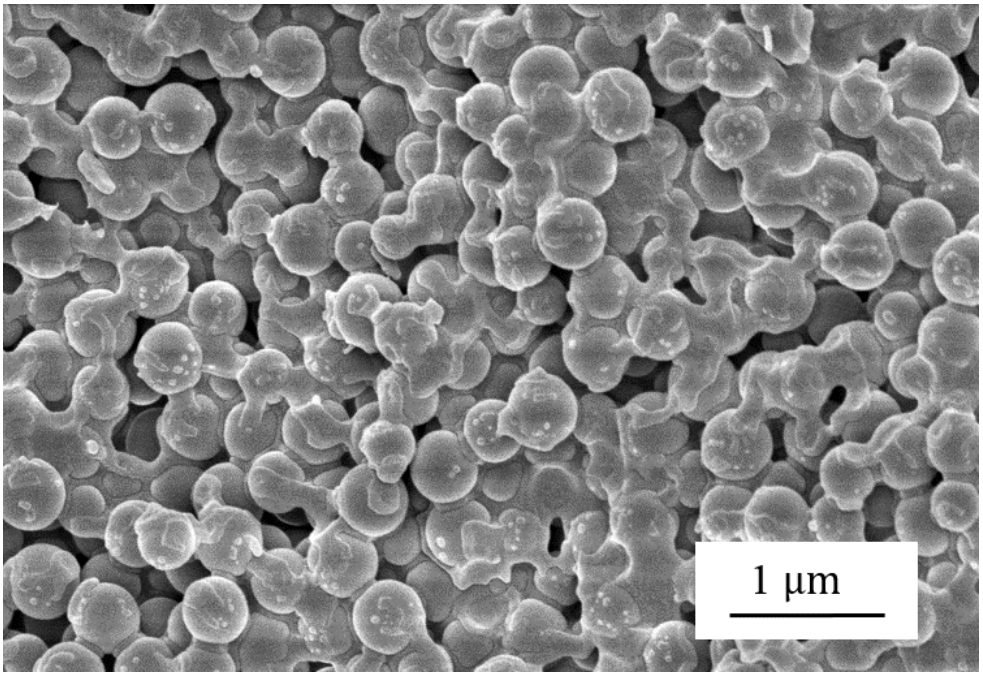

Figure 3.14: CryoSEM cross-sectional micrograph of sample preparing from polystyrenes with size of 400 nm. Sample is frozen at later stage of drying when the coating is porous.

3.3 Laser Profilometry

3.3.1 Introduction

Although cryoSEM is a powerful technique to characterize the microstructure evolution during drying, it is time-consuming and expensive. Also, correlating the results of microstructure change to the data of stress development can be difficult due to the difference in sample dimension. The use of a non-contact laser profilometer is more convenient to explore the coating thickness change using the same coating deposition methods applied in the stress measurement (introduced in Section 3.1). A non-contact laser profilometer (KEYENCE LJ-V7060) is used to study the *in-situ* coating thickness evolution during the drying. The most common use of the laser profilometer is to detect the dimension or surface of manufactured parts [130, 131, 132]. To capture the dynamic change of the coating thickness, thus the shrinkage, some modifications are made to the apparatus setup to overcome the limitation of the equipment. Since the shrinkage of the coating represents the coating microstructure changes and is closely related to the constrained shrinkage, the laser profilometry technique is used together with other characterization approaches to understanding the crack formation and stress development.

3.3.2 Experiment Apparatus and Procedure

The laser profilometer used in this work generates a stabilized high-precision profile by focusing a short wavelength (405nm) laser to its diffraction lens [133]. The laser beam is expanded into a line to be better diffusely reflected from the surface of the target. It is capable of providing a clear reflection regardless of sample color or reflectivity. Figure 3.15 shows the experimental setup of the laser profilometer, where the laser head is mounted on a 3D-printed holder with adjustable height and angle.

Two testing methods are developed to measure the thickness change of the coating sample using standard walled substrate. Selecting the same substrate as used in the stress measurement helps directly correlate the shrinkage to the stress development which is useful for data interpretation. Before a test, the laser profilometer needs to be set to “translucent” mode to obtain most reflection signal and the measurement frequency of 10 Hz. A plasma cleaned, PDMS-walled silicon substrate was positioned

onto the leveled platform. Two orientations can be used to position the substrate relative to the laser beam line: H orientation, the full cross-section of the coating is measured to get one center point measurement (as shown in Figure 3.15-left); and V orientation, the coating is measured down the center to get 800 center point measurements (as shown in Figure 3.15-right). The thickness of the coating layer was recorded every 10 seconds for the drying process and then recorded every 30 seconds for 3 minutes after the tested sample reached the final thickness. Plotting the thickness change as a function of time, the slope and the time for the thickness to reach a stable value are considered to be the shrink rate and the shrink time.

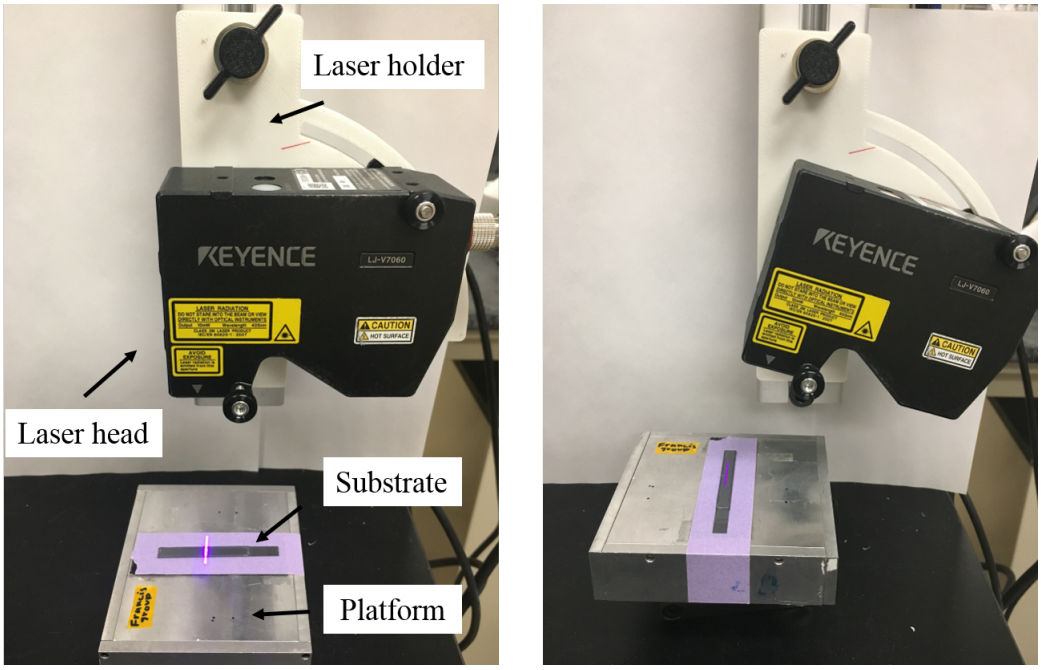

Figure 3.15: Equipment photograph of the laser profilometer apparatus used in this work to characterize the coating surface movement during drying. (Left: measuring opaque sample using H orientation; Right: measuring transparent sample with tilted laser head using V orientation.)

The two testing orientation have their own advantages. Using the H orientation, as illustrated in Figure 3.16, the full cross-section of the coating is captured with the platform thickness available as the reference value and coating center easy to find. The "absolute thickness value" reading from the laser is sensitive to the substrate placement.

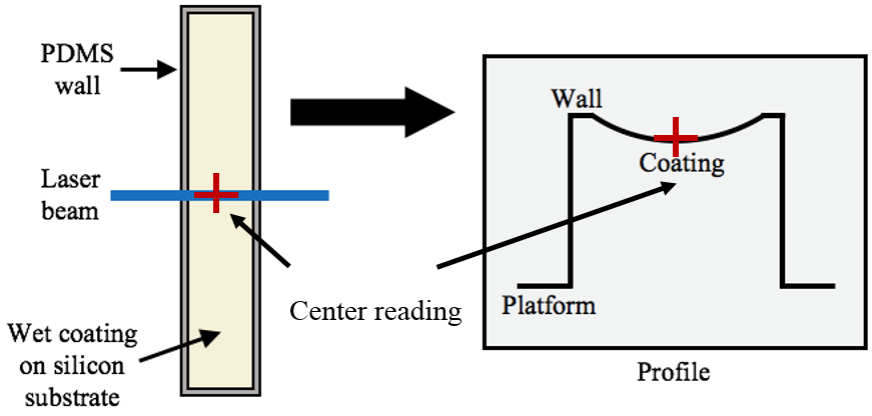

Figure 3.16: Schematic depicting laser profilometer measurement of a drying coating using walled substrate.

Having a reference point away from the coating profile improves the accuracy in measuring the actual thickness. However, due to coating thickness non-uniformity, a single thickness measurement of a coating cross-section cannot represent well the thickness of the entire coating area. More data points from the profile are better collected especially when testing the coating has high viscosity and is difficult to spread. In this case, measuring the thickness using V orientation, which is developed and evaluated by Tess Marconie [134], can give the thickness value averaged from 800 data points, improving the reproducibility. Possible error in measurement caused by positioning the laser beam line off the center was proven to be small [134]. For both orientations, the complete profile with 800 data points can be recorded for each time frame. To analyze the data, a Matlab code was written [134] (See Appendix B) to quickly determine the shrink rate, shrink time and total shrinkage.

3.4 Summary

This chapter introduced some important characterization approaches used for studying coating drying behavior. These techniques are often applied together to provide a more comprehensive understanding of the dynamic changes occurred during the drying process. For instance, with cryoSEM imaging the particle position through the coating

thickness, the origin of stress development can be better interpreted; using the shrinkage curve along with the stress measurement, the cracking behavior of a coating can then provide some insights of the mechanical properties using strain-stress relationship [135]. In addition, for different coating samples, other testing methods like the particle characterization (including size, shape, isoelectric point), critical cracking thickness measurement, and mechanical tests are also conducted to fully understand the coating drying and cracking behavior.

Chapter 4

Effect of Particle Size Distribution on Drying of Ground Calcium Carbonate Coatings

Abstract—The role of pigment particle size distribution on stress and microstructure development was studied for coatings prepared from aqueous suspensions of ground calcium carbonate (GCC) and latex binders. Stress development was monitored using a modified beam deflection technique under a controlled environment. The microstructure was characterized by scanning electron microscopy (SEM) and cryogenic SEM. For coatings containing only GCC particles and no latex, a wide particle size distribution resulted in a significant particle size gradient in microstructure, which interfered with monitoring stress development. With latex addition, uniform microstructures were observed in coatings with either wide or narrow particle size distribution. GCC-latex coatings prepared using GCC with a wide particle size distribution developed a higher stress than those prepared using GCC with a similar average particle size but a narrow particle size distribution. The higher stress is related to the particle packing that results in smaller pore sizes and larger capillary pressures that drive compaction. In coatings prepared with the same GCC particles but different latex binders, the stress and cracking behavior of the coating depend on the latex properties. [1]

[1] Some work introduced in this chapter has been published in [89].

4.1 Background and Motivation

Particulate coatings have a wide range of applications and take a large portion of the coating market share. By formulating the coatings with different particles such as ceramic [5] and metal particles [136, 137], polymer latex particles, and semiconductor nanocrystals particles [12], coatings can serve as barrier coatings [5], antireflective coatings [16, 138, 12], and printed electronic structures [7, 136]. Other than the material, the characteristics of the particles, especially the particle size and particle size distribution also have substantial influences on the coating performance.

The essential roles of the particle size and particle size distribution to the coating final properties are investigated by many researchers. Because of the influence of particle size distribution on coating microstructure formation, coating functions like wear resistance [139], water holding capacity [140, 72] as well as optical [141, 73] and mechanical properties [142, 24] of the coating layer are altered. However, little research has investigated the impact of the particle size distribution on the coating drying behavior, especially the stress development.

As introduced in Chapter 2, the stress development and microstructure formation during the drying process are critical to determining the final performance of the particulate coatings. Even though ceramic particles are responsible for many important properties, coatings of ceramic particles alone are relatively fragile due to weak bonding between the rigid particles. Latex binders or additives are frequently added to ceramic suspensions to improve strength and flexibility of coatings. Studies [143, 144, 49, 145] conducted on coatings systems containing both ceramic particles and latex particles have addressed suspension stability, microstructure, and stress development. Martinez and Lewis [145] studied the role of latex T_g and the relative amount of latex on the stress development of latex-silica coatings with an emphasis on the role of capillary stresses. At low latex quantities (up to 40 % by solids volume), they found that the stress rises to a peak and falls, mirroring silica alone but with lower peak stresses, and the packing of the latex and silica was important to the magnitude of the stress peak. Wedin and *et al.* [143] further studied the stress development of coatings made from calcium carbonate-latex suspensions with relatively small amounts of latex (latex/calcium carbonate = 0.1 by weight or 0.26 by volume). With soft latex, they found that the

coating stress first increases to a peak, assigned to a capillary pressure effect, and then rises to a plateau related to the compression and coalescence of soft latex. In these past studies, the size of the ceramic particles has been recognized as an important factor in coatings stress development. However, the role of ceramic particle size distribution on stress and microstructure development is not well understood.

Understanding the impact of particle size distribution on the stress development and microstructure formation during drying is essential to engineer a coating formulation that achieves the optimal performance. In this chapter, the stress evolution and microstructure development using coating systems composed of ground calcium carbonate (GCC) particles with tailored particle size distributions with and without latex are reported. This type of coating is similar to those used in the paper coating industry. Stress development was determined by cantilever beam deflection method [2, 146] using substrates with a soft border [103, 87] to limit lateral drying. This technique enables the investigation of stress generation without the influence of significant drying front movement. The combination of stress measurement and SEM/cryoSEM visualization provides insights of the influence of particle size distribution as well as latex binder addition on coating stress development.

4.2 Materials and Methods

4.2.1 Suspension Systems

GCC-based aqueous suspensions were prepared from commercial GCC particles (Hydrocarb 60 and Hydrocarb 90, Omya, USA). Both the coarse and the fine GCC particles were modified into two particle size distributions wide and narrow. Figure 4.1 shows the mass frequency plot from SediGraph data. The coarse GCC particles with wide or narrow particle size distribution are denoted as GCC-W and GCC-N, respectively. Similarly, FGCC-W and FGCC-N are used to denote fine GCC particles with wide and narrow particle size distribution, respectively. Eleven samples were investigated (as listed in Table 1): suspensions containing only GCC-W or GCC-N particles; suspensions containing both GCC particles and styrene acrylate latex (denoted as SA, approximate particle diameter of 0.2 μm, BASF, Acronal-S504. $T_g = 4$ °C); and a sample containing GCC-W and polyvinyl acetate latex (denoted as PA, approximate particle diameter of

0.2 μm, Resyn 1103, Celanese. T_g = 32°C); and a sample containing GCC-W and styrene butadiene (denoted as SB, approximate particle diameter of 0.12 μm, Latex CP 615NA, Trinseo LLC. T_g = 15°C); suspensions containing GCC-W particles, SA latex and additives polyvinyl alcohol (PVOH) (SELVOL 203S, with glass transition temperature T_g = 58°C) and ethyl acrylate (denoted as Alco) (Alcogum-L29, rheology modifier); and one suspension of GCC-W and lower content of SA latex. All coating dispersions were sonicated for 10 minutes prior to deposition.

Table 4.1: Compositions of eleven coating dispersions prepared from GCC particles given in volume percent.

Sample	Coarse GCC		Fine GCC		Latex			Additives	
	Wide	Narrow	Wide	Narrow	SA	PA	SB	PVOH	Alco
N		25.00							
W	25.00								
N-SA		29.19			15.07				
W-SA	29.19				15.07				
W-LSA	31.08				12.03				
FN-SA				29.19	15.07				
FW-SA			29.19		15.07				
W-PA	29.19					15.07			
W-SB	29.19						15.07		
W-SA-P	29.19				13.60			1.22	
W-SA-A	29.19				14.70				0.30

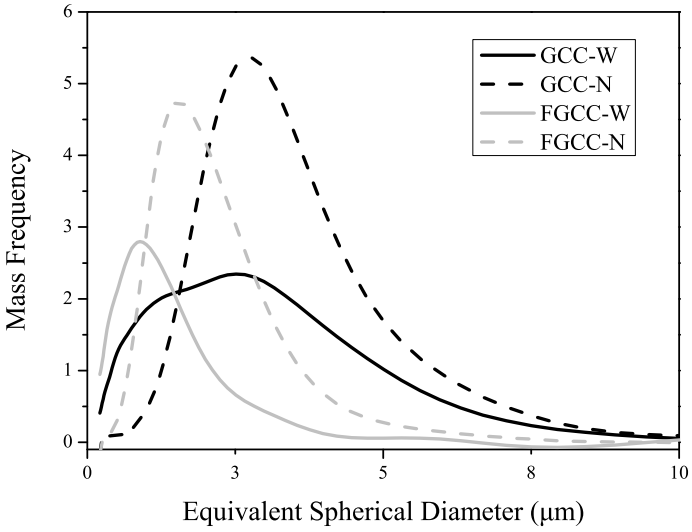

Figure 4.1: Particle size distributions of coarse GCC (GCC-W and GCC-N) and fine GCC (FGCC-W and FGCC-N). The average particles sizes are 1.9 μm and 3.1 μm for GCC-W and GCC-N, respectively; and 1.2 μm and 1.8 μm, for FGCC-W and FGCC-N, respectively.

4.2.2 Stress Measurement

Coating stress development was characterized using a beam deflection method [2, 146] with a walled cantilever [103, 87] which is introduced in detail in Chapter 3.1. In brief, the measurement is conducted by applying coating liquid onto the standard walled substrate (coating area: 5 × 45 mm; PDMS wall: 0.5 mm in width), which is plasma cleaned (Harrick Plasma Inc., Ithaca, NY). The stress developed in the coating layer due to drying causes the cantilever to deflect. The deflection of the cantilever is captured by a laser-photodiode system and translated using a calibration curve measured prior each experiment. The measurement takes place in a drying chamber with controlled temperature and relative humidity (RH). Coatings were applied to silicon cantilevers (Youngs modulus and Poissons ratio were taken to be E = 169 GPa, v = 0.064, respectively [114]) with polydimethylsiloxane (PDMS) walls to suppress lateral drying [103]. Using in situ visualization during stress measurement experiments, the coating is found to experience little spatial variation in appearance during drying, which is consistent with our previous work [103].

The average coating stress, σ, is calculated from the measured deflection, d, using the modified Corcoran Equation (discussed in Chapter 3.1, Equation 4.1):

$$\sigma = \frac{dE_s t^3}{3L^2 c(t+c)(1-\upsilon_s)} \frac{w_s}{w_c} \tag{4.1}$$

where E is the elastic modulus and υ is the Poisson ratio. The subscripts s and c denote the substrate and the coating layer, respectively. t and c represent the thicknesses of the substrate and the coating. And the average coating stress σ is related to the deflection d of the cantilever with coating area length of L. The correction factor the ratio of substrate width, w_s, to width of the coated area, w_c.

Unless otherwise noted, all stress measurements were conducted at 23 °C ± 1°C and RH of 6 %± 2% controlled by nitrogen flow. Either 30 or 40 μL of suspension was used to prepare the coatings to provide two thickness values. For each sample, 8-10 repeat runs were conducted at each drying condition, except GCC-only coatings (sample W and sample N), in which four trials were carried out. Representative stress development curves are reported. Final stress and thickness values are reported with an error based on a 95% confidence interval.

4.2.3 Microstructure Characterization

SEM was used to characterize coating microstructure after the drying. Coatings were prepared on 5 mm × 7 mm silicon substrates following a similar procedure as that used to prepare coated cantilevers for stress measurement; however, the coatings here were dried at room condition (22 °C and 40 % RH). Approximately 10 nm of platinum was sputtered onto the coating surfaces to reduce charging during imaging. The samples were imaged using secondary electron mode a Hitachi S-4700 or Hitachi SU-8230 (Hitachi, Pleasanton, CA) field emission scanning electron microscope (FESEM).

CryoSEM was done to capture the evolution of the coating microstructure during drying. Coatings were prepared and deposited onto 5 mm × 7 mm silicon substrates similarly to the SEM samples. But coatings were dried for different times and plunged into liquid ethane to freeze the specimen [87, 125]. Then the frozen samples were fractured and sputtered with platinum under the protected environment (Leica EM VTC 100 and ACE 600) and imaged using Hitachi SU-8230 equipped with a cryo-stage that maintained the temperature at -140 °C under high vacuum.

4.3 Results and Discussion

4.3.1 Coatings Prepared from GCC Suspensions

The stress development curves for coatings prepared from the larger sized GCC particles, samples N and W, are shown in Figure 4.2 and Figure 4.3, respectively. Both coatings contain only non-deformable GCC. For the coating prepared with a GCC dispersion having a narrow size distribution (Figure 4.2), the stress curve is comparable to those reported for coatings of monodisperse ceramic particles measured using walled cantilevers [103]; stress rises sharply as curved menisci form and relaxes after menisci retreat. The small residual stress is likely related to reprecipitation of dissolved calcium carbonate [143]. However, coatings prepared from dispersions of GCC with a wide particle size distribution (Figure 4.3), the stress shows a sharp rise, as expected, but then undergoes an intermediate relaxation, a rise to a second peak and incomplete stress relaxation. The irregular shape of sample W's stress curve can be explained by the non-uniformity in microstructure and drying.

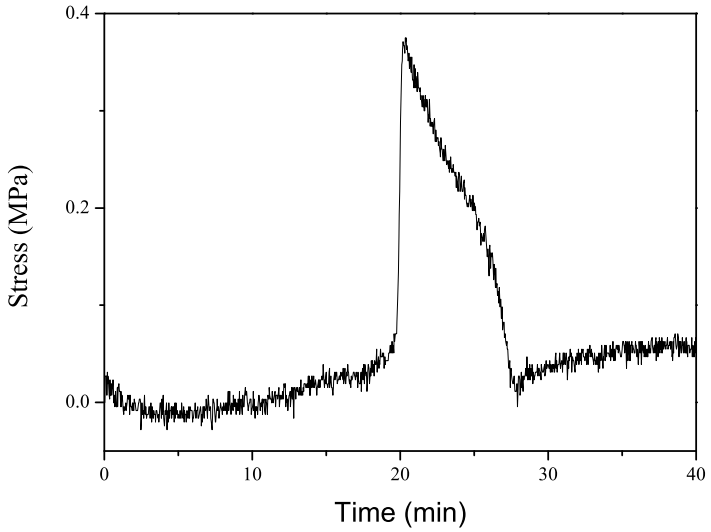

Figure 4.2: Stress development curve for sample N. Measurement was conducted using 40 μL suspension volume. Because of the low stress level, the system noise (prior to peak formation and after stress relaxation) of the measuring apparatus is apparent.

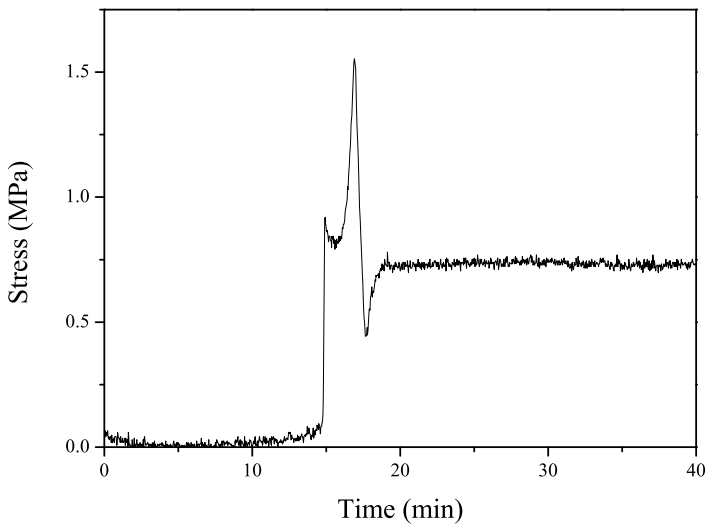

Figure 4.3: Stress development curve for sample W. Measurement was conducted using 40 μL suspension volume.

Cross-sectional SEM images of dried samples W and N are shown in Figure 4.4. A significant particle size gradient appears through the thickness of the coating prepared with the GCC-W particles. As a particulate coating dries, the distribution of particles through thickness early in the drying process depends on evaporation, diffusion and sedimentation [46]. For a given suspension and drying condition, the dominant process can be determined using drying regime map [46]. In an evaporation-dominated case, particles accumulate at the top surface; if sedimentation dominates, particles accumulate at the base; and when diffusion dominates, particles are uniformly distributed through the thickness. Particle size is an important variable determining the diffusion coefficient and sedimentation velocity. Based on analysis of the drying regime map for the conditions of our experiments, smaller GCC particles likely accumulate at coating surface during drying while larger GCC particles sediment. Therefore, the final coating microstructure has a particle size gradient from small to large through the cross-section. GCC-W contains a higher fraction of fine particles than GCC-N, and thus, coating W has a more significant particle size gradient than coating N, as shown in Figure 4.4.

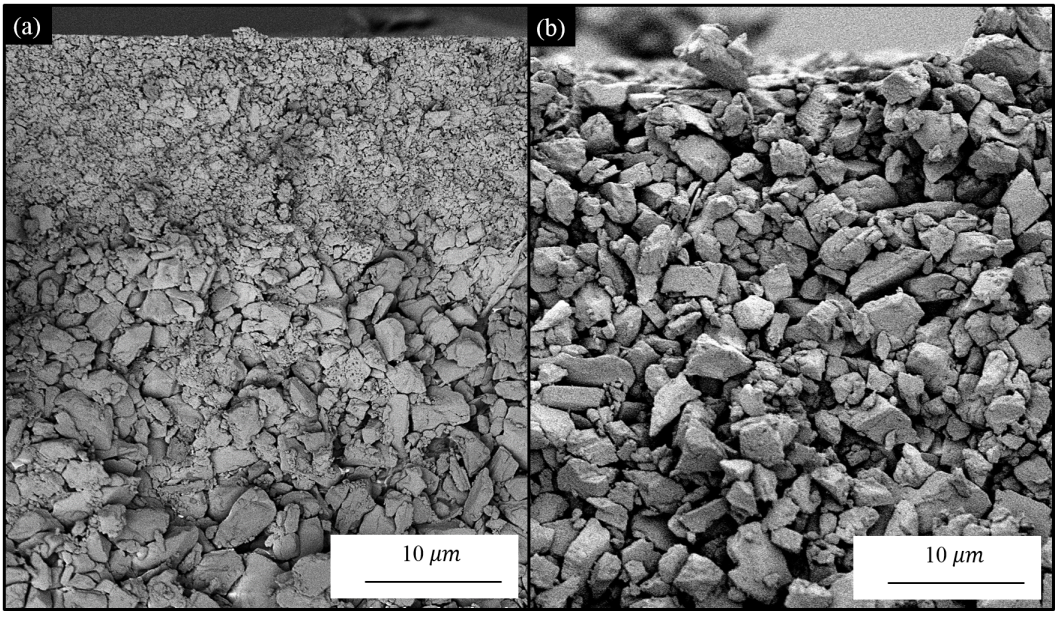

Figure 4.4: SEM cross-sectional micrographs for sample W (left) and sample N (right) dried at room conditions. Sample W shows a significant particle size gradient along thickness direction, while sample N has a relative uniform microstructure.

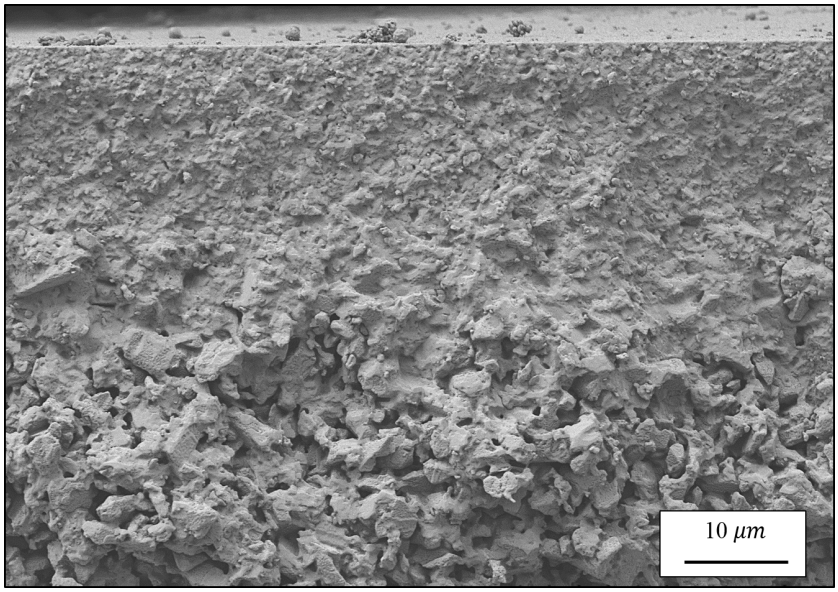

Figure 4.5: CryoSEM cross-sectional micrographs of sample W dried at 22°C, 6 RH% under nitrogen flow for 2 minutes before freezing.

The microstructural gradient influences the stress development in these GCC-only coatings. In the past research [103], CryoSEM results revealed that the sudden onset of stress development in ceramic particle coatings is triggered by the appearance of curved menisci in the saturated particulate network. Thus, the initial sharp increase in the stress of coating W is linked to this event, while the subsequent small decrease and higher stress peak indicate additional complexity that is likely resulted from the heterogeneous microstructure. Using CryoSEM, the microstructure of sample W was captured at an intermediate stage of drying, between the saturated state and the dried state (i.e., there was still water in the particulate network at the time of freezing). See Figure 4.5. At this stage in the drying process, the particle packing is established and the pores are partially emptied. Voids are especially apparent near the bottom of the coating. The comparison of Figure 4.6 clearly shows the difference between the microstructure of the dry coating (Figure 4.6b and d) and that of the partially dry coating the frozen microstructure (Figure 4.6a and c). Frozen water fills some of the pore spaces throughout; there appear to be tiny pores in the top section among fine particles (Figure 4.6a) and more significant empty pores in between large GCC particles

(Figure 4.6c) in the bottom section. Since large pores empty first during drying [147], [148], the movement of menisci is a function of pore size gradient. Therefore, the coating likely dried non-uniformly due to the gradient of pore size caused by coating Ws non-uniform microstructure. This non-uniformity influences the formation and movement of the menisci and the development of stress.

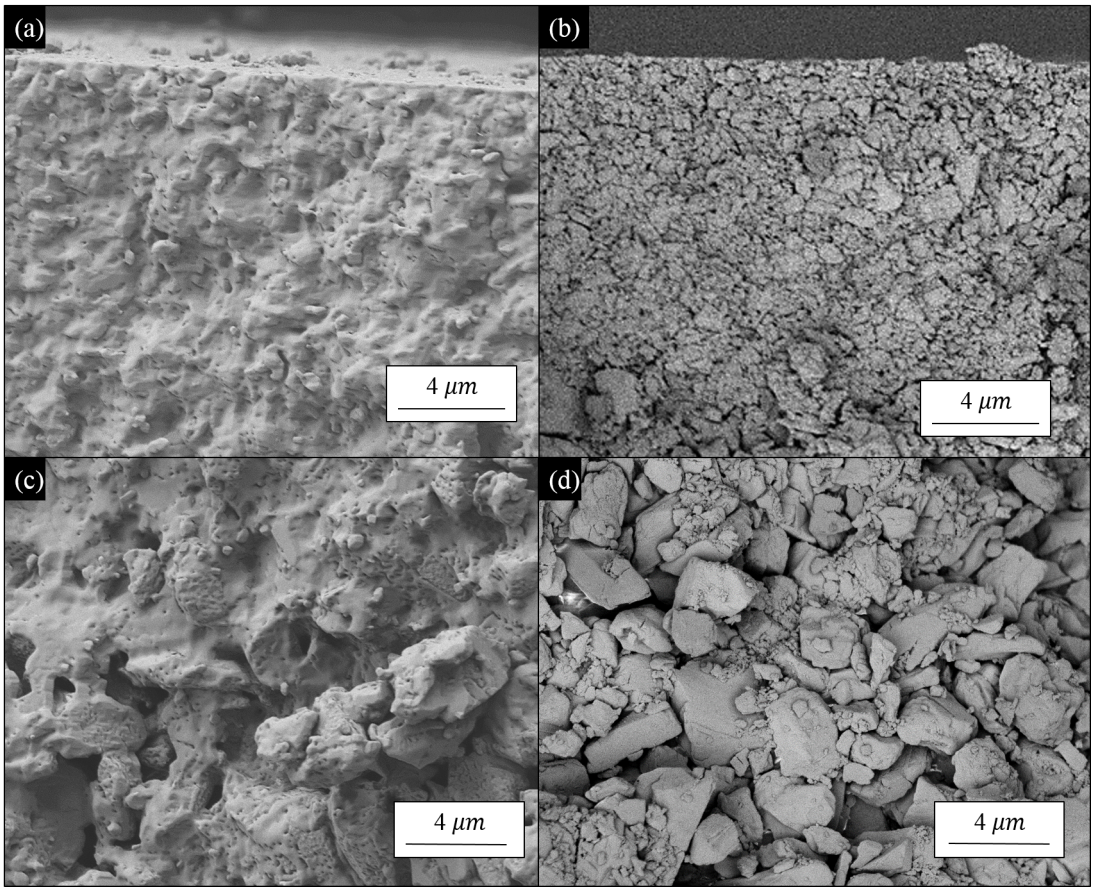

Figure 4.6: Comparison between coating Ws cross-sectional micrographs of partially dry sample (CryoSEM) and dry sample (SEM). CryoSEM of sample W dried at 22°C, 6 RH% under nitrogen flow for 2 min. (a) CryoSEM image of partially dry coating W at the top section; (b) SEM image of dry coating W at the top section; (c) CryoSEM image of partially dry coating W at the bottom section; (d) SEM image of dry coating W at the bottom section.

4.3.2 Coatings Prepared with GCC and Styrene Acrylate Latex

For coatings of non-deformable particles, organic binders are frequently added to improve green strength and crack resistance. Structure development during drying, including particle and binder distribution, is critical to coating performance. Coatings N-SA and W-SA contain non-deformable coarse GCC particles (GCC-N for sample N-SA, GCC-W for sample W-SA) and deformable styrene acrylate (SA) latex particles. Figure 4.7 shows the microstructure of W-SA, the coating with GCC-W and SA latex. Unlike the coating prepared from GCC-W alone (see Figure 4.4, this coating has a uniform microstructure with no GCC particle size gradient. The latex particles apparently interfere with sedimentation of the GCC particles in the early stage of drying. At the later stage of drying, the latex deforms and fills some of the pore space. Likewise, the N-SA coating (not shown) has a uniform microstructure.

With uniform microstructures, the stress development curves for samples W-SA and N-SA (see Figure 4.8) are similar in shape but quite different from the stress development curves for coatings prepared from GCC alone. As indicated by the two stress curves in Figure 4.8, there is no stress generation for the first five minutes of drying, indicating that the volume shrinkage due to evaporation is accommodated by particle rearrangement in the liquid coating. As drying continues, particles are brought closer to each other and eventually form an interconnected network. Curved menisci form between particles, leading to the capillary pressure that compacts the particulate network and causes latex particles to deform. Adhesion to the substrate constrains the shrinkage from particulate network densification and latex deformation, which leads to in-plane stress development. With further water removal, menisci descend into coating and air invades the pore space. At around 25 minutes of drying, stresses reach stable final values. At this point, the capillary force disappears as menisci retreat, but deformed latex particles provide the binding between GCC particles, preventing stress relaxation.

Although W-SA and N-SA have the same levels of coarse GCC particles and SA latex, the stress in W-SA is much higher than that of N-SA (see Table 4.2). The SEM micrographs in Figure 4.9 show the top views of coatings W-SA and N-SA. Coating W-SA contains more fine particles due to its wider particle size distribution and hence creates smaller pores than N-SA sample. Since the capillary effect is inversely proportional to the pore size, W-SA coating experiences stronger compaction of the particulate

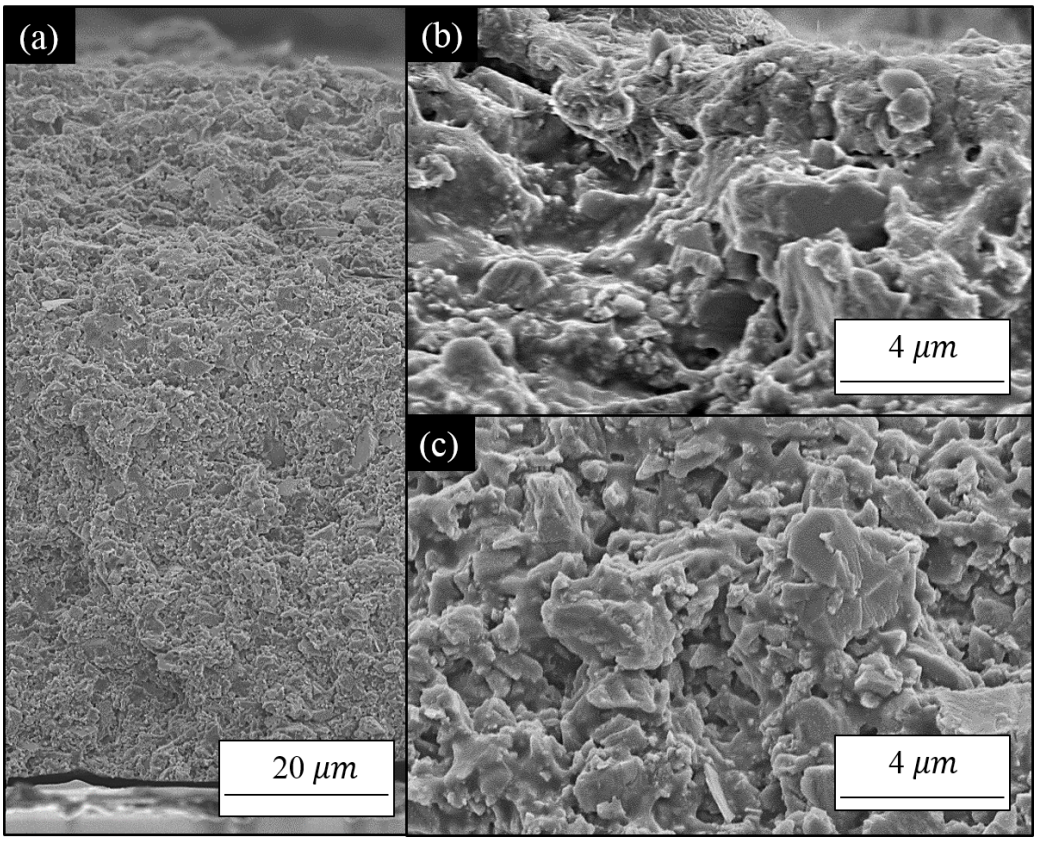

Figure 4.7: SEM cross-sectional micrographs for W-SA coatings dried at room condition. (a) low magnification cross-sectional view, (b) high magnification view at the top section, (c) high magnification view at the bottom section.

Table 4.2: Comparison of average stress for coatings prepared with GCC and SA latex with different particle size distribution.

Sample	GCC Type	Latex	Thickness (μm)	Stress (MPa)	Comment
W-SA	GCC-W	SA	64.9 ± 6.6	3.41 ± 0.26	no defects (40μL)
			43.3 ± 9.4	4.29 ± 0.95	no defects (30μL)
W-LSA	GCC-W	SA	74.2 ± 5.1	2.11 ± 0.12	no defects (40μL)
N-SA	GCC-N	SA	59.7 ± 6.8	1.16 ± 0.22	no defects (40μL)
FW-SA*	FGCC-W	SA	48.8 ± 9.4	4.32 ± 0.96	no defects (30μL)
FN-SA	FGCC-N	SA	52.2 ± 5.1	1.64 ± 0.29	no defects (30μL)

* Sample FW-SA cracks at 40 μL.

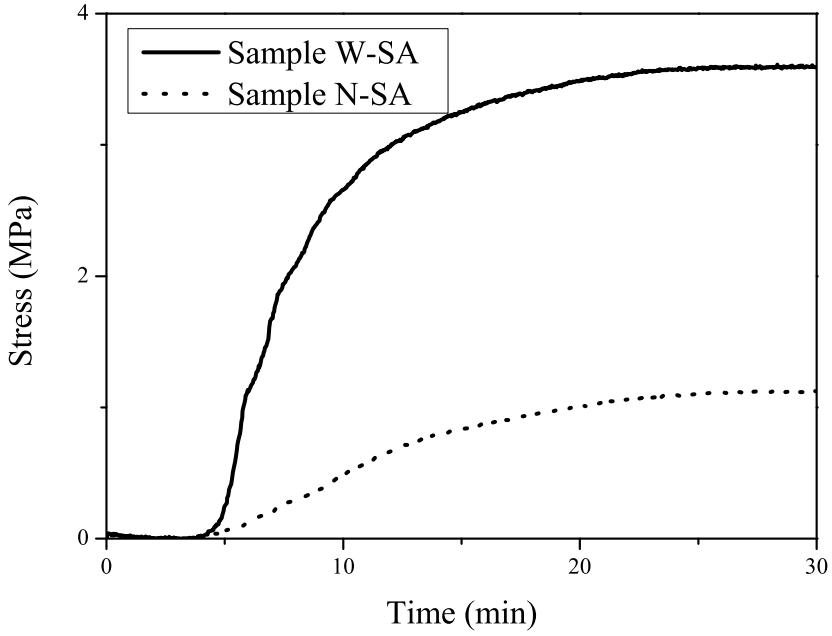

Figure 4.8: Effect of particle size distribution on stress development of coarse GCC and SA latex coatings. Measurements were done using 40 μL of suspension volume.

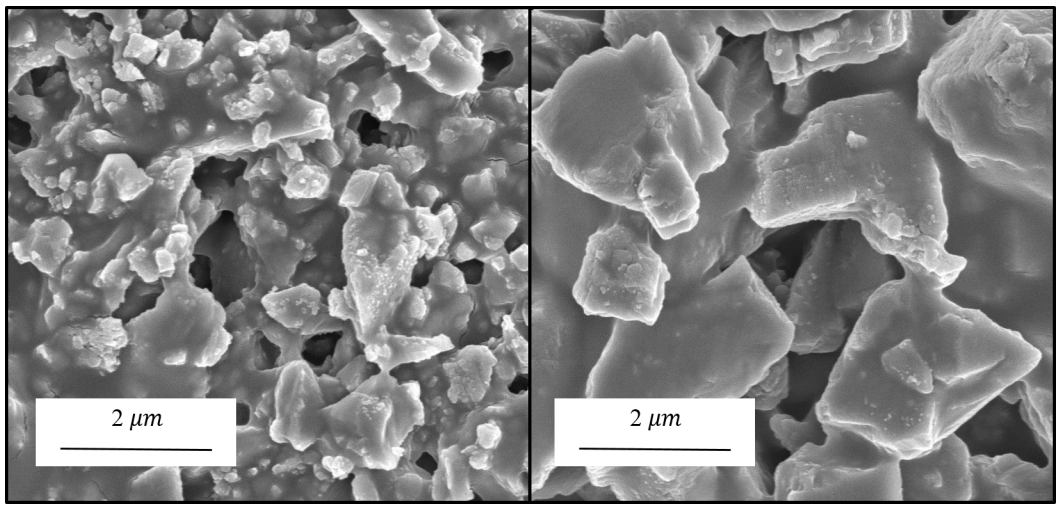

Figure 4.9: Comparison of SEM top view micrographs for samples W-SA (left) and N-SA (right) dried at room conditions.

network from capillary pressure during the drying process and higher final stress values. Moreover, the wider particle size distribution should result in higher GCC packing density and higher coating modulus. These factors lead to a higher final stress when the particle size distribution is broader.

Results from coatings containing fine GCC particles and SA latex (FW-SA and FN-SA) further confirm this trend (see Figure 4.10). Note that these data were taken with a lower suspension volume and hence a thinner coating. Therefore a shorter time is needed for drying and the coatings themselves are crack-free, a fact that helps in making comparisons between different formulations. The shape of the stress development with time is very similar to that shown for the coatings made from coarser GCC and SA latex (see Figure 4.8). The stress rises as capillary force compacts the coating. The intermediate small peaks that appear as the stress increases may be related to some relaxation of the capillary stress. These features varied from run to run and were sensitive to the drying conditions and thickness. Similar features in the stress curves of particulate coatings have also been noticed by other researchers [143]. Coating FW-SA has a wider particle size distribution and generates higher stress values than coating FN-SA.

The effect of latex content on stress development is shown via the comparison of sample W-SA and W-LSA. Coatings with higher latex content (sample W-SA) appear to develop a higher stress during drying, as shown in Figure 4.11. The higher amount of latex provides more binding in between the porous structure which reduces the pore size and enhances the mechanical property. Therefore, the higher level of stress is developed in the coating layer of sample W-SA due to possibly higher modulus and more strain resulting from capillary effect and particle deformation.

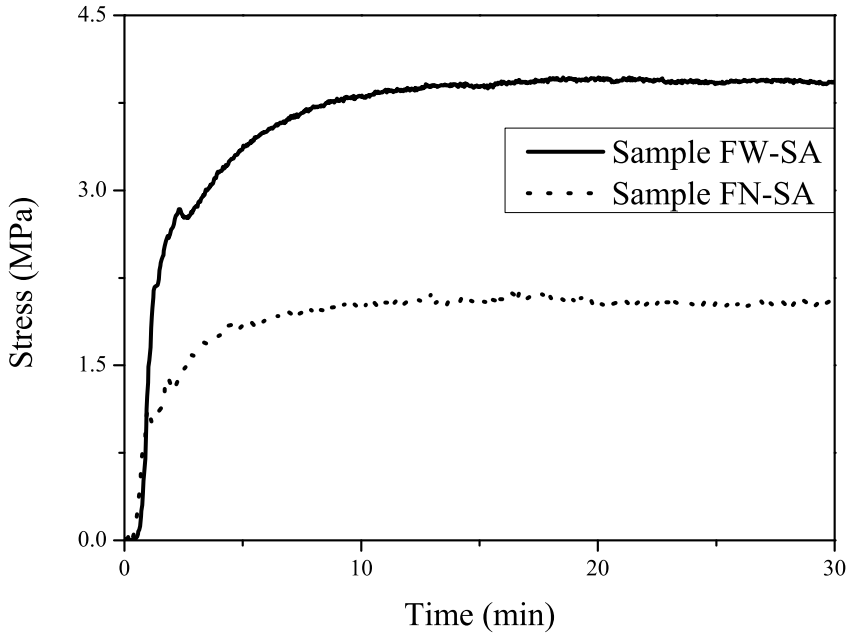

Figure 4.10: Effect of particle size distribution on stress development of fine GCC and SA latex coatings (FW-SA and FN-SA). Measurements were done using 30 μL of suspension volume.

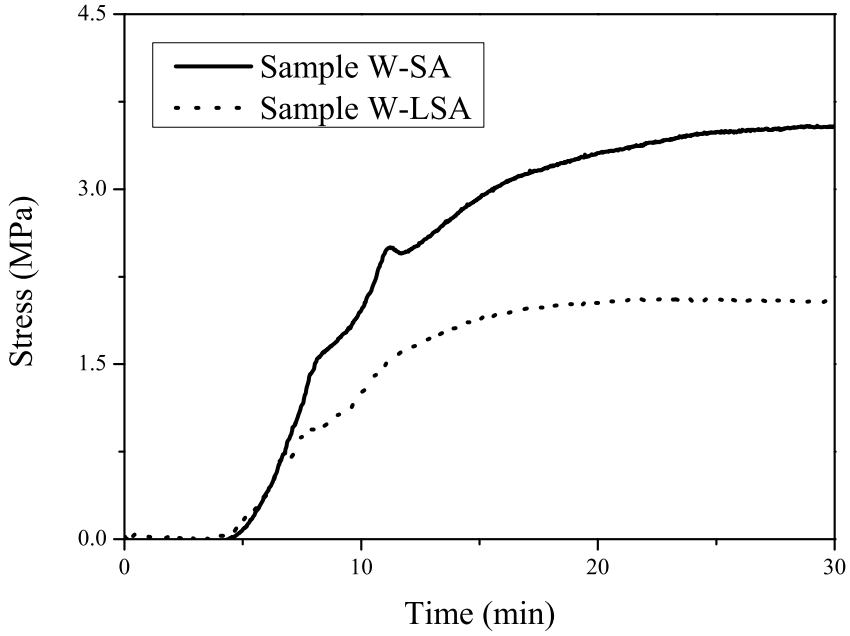

Figure 4.11: Effect of SA latex content on stress development of GCC and SA latex coatings (W-SA and W-LSA). Measurements were done using 40 μL of suspension volume.

4.3.3 Coatings Prepared with GCC-W and Different Types of Latex

In addition to SA, two other types of latex, polyvinyl acetate (PA) and styrene butadiene (SB), were studied to further reveal the effect of latex binder on coating stress development and cracking.

Table 4.3: Effect of latex binder type on the average stress and cracking behavior in GCC-W coatings. Measurements were conducted using 30 μL suspension volume.

Latex Properties			Coating Behavior			
Sample	Type	T_g (°C)	Stress (MPa*)	Thickness (μm)**	Drying temperature (22°C)	Drying temperature (4°C)
W-SA	Styrene acrylate	4	4.29 ± 0.95	43.3 ± 9.4	No defects	Cracks
W-SB	Styrene butadiene	15	3.44 ± 0.64	59.0 ± 6.4	Cracks & Delamination	Severe cracks &Delamination
W-PA	Polyvinyl acetate	34	2.36 ± 0.56	51.4 ± 3.8	No defects	Cracks

* Listed stress is the average stress level at 30 minute drying under 22°C.
** Thickness is measured on coatings dried at 22°C.

Stress measurement results for coatings W-SA, W-PA and W-SB along with the latex properties are listed in Table 4.3.3. Latex with a T_g lower than the drying temperature is considered to be soft latex (e.g., styrene acrylate and styrene butadiene in samples W-SA and W-SB). The SEM images in Figure 4.12 show that the soft latex better fills the space in between GCC particles compared to the hard latex (W-PA). Coatings prepared with GCC and soft latex undergo more deformation during the drying process, which should lead to a larger amount of constrained volume shrinkage and potentially higher stresses. Concurrently, stronger contacts between GCC particles are expected with softer latex [149, 150, 151]. Therefore, the particulate network is better glued together to prevent stress relaxation due to water evaporation. Unfortunately, the W-SB cracked and so the stress value listed in Table 4.3.3 is less than that which would have been observed in a crack-free coating and so comparing W-SA with W-SB is not possible. Coating W-PA, on the other hand, contains a relatively rigid latex, polyvinyl acetate. During drying, sample W-PA has less latex deformation, leaving larger pores between GCC particles and contributing less to the constrained shrinkage, which results

in a lower stress level. It should be noted that the stress development is also expected to depend on the relative amounts of GCC and latex in the coating formulation; this variable was constant in this study.

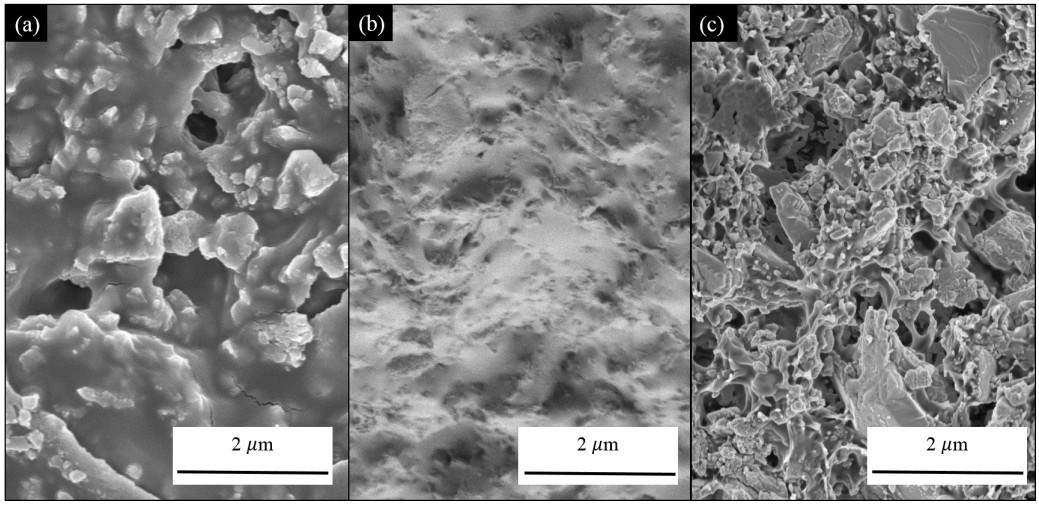

Figure 4.12: SEM images a) sample W-SA, coating with soft latex and develops high stress b) sample W-SB, coating with soft latex and develops high stress and c) sample W-PA, coating with hard latex and develops low stress

Figure 4.13 shows differences in the stress development data for the GCC-W coatings containing soft and hard latex. For all three samples, the stress increases after some initial drying. This increase is likely triggered by a capillary effect in which the curved menisci form in the particulate network. Coatings containing soft latex (W-SA and W-SB) reach a higher stress value because they undergo a greater extent of deformation [149], causing more constrained shrinkage. The shape of the curve following the initial stress increase is different: coatings contained soft latex show a slow upturn in the stress development, while the stress in the coating with hard latex (W-PA), on the other hand, slowly declines. The gentle rise in the soft latex coatings is likely caused by continued latex deformation and volume shrinkage. And the decline is likely related to continued loss of capillary-induced stress. However, the stress measurements studied here were conducted only during coatings drying period. There is no investigation into coatings stress level hours or days after drying completes. The impact of latex glass transition temperature in coatings stress level in long term may be influenced by mechanical

properties of the latex and environment conditions.

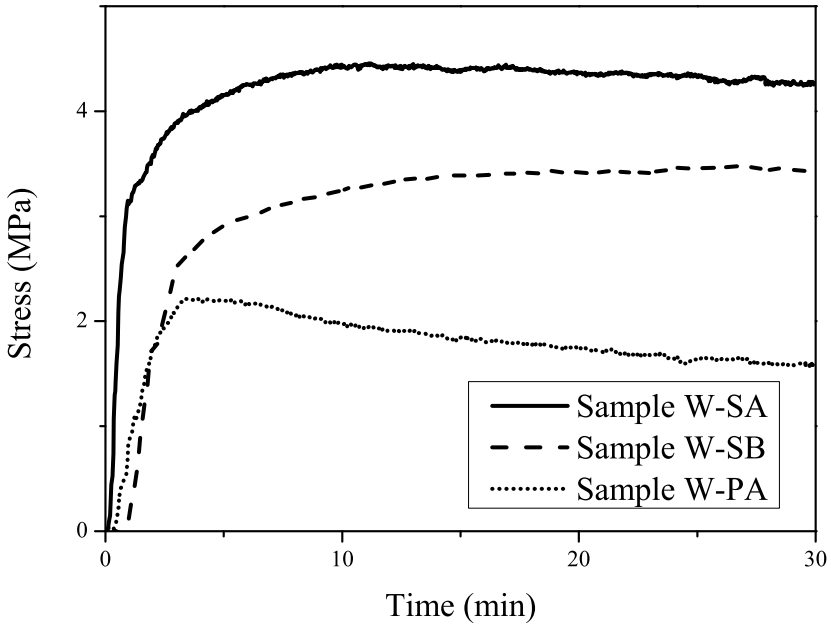

Figure 4.13: Comparison of stress development curves for GCC-W coatings with different types of latex addition. Measurements were conducted using 30 μL suspension volume. Sample W-SB is cracked and delaminated.

The cracking behavior of GCC-W coatings with different latex types was explored under two drying temperatures (see Table 3). When drying at 22°C, coating W-SB ($T_g = 15$°C) cracks and delaminates while W-SA ($T_g = 4$°C) has no defects. Both types of latex deform during drying but the coating with SB latex likely has less deformation, leading to less binding between particles and lower resistance to cracking. Additionally, thicker coatings (40 μL) prepared with PA, the hard latex, also cracked. In this case also, a lower amount of latex deformation likely created a weaker coating overall. When drying at a low temperature (4 °C), below the glass transition temperature of all latex binders, all three coatings crack. However, the reason sample W-SB has the most severe cracks cannot be fully understood by considering latex glass transition temperature alone. This observation indicates that the latex characteristics (i.e., molecular weight

of the polymer, the degree of branching of the polymer chains, latex particle size and morphology [12], [34]) also impact the coating mechanical strength and toughness.

4.3.4 Coatings Prepared with GCC-W, SA Latex and Different Additives

The effect of PVOH additive is revealed by comparing samples W-SA and W-SA-P. The stress curves for these two samples are plotted in Figure 4.14. These results show that the sample without PVOH reaches a stable stress value of 3.5 MPa in around 30 minutes, while the sample with PVOH reaches stress as high as 8.5 MPa after drying 80 minutes. This result clearly indicates that 1.22 vol% PVOH causes high stress and slows drying. In this coating the constrained shrinkage from the PVOH phase amplifies the stress, a trend noted in stress studies of polymer-solvent coatings [31].

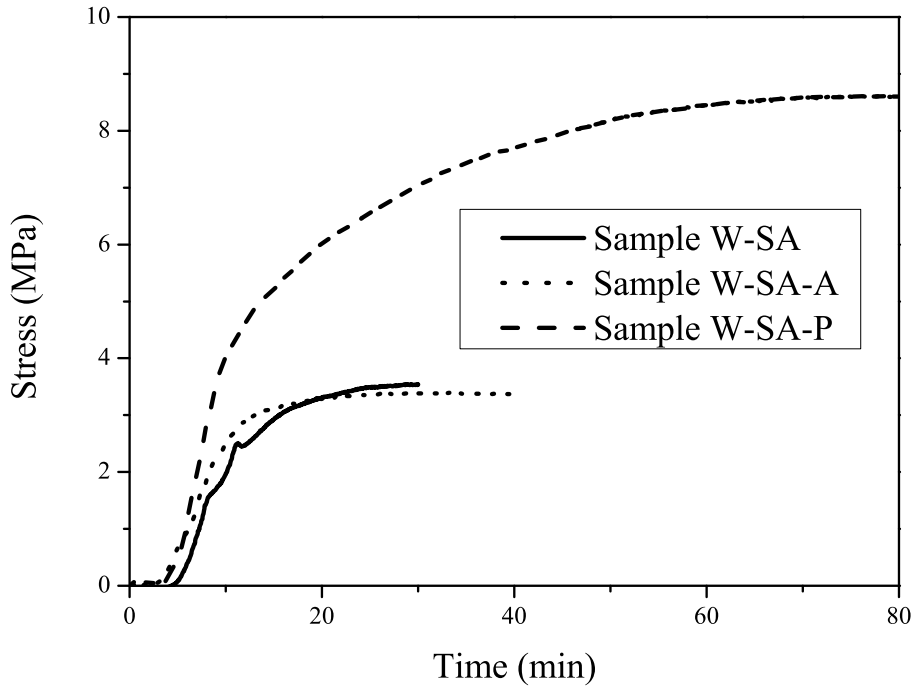

Figure 4.14: Comparison of stress development curves for GCC-W coatings with different types of additives. Measurements were conducted using 40 μL suspension volume.

The opposite trend in stress measurement is found by studying the effect of Alco additive (ethyl acrylate), which is normally used as a rheology modifier. By adding Alco, the widely distributed GCC coatings, sample W-SA and sample W-SA-A (see Figure 4.14), have no significant difference in stress development. Other additives (starch and nanoclay) which are particularly used in paper coating formulations were tested using particulate suspensions prepared from GCC-W and SA particles, which is presented in Appendix C.

4.4 Summary

In ground calcium carbonate (GCC)-based coatings, particle size distribution influences coating stress development and microstructure evolution. For coatings containing only GCC particles, a wide particle size distribution resulted in an inhomogeneous microstructure and irregular stress development behavior for the conditions we investigated. Latex addition improves the uniformity of coating microstructure. GCC-latex coatings prepared with GCC having a wide distribution in particle size have a higher stress than those prepared with GCC having a narrow distribution. In this case, the higher stress is related to the particle packing that results in smaller pore sizes, larger capillary pressures that drive compaction and a higher coating density. In coatings prepared with the same GCC particles but different latex binders, the stress and cracking behavior of the coating depend on the latex properties. With the specific latex types and coating compositions explored in this study, adding more latex content or using the latex with lower glass transition temperature (T_g) provides better contact between GCC particles and results in coatings that develop higher stress levels on drying. However, these latex's impact on coating stress level in long-term was not investigated in this work and requires further study.

4.5 Acknowledgement

The authors would like to gratefully acknowledge support from the WestRock Company and the industrial supporters of the Coating Process Fundamentals Program of the Industrial Partnership for Research in Interfacial and Materials Engineering (IPRIME).

Acknowledgements also go to Gary Fugitt, Kyle Price, Chris Frethem, and Wieslaw Suszynski for their contributions to this project. Parts of this work were carried out in the Characterization Facility, University of Minnesota. The Hitachi SU8320 CryoSEM and Cryo-specimen preparation system were provided by NSF MRI DMR-1229263.

Chapter 5

Effect of Clay Addition to Irregular-shaped Particulate Coatings

Abstract—Particle characteristics are essential for the formulation of particulate coatings. Particles with different material properties, size, size distribution, and shape provide coatings with various mechanical, electrical, and optical properties. Additionally, particle characteristics can significantly impact the particle dispersion, as well as the drying and cracking behavior. In Chapter 4, study of coatings made from suspensions of wide particle size distribution was presented. In this chapter, the study of the effect of particle properties on performance is continued by exploring the effect of particle shape, using suspensions of irregular-shaped particles (ground calcium carbonate) with different levels of plate-shaped clay particles and constant level of latex binder particles. The drying behavior, including weight loss, stress development, microstructure formation, and shrinkage, were studied using beam deflection method, SEM/cryoSEM and laser profilometry. The cracking behavior was studied by measuring the critical cracking thickness. The objective of this study is to understand the effect of particle shape on drying and cracking, which can provides a better guidance to the formulation development and optimize coating performance. [1]

[1] Some work introduced in this chapter is under preparation for publication.

5.1 Background and Motivation

Clay and clay minerals are used in a variety of applications; they are central to some ceramics, are added to paper and paint, and their properties make them suitable as chemical barriers, liquid barriers and catalysts. [76, 152, 153] Kaolin, as the prototypical clay mineral, is one of the most widely used pigments in the paper industry and exploited in a wide range of coating applications. [154, 155] The physical and chemical properties of the kaolin can improve the performance of particulate coatings applied on paper and paperboard, imparting desired appearance, printability, mechanical and barrier properties. [13, 156, 157]

Paper coatings are typically prepared from aqueous particulate suspensions containing a mixture of kaolin clay and ground calcium carbonate (GCC), along with binder, dispersants and other additives [76]. The hard particles in the formulation, such as GCC and clay, are often called pigments. The coating formulation, including the characteristics of the components and their relative amounts, influences the final coating properties. With the pigments representing 80-95 wt% of many paper coating formulations [32], understanding the role of pigments on drying and performance of the coating is essential.

Past studies have investigated the impacts of the properties of clay pigment on the coating structure [13, 154], printability [158, 159], optical [156, 160, 161] and mechanical properties [162, 163, 164]. The importance of the particle size, shape and surface chemistry of clay pigments to the final coating performance, including the porous structure [76, 77, 165], reflection coefficient [154, 158], surface roughness [32, 166, 167], and capillarity-based ink absorption [13, 154, 159], is well-recognized by many researchers. The effect of clay pigments has also been investigated in coating systems with different blending of pigments and binders [77, 156, 165, 168]. In studies of coating systems that blend kaolin clay with GCC pigments and binders, several researchers [162, 163, 164] have found that increasing the clay content enhances in-plane tensile and printing strength of coatings, as well as the bending stiffness, and this reinforcement is increased with clay aspect ratio.

However, little research has been done on the influences of clay addition on the dynamic changes that occur during the drying process, especially the stress development,

shrinkage and cracking performance. In this study, the effect of clay is investigated by varying the blending ratio of the plate-shaped clay particles to irregular-shaped GCC particles. In addition to coating structure and properties, *in-situ* stress development, dynamic microstructure formation and cracking are explored. Previous work introduced in Chapter 4 [89] investigates the stress development and microstructure formation of coatings contained GCC particles of different particle size distribution and binders. That study showed that with similar average particle size, coatings prepared from particles with a wide particle size distribution formed a more compact microstructure, but was prone to cracking due to high tensile stress development on drying. In this work, the addition of clay particles is found to greatly suppress the cracking issue.

5.2 Materials and Methods

5.2.1 Suspension Systems

Table 5.1: Solid compositions of five coating dispersions given in volume percent.

Sample	Fine GCC	Clay	Latex	Total Solid
GCC:clay-100:0	29.19	-	15.07	44.26
GCC:clay-75:25	21.89	7.43	15.15	44.47
GCC:clay-50:50	14.75	14.86	15.13	44.56
GCC:clay-25:75	7.45	21.82	15.07	44.34
GCC:clay-0:100	-	29.19	15.07	44.26

The coating system investigated in this study was aqueous suspensions prepared from fine ground calcium carbonate (GCC), styrene acrylate latex (Acronal-S504, BASF, approximate particle diameter of 0.2 μm, glass transition temperature, $T_g, = 4°C$) and clay particles (Kaofine 90, Thiele, ratio of particle diameter to thickness is between 5 to 10, mean particle diameter of $\sim$ 0.2 μm [169]). The fine GCC particles (Hydrocarb 90, Omya) used were polydispersed, irregular-shaped particles with average particle size of 750 nm. Five formulations were investigated, as listed in Table 5.1. All contain a constant level of styrene acrylate latex and the same total amount of fine GCC and clay particles. The pigment volume concentration (PVC) is constant at $\sim$ 0.66, which is above the typical critical pigment volume concentration (CPVC) for coatings of this type. Therefore, the final coatings are porous. All coating dispersions are kinetically

stable [170] (pH of GCC-based coatings are 7.5-8), and all samples were sonicated for 10 minutes prior to deposition.

5.2.2 Drying Stress Measurement

The dynamic stress development of the coating was characterized using a beam deflection method [2, 146] with a polydimethylsiloxane (PDMS) walled cantilever [103]. The measurement takes place in a drying chamber with controlled temperature and relative humidity using nitrogen gas. Uniform drying with suppressed drying front movement was observed during the test using walled cantilevers [103]. The deflection of the substrate free end in response to the stress developed in the coating layer is measured using laser and detector.

In a typical experiment, 40 L of liquid suspension is applied onto the walled cantilever substrate (5 mm $\times$ 45 mm coating area), which is plasma cleaned (Harrick Plasma Inc., Ithaca, NY) for two minutes before use. All stress measurements were conducted at 23 °C $\pm$ 1°C and RH of 6 % $\pm$ 2% controlled by nitrogen flow. For each sample, 6-8 repeat runs were conducted. Representative stress development curves are reported, as well as the final and peak stress values with an error based on a 95% confidence interval.

5.2.3 Microstructure Characterization

Scanning electron microscopy (SEM) and Cryogenic SEM (CryoSEM) were used to characterize coating microstructure after and during drying. Coatings were prepared on 5 mm $\times$ 7 mm silicon substrates, which were pre-scored to achieve more reliable fracture. Similar deposition procedure as that used to prepare coated cantilevers for stress measurement was used here; however, the coatings here were dried at room condition (23 °C $\pm$ 1°C and RH of 40 % $\pm$ 5%). For CryoSEM samples, coatings were left drying for different times and plunged into liquid ethane to vitrify the specimens [87, 125]. Then the frozen samples were transferred to liquid nitrogen and mounted in a specimen holder. The holder, at liquid nitrogen temperature, was transferred to a cryo-preparation system where the coatings were fractured and sputtered with platinum under the protected environment (Leica EM VTC 100 and ACE 600). For both SEM and CryoSEM samples, approximately 10 nm of platinum was sputtered onto the

coating surfaces to reduce charging during imaging. The samples were imaged using Hitachi SU-8230 (Hitachi, Pleasanton, CA) field emission scanning electron microscope (FESEM).

5.2.4 Critical Cracking Thickness (CCT) Measurement

Coatings were deposited onto 5 mm × 45 mm walled silicon substrates with varied thickness and dried at room condition (23 °C ± 1°C and RH of 40 % ± 5%). The thickness was regulated by the amount of coating suspension deposited onto the substrate and measured after drying completed. In this test, the drying of the coating occurs uniformly with little lateral drying effect. The thickness was recorded as the critical cracking thickness when cracking was first observed in the sequence of samples with increasing amount of suspension deposition. The crack is observed by eye without microscopy. Due to the liquid pinning of the substrate wall, the edge of the coating is slightly thicker than the rest of the coating area. Hence cracks form preferentially at these thicker regions. The coating is considered "cracked" when cracks appear over more than one eighth of the coating width.

5.2.5 *In-situ* Thickness Measurement

A laser profilometer (KEYENCE LJ-V7001) was used to track the cross-section profile of drying coatings. As discussed in Chapter 3.3, the full cross-section of the center of the coating is measured to get one center point measurement using H orientation. The thickness of the coating layer was recorded every 10 seconds for the first 15 minutes of the drying process and then recorded every 20 seconds until 3 minutes after the tested sample reached final thickness. Plotting the thickness change as a function of time, the slope and the time of the thickness to first reach the minimum thickness value are considered to be the shrink rate and the shrink time. All samples were tested using same 5 mm × 45 mm walled silicon substrate under room condition (23 °C ± 1°C and RH of 40 % ± 5%).

5.3 Results and Discussion

The drying process of coatings with different GCC-clay blending ratios is studied to reveal the impact of plate-like shape of clay pigments on the coating drying and final performance. The cracking thickness and pattern, as well as the microstructure of the dried coatings, were compared among formulations. The difference in mechanical properties indicated by the cracking behavior was then further investigated via the dynamic changes of coatings during drying, including stress development, microstructure formation and particulate network shrinkage.

5.3.1 Cracking and Microstructure of Dried GCC-Based Coatings with Clay Addition

The images shown in Figure 5.1 are the crack patterns of four GCC-based coatings. All four coatings were coated using a blade coater with a 50 mil gap on the PET film (Polyethylene Terephthalate) and drying under room condition of 23 °C and 38 %RH. As indicated by the cracking patterns, fewer cracks are observed as the relative amount of clay increases (GCC-clay ratio decreases).

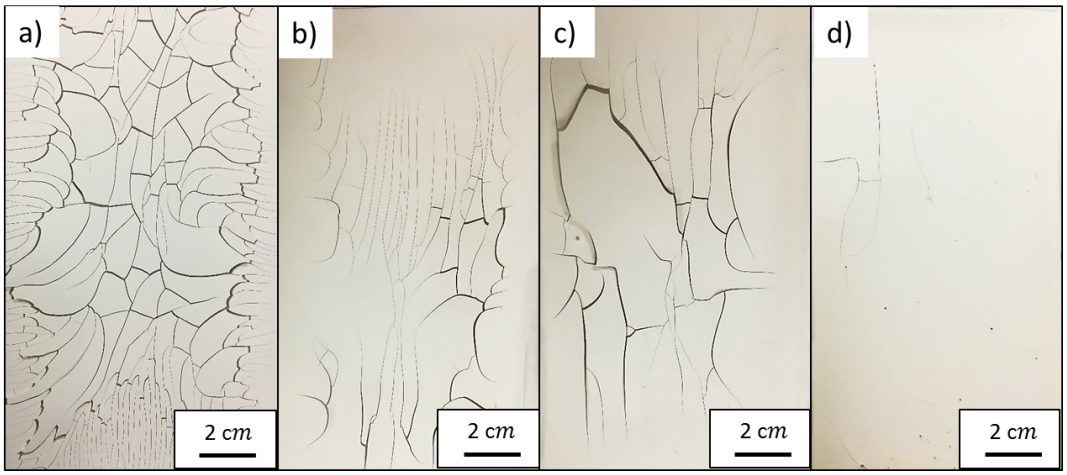

Figure 5.1: The cracking pattern observed on dried coatings with different GCC-clay blending ratio. (a) GCC:clay-100:0, (b) GCC:clay-75:25, (c) GCC:clay-50:50 and (d) GCC:clay-25:75. Drying is conducted under room condition.

In addition to the cracking pattern, the critical cracking thickness (CCT) of these

samples were measured using walled silicon substrate as the indicator of cracking resistance. As shown in Table 5.2, coatings with a higher level of clay contents have significant higher CCT. Therefore, coatings prepared with irregular-shaped GCC particles have improved cracking resistance with the increased level of clay content. Similar cracking improvements due to clay addition were also observed by other researchers [157, 171]. The plate-like shape of the clay particles are found to improve the in-plane tensile stiffness and strength which reinforce the coating in the loading or constrained drying shrinkage direction. [164, 172]

Table 5.2: CCT of coatings made from the five GCC-latex-clay dispersions with different level of clay additions under room condition.

Sample	GCC:clay-100:0	GCC:clay-75:25	GCC:clay-50:50	GCC:clay-25:75	GCC:clay-0:100
CCT (μm)	89 $\pm$ 20	137 $\pm$ 20	178 $\pm$ 20	220 $\pm$ 20	371 $\pm$ 20

To further investigate the performance indicated by the dissimilar cracking behavior, the microstructure of the coatings was compared. As demonstrated in Figure 5.2a, sample GCC:clay-100:0 contains GCC particles with wide particle size distribution and size around 0.5 - 1 μm. However, due to the coverage of the deformed latex, the edges of the GCC particles are not very distinct. In Figure 5.2b, some large clay particles can be observed in the cross-section of sample GCC:clay-75:25. But as the image shows, the contrast between GCC particles and clay particles is small, which makes them hard to distinguish from each other, especially with the coverage of the deformed latex. Likewise, GCC:clay-50:50 and GCC:clay-25:75 are similar in appearance but increasing amount of palte-like clay particles can be discerned, as shown in Figure 5.2c and 5.2e, respectively. With a higher magnification image (Figure 5.2d), some of the large GCC particles can be recognized. As shown in Figure 5.2, all five samples have the porous structure. With decreasing GCC-clay ratio, more clay particles can be observed in coating microstructure, but no significant difference is found in the porosity structure.

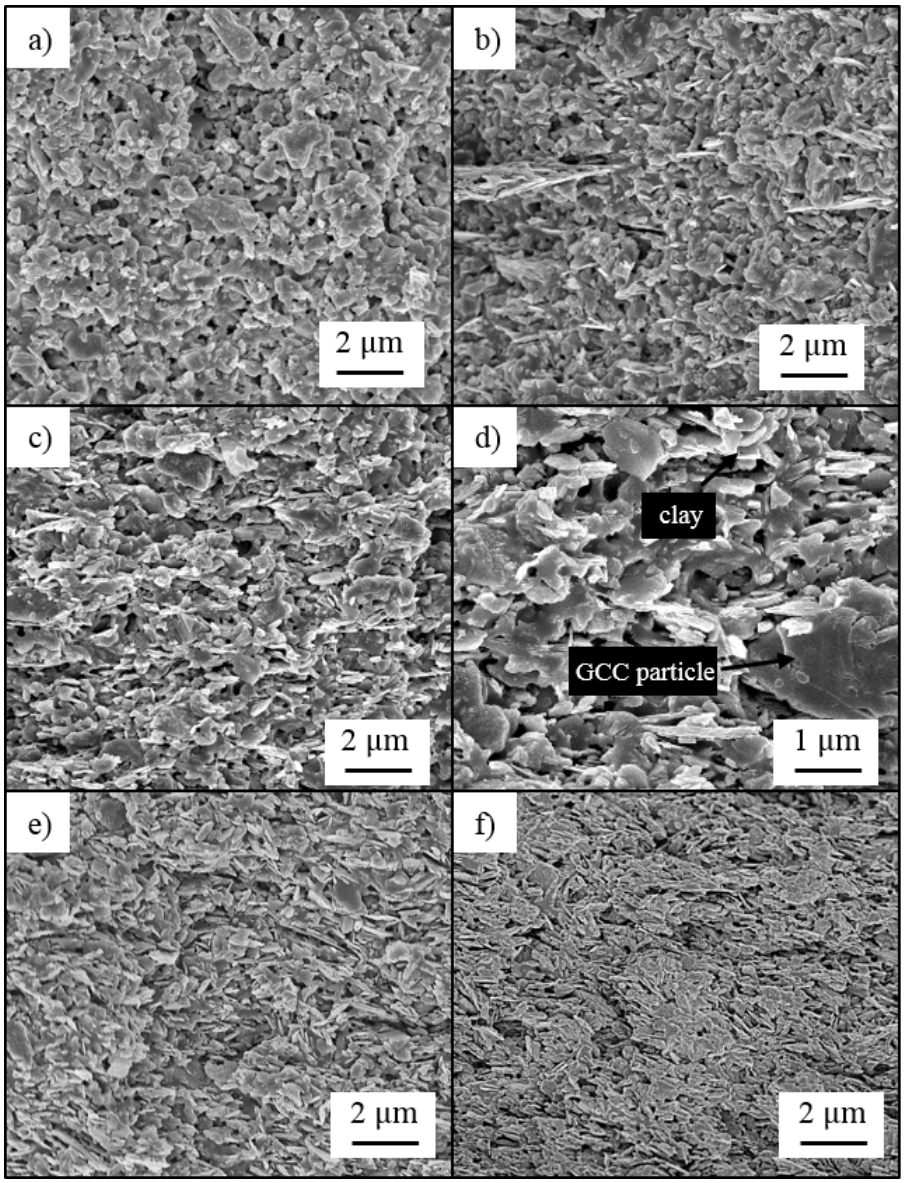

Figure 5.2: SEM cross-sectional micrographs of GCC-based coatings with different GCC-clay blending ratio. (a) GCC:clay-100:0, (b) GCC:clay-75:25, (c) GCC:clay-50:50, (d) GCC:clay-50:50 with higher magnification, (e) GCC:clay-25:75 and (f) GCC:clay-0:100. Drying is conducted under room condition.

5.3.2 Stress Development and Microstructure Evolution During Drying

The final performance of GCC coatings varies with clay addition; therefore, the dynamic changes during drying were characterized. Figure 5.3 shows representative stress development curves for GCC-clay coatings dried under controlled conditions (23 °C ± 1°C and RH of 6% ± 2%). Stress data show all coating formulations have a similar features. Initially, there is no stress for a short period, followed by a stress rise and a peak, and then slower stress increase to the final value.

With the same contour of the stress development curves, a slight decrease in the stress magnitude was observed with increasing clay content when analyzing the average values of all trials of measurements. More than 6 trials of stress measurement were conducted for each formulation. The average values for initial peak stress and final stress magnitudes (after 30 minutes of drying) are listed in Table 5.3.2, together with the thickness of dried coatings. Considering first the GCC-clay coatings with both GCC and clay present, the data show that both the peak and final stress values decrease with increasing amount of clay. The GCC-only coating cracked during measurement and hence the stress values listed in the table are likely lower than the actual stresses in an uncracked coating [89]. The clay-only coating experienced a higher stress peak than the GCC:clay-25:75 coating but followed the trend of lower final stress with increasing clay content exhibited in the coatings with both GCC and clay. Therefore, increasing the clay addition to lower the stress development of GCC-based coatings is considered as a general trend, although the trend is not significant with the variations between trials taken into consideration. The decrease in the stress values is possibly due to the lower capillary pressure resulting from an increase in pore size as the plate-shaped clay is added.

The formation of the stress peak in GCC-clay coatings shown in Figure 5.3 is different from the results for coatings prepared from dispersions of ceramic (hard) particles alone [89, 146, 2] and latex (soft) particles alone [125, 149, 31]. For coatings of only non-deformable particles, such as the silica-only coatings studied in the work of Price and coworkers [103], the stress development curve has a peak, where the stress rises due to capillary forces induced by curved menisci formation and then stress goes down to nearly zero as drying continous and menisci retreat. By contrast, the stress in

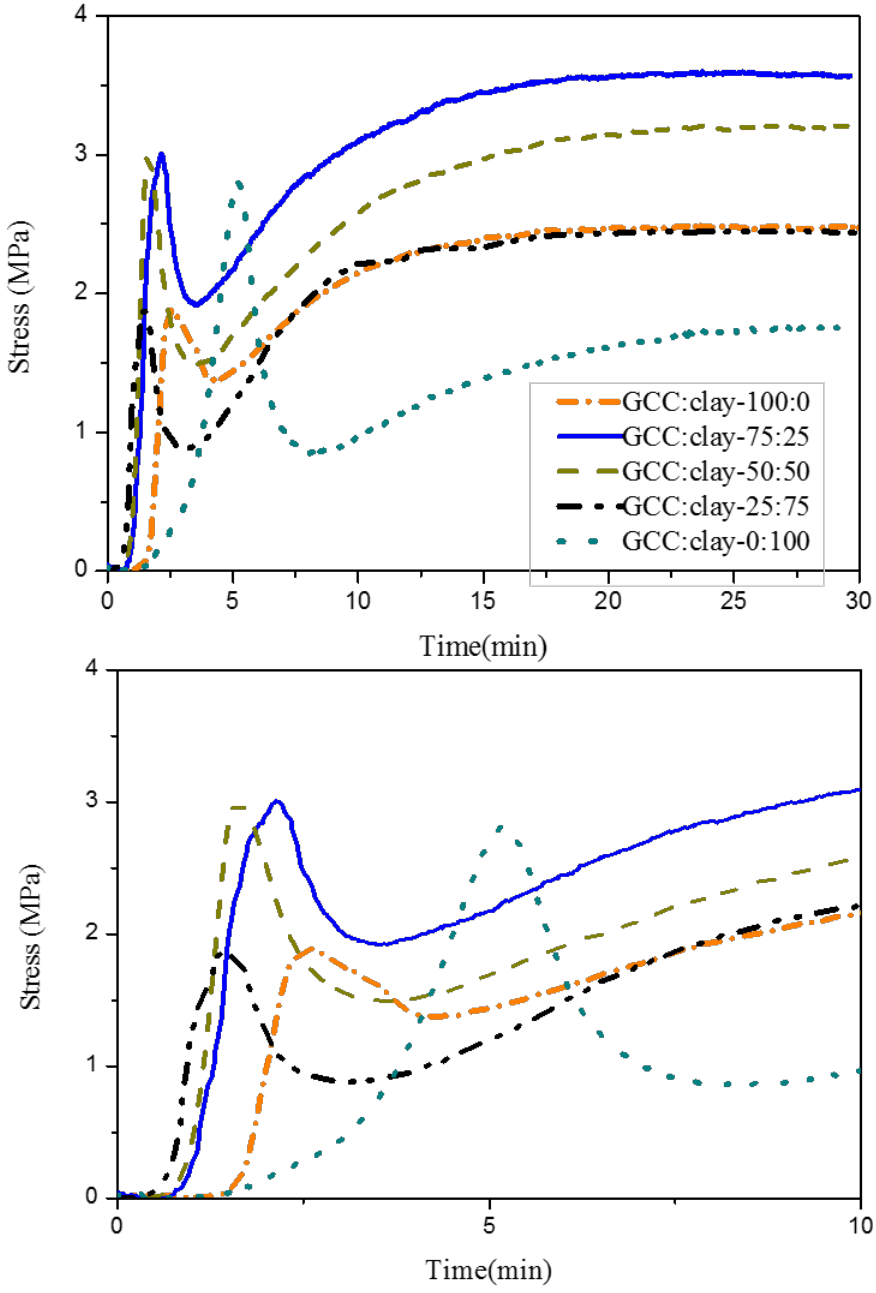

Figure 5.3: Stress development curves of coatings with different GCC-clay blending ratio. The curves are chosen from at least six trials measured for each composition. The plots on the bottom are the same curves given in the top one but showing only the early stage of stress development.

Table 5.3: Stress measurement results of five GCC-latex dispersions with different level of clay addition.

Sample	Stress (MPa)		Final thickness
	Peak	Final	(μm)
GCC:clay-100:0*	2.21 ± 0.16	2.54 ± 0.22	76.99 ± 6.76
GCC:clay-75:25	2.65 ± 0.22	3.40 ± 0.26	70.71 ± 6.47
GCC:clay-50:50	2.37 ± 0.14	3.03 ± 0.12	76.07 ± 8.73
GCC:clay-25:75	1.91 ± 0.19	2.68 ± 0.16	76.86 ± 6.67
GCC:clay-0:100	2.30 ± 0.39	1.53 ± 0.17	86.86 ± 5.69

* Cracking was observed in the measurement of sample GCC:clay-100:0 which results in slightly lower stress values.

coatings containing soft particles increases gradually and is retained after the coating dries completely. For example, in the latex coatings [113] in which the glass transition temperature of the particles is much less than the drying temperature, or in a coating containing both rigid particles and soft particles [89, 145, 143], the soft particles deform in response to the capillary effect. In these cases, the constrained shrinkage is permanent due to the deformation of the particles and stress does not decrease in the later stages of drying. This peak is not seen when GCC is larger (Stress data discussed in Chapter 4, Figure 4.8), which is likely due to the low capillary stress overall (see Figure 4.2). In the work of Wedin *et al.* [143], the stress development of the coating containing both rigid silica and soft latex was found to have both stress peak and retained stress after drying, but the stress partial relaxation followed by gradual increase has never been observed.

The stress peak that forms during drying of GCC-based coatings is very likely caused by the time lag between the capillary-induced stress development and latex deformation-induced stress development. This idea is supported by the results correlating stress development with weight change and thickness reduction during drying. As shown in Figure 5.4, the time when the coating thickness reaches its minimum value, indicating a compact particulate microstructure and the formation of the curved menisci, corresponds to the stress peak. There is continued weight loss beyond this point, as water is removed from the pore space and the stress decreases as the menisci descend and less of the coating is under the influence of the capillary force. Meanwhile, an increase in the coating thickness was observed after the coating reached minimum value. This possibly

results from the relaxation or "bounce back" of the particulate network after capillary forces disappear with the menisci. The subsequent increase in the stress that occurs in the final stages of drying appears to be related to latex deformation.

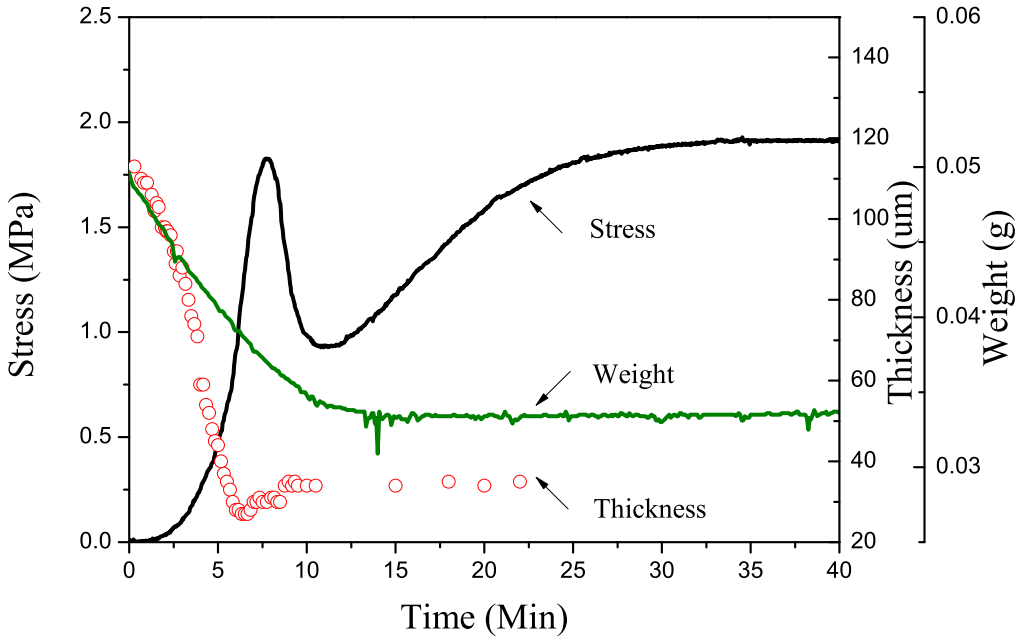

Figure 5.4: Stress development curve of GCC:clay-50:50 coating is plotted against weight loss curve and thickness change curve. All measurements were measured using same walled-substrate with 40 μL suspension and drying under room condition.

In addition to the weight, thickness and stress characterization, cryoSEM images of sample GCC:clay-50:50 were taken to further explore the microstructure formation responsible for the stress peak during drying. Samples for this test were prepared in a similar way as those used for stress measurement, but the samples were drying under ambient conditions on smaller substrates. Therefore the drying times are not directly comparable to those in Figure 5.4. Figure 5.5a shows a cryoSEM cross-section of a coating frozen after 3 minutes of drying. This image clearly shows frozen water throughout the coating, indicating that the coating is saturated. The GCC, clay and latex particles are discernible based on the size and shape of the particles using this

imaging method since the latex is not deformed. An image taken of a coating frozen after a slightly longer drying time (5.5 min, Figure 5.5b) shows less water; however, quantification of the water present is challenging due to sublimation that is carried out before imaging to create contrast during imaging. Interestingly, the latex particle shape is still roughly symmetrical with little particle-particle contact and deformation. After a somewhat longer drying time (7 min, Figure 5.5c), the latex particles are less distinct and show some features of deformation. Likewise, after the longest time (9 min, Figure 5.5d), the particles are almost completely deformed. These images are consistent with the general progression of microstructure development postulated in the description of the stress measurement results.

According to the microstructure changes observed via the cryoSEM images, capillary forces and particle deformation are dominating at the early and later stages of stress development respectively. And it is the time lag between the two dominating forces, or in other words, the delay of the particle deformation that results in the formation of this unique shape of the stress development curve. It should be noted that such delay is likely also occurring in the coatings explored in Chapter 4, but it is only apparent when the particle size is small and capillary stress is large. For this delay to be present, there must be relatively low amount of latex such that the final microstructure is porous. In this case, the large GCC and clay particles established a hard particulate network first on drying and menisci form based on this network, causing the stress rise, and then retreat into the network, causing the stress to drop. Latex deformation begins when the menisci begin to act directly on those particles locally or on the densely packed adjacent rigid particles which then press the latex particles gathered in the pore space between the large GCC and clay particles.

The shrinkage and particle rearrangement resulting from the packing of the complexed shaped particles may influence this delay. Past research has reported no second-time stress increase in the drying stress study of spherical particulate coatings containing both rigid and soft particles [145] but similar stress peak has been observed in the stress tests of irregular particulate coatings with both rigid and soft particles [89, 143]. Here in this coating system, the geometry constraints come from both the irregular-shaped GCC particles and the plate-shaped clay particles.

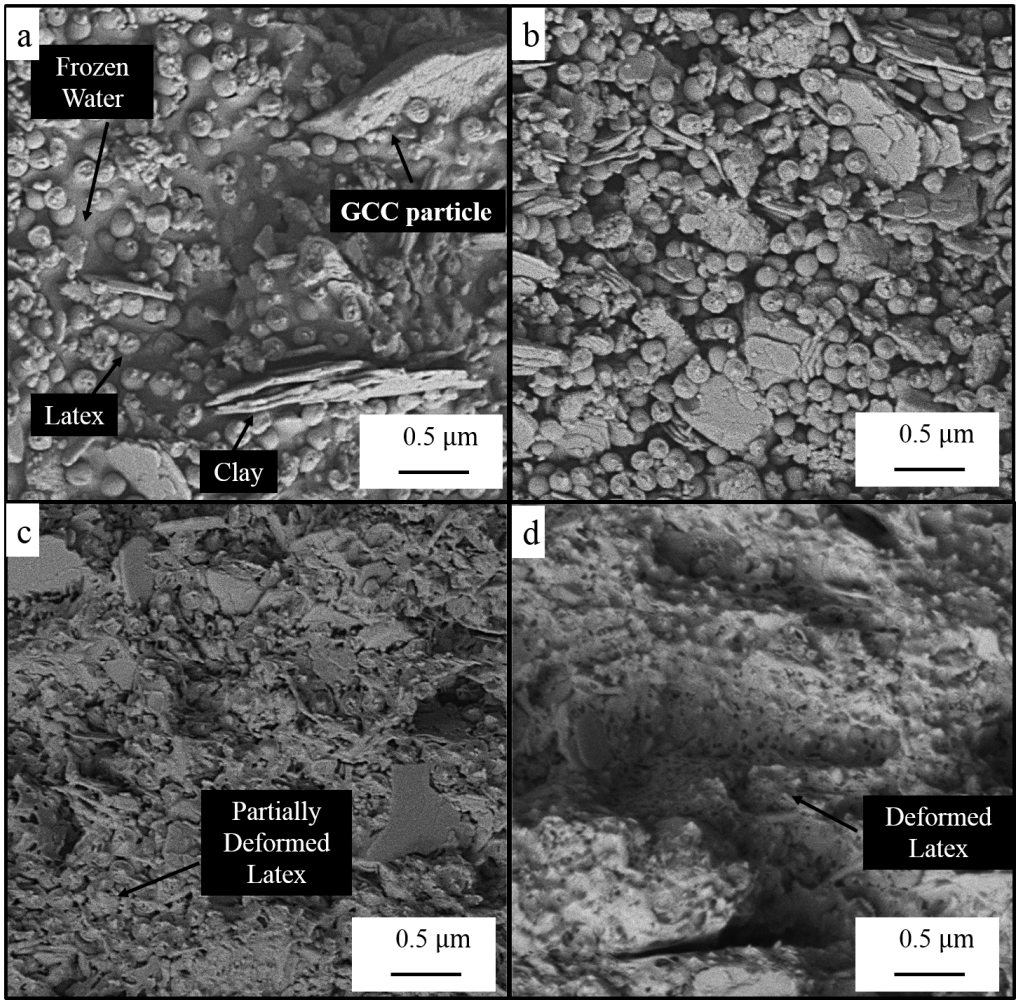

Figure 5.5: CryoSEM cross-sectional micrographs of coating GCC:clay-50:50 on 5 mm × 7 mm silicon substrates dried for (a) 3 minute, (b) 5.5 minute, (c) 7.5 minute and (d) 9 minute. Drying is conducted using 5 mm × 7 mm silicon chip under room condition.

Table 5.4: Summary of shrinkage results for GCC-based dispersions with different GCC-clay ratios.

Sample	Shrink rate (μm/min)	Shrink time (min)
GCC:clay-100:0	11.05 ± 2.75	11.90 ± 0.86
GCC:clay-75:25	13.52 ± 1.22	11.05 ± 0.83
GCC:clay-50:50	16.58 ± 1.95	11.05 ± 0.35
GCC:clay-25:75	20.54 ± 2.10	11.05 ± 1.45

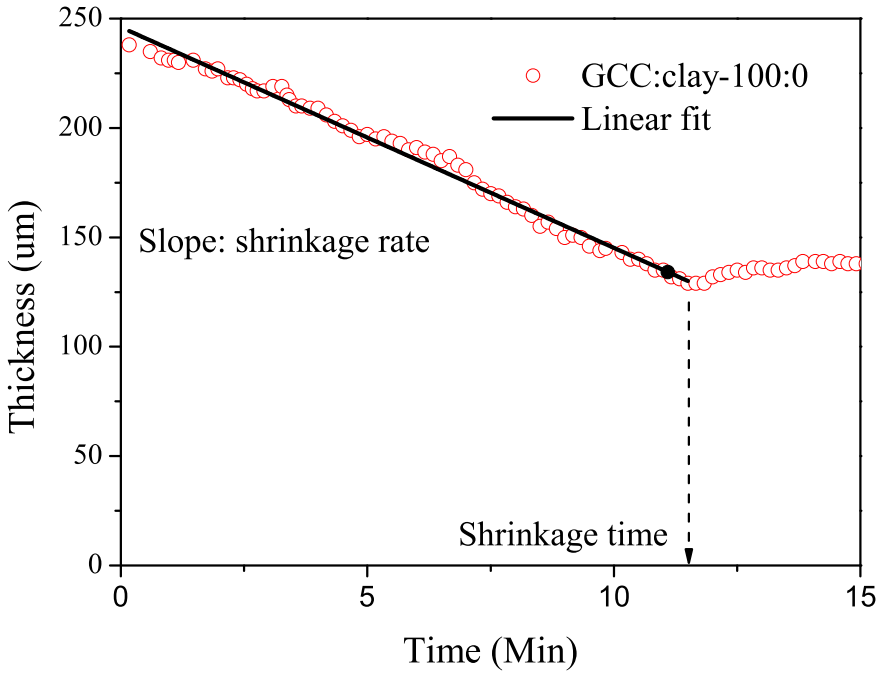

Figure 5.6: Shrinkage curve of GCC:clay-100:0 coating, with the shrink rate (slope of the linear fit line) and shrink time labelled.

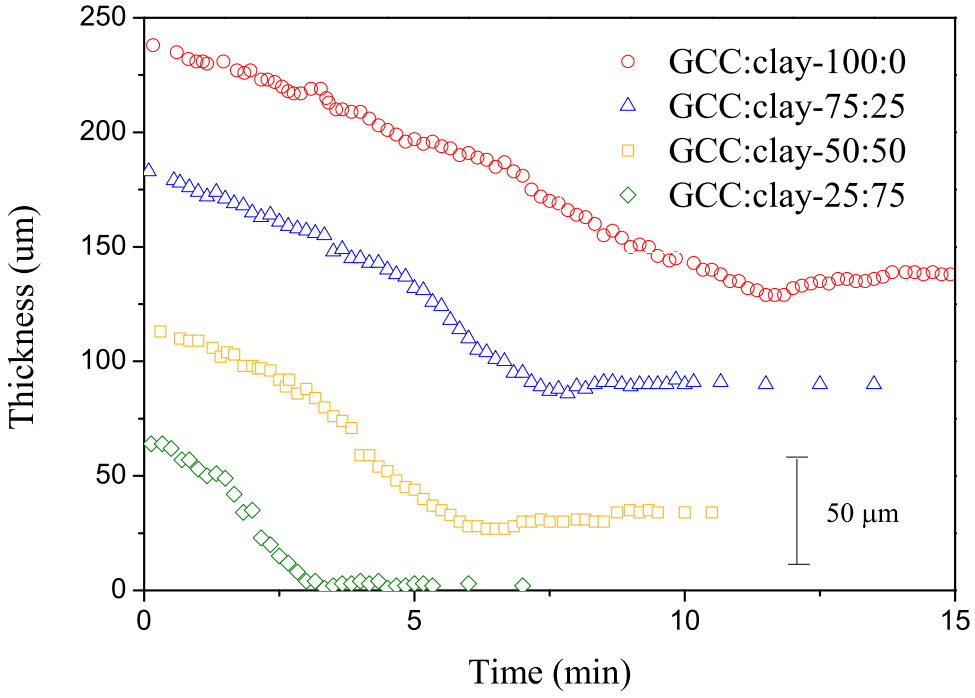

Figure 5.7: The shrinkage curves of four GCC-based coatings with different GCC-clay ratio are plotted together. All four curves are started at the same initial thickness but super-positioned this way to better present the data. The shrink rate (slope of the curve) of sample GCC:clay-100:0, GCC:clay-75:25, GCC:clay-50:50 and GCC:clay-25:75 are 10 μm/min, 13 μm/min, 17 μm/min and 22 μm/min, respectively.

The thickness change of the coating is in response to the drying as well as the shrinkage of the particulate network induced by capillary and particle deformation. Figure 5.6 shows one plot of coating height or thickness as a function of time, as measured with a laser profilometer. The absolute value of coating thickness is determined based on the difference between the vertical position of the substrate and the coating surface provided by the profilometer data. Early in drying, the free surface drops at a rate that depends on evaporation alone. At the later drying stage, the shrinkage is related to particle rearrangement and collapsing large empty space in between particles. Table 5.4 shows the shrinkage results of the GCC-based coatings with four different GCC-clay ratio measured under room condition using laser profilometer. Four example shrinkage curves of each sample are given in Figure 5.7. As the shrinkage data suggests, with increasing level of clay content, samples exhibit faster shrinkage rate, but less shrink time. With more content of the plate-like clay, the coating network has more complex particle shapes whose geometry constraints hinder the rotation and rearrangement of the particles. Collapsing the gaps between the pigments, as the dominating densification action for the high-clay-content coatings, gives higher shrink rate since the excess of clay particles helps the network to be 'locked' at a more porous position at the beginning of the drying. However, with less ability of particle rearrangement and orientation, coatings with high clay level end the shrinkage earlier. Therefore, in the later stage of drying, when the coatings acquire more solid-like nature, the high-clay-content coatings possibly experience less constrained shrinkage, resulting in less cracking.

The thickness measured using the laser during the coating shrinkage test is not exactly the 'true value' but the 'relative value', which are valid only for the shrinkage rate and time analysis. Due to the sensitivity of the laser profilometer, the setting of the substrate (i.e. the air gap between the substrate and the table) can easily cause the profile shift, which induces error to the accurate thickness measurement. According to the thickness measured using the digimatic indicator, coatings drying under the room condition show similar final thickness to the ones drying under the controlled condition (as listed in Table 5.3.2). Therefore, the total shrinkages of the coatings between formulations are comparable.

5.3.3 Discussion

Characterizing the GCC-clay coatings drying and cracking behavior via microstructure, stress and thickness changes, a better understanding of the role of clay particle is gained. Due to the addition of the plate-like clay particles to the GCC-latex coatings, the particulate network is less densely packed with larger pore spaces in between particles. The larger pore spaces lead to lower capillary-induced stress and more delay in latex deformation-induced stress since the rigid particles can't press the latex particles sufficiently under capillary pressure when packed loosely, therefore, lower stress values were observed in coatings with high clay level. With decreasing stress development, the coatings have smaller driving force for crack formation. However, the differences in stress are not significant. The fracture toughness of the coatings, which is reflected by the CCT, is enhanced with the higher level of clay addition. Also, the difficulty in particle rearrangement at the later stage of the drying for coatings containing more plate-like clay particles suppresses the shrinkage and may contribute to the less crack formation.

5.4 Summary

This study demonstrates the effect of adding clay particles to the GCC-based coatings on stress development, microstructure changed and cracking performance. With decreasing GCC-clay blending ratio, more platy-shaped clay particles are added into the irregular-shaped GCC particulate network, so coatings have better cracking resistance under slightly decreased stress development. The increased amount of clay content with enhanced particle shape complexity intensifies the geometry constraints and disrupts the particle rearrangement. The hindered shrinkage of the particulate network explains the stress peak development and less cracking formation. However, blending clay particles to particulate coatings does not always leads to cracking performance improvement. More severe cracks are observed when adding clay into silica-based coatings. The shape and material properties of the original pigments in the particulate coatings may alter the effect of clay addition.

5.5 Acknowledgement

The authors would like to gratefully thank the support from the WestRock Company and the Coating Process Fundamentals Program. Acknowledgements also go to Gary Fugitt, Chris Frethem, and Wieslaw Suszynski for their contributions to this project. Some of this work was carried out in the Characterization Facility, University of Minnesota. The Hitachi SU8320 cryoSEM and cryo-specimen preparation system were provided by NSF MRI DMR-1229263.

Chapter 6

Effect of Clay Addition to Spherical-shaped Particulate Coatings with Different Particle Size Distribution

Abstract—Inspired by the previous study introduced in Chapter 5, more work is done to continue explore the impacts of clay addition on coating drying and cracking behavior. Adding clay pigments to the coatings containing irregular-shaped ground calcium carbonate (GCC) particles and latex binders, as discussed in chapter 5, improves the coating cracking resistance. In this chapter, the effect clay pigments is studied using spherical-shaped silica coating systems. Two types of the silica coating systems, preparing from mono-dispersed and bimodal-dispersed silica particles, are studied using similar approaches as the previous work, including stress measurement, cracking characterization, shrinkage test and SEM imaging. With decreasing pigment-clay blending ratio, the increased level of clay content influences the drying behavior of silica-based coatings and reduces the cracking resistance.

6.1 Background and Motivation

Kaolin clay particle, as a popular component in many coating formulations, is proven to alter the coating properties and provide varied functions. Many research has investigated the roles of the characteristics of the clay particles, such as the particle size, shape and surface chemistry, on coating performance. However, the influence of the properties of the pigments that blend with the clay particles in coating formulation is not well-known.

Kaolin clay engineered with tailored particle size, shape, and distribution and surface chemistry is considered to be the essential component that gives paper coatings controlled optical and physical properties. [156, 13, 157] Much research has been done to investigate the role of kaolin clay in determining the coating structure and optical properties. The physical properties like the pigments particle shape and size are found to have a larger impact on the gloss and roughness of coated sheet than the chemical properties. [32] As demonstrated by the work of Morris *et al.*[160], coatings with highly plate-like shaped, delaminated kaolin clay particles generate smoother film surfaces with higher gloss than undelaminated kaolins. The importance of using finer pigments to promote higher gloss and lower roughness is supported by many researchers. [157, 32, 161, 166] The impact of kaolin clay pigments on the opacity and printability of paper coatings is closely related to coatings porous structure. More light scattering interfaces are available when coating structure contains a larger number of voids; and the difference in the reflective indices (R.I.) of kaolinite (R.I.= 1.56) and air-filled voids (R.I.= 1) leads to large reflection coefficient, [154, 167] and thus the light scattering of the coated paper is promoted, which results in good brightness and opacity. The printability is also closely related to the porous structure, which controls the capillarity-based ink absorption and compressibility. [154, 168]

The impact of the kaolin clay on the physical properties of paper coatings, such as the permeability, flexibility, stiffness and strength, has been investigated in coating systems with different blending pigments and binders. In studies of coating systems that blend kaolin clay with GCC pigments and binders, several researchers [158, 159, 162, 163] have found that increasing the clay content enhances in-plane tensile and printing strength of coatings, as well as the bending stiffness, and this reinforcement is increased with clay

aspect ratio. By studying the coating microstructure, clay particles were found to be oriented parallel to the coating surface with increased clay content, which leads to more gloss and less porosity. [156, 164] The clay content in paper coatings is usually higher than the critical pigment volume concentration (CPVC); therefore an increase in binder level can reduce voids and lead to higher flexibility and lower permeability. [76, 165] However, for barrier coatings, fine clay is used as a filler and added into a polymer matrix at a value that is typically well below the CPVC. In this case, higher clay content increases the length of the diffusion path and enhances the barrier properties. [76, 77, 173]

The essential role of the shape of kaolin clay particles to the properties of paper coatings, which are usually prepared from GCC pigments, is well-recognized and studied; however, little research has investigated the impact of the characteristics of other particles (co-blending pigment) present with the clay, such as the shape and particle size distribution. In this study, the effect of kaolin addition is investigated by blending different level of clay particles with coatings formulated with spherical silica particles of altered particle size distribution and latex binder. The results can also be compared with the previous work (introduced in Chapter 5) of clay addition to irregular-shaped GCC coatings to reveal the role of co-blending pigment shape in drying and cracking behavior. Similar approaches were used in this study to explore the coating stress development, cracking and microstructure formation during drying.

6.2 Materials and Methods

6.2.1 Suspension Systems

The coating systems investigated in this study are very similar to the GCC-clay system studied in Chapter 5. As discussed in the previous chapter, the increasing clay content evidently influences the drying behavior of the GCC-based coatings. The complexity of the geometry constraint of the particles clearly plays an important role. To further clarify the impact of the plate-like clay particle from the irregular-shaped GCC particles, two silica-based coating systems were studied. The formulations of the silica-based coating samples are given in Table 6.1, the GCC particles are replaced with one or two types of silica particles. One silica coating system, denoted as Mo-silica system,

is prepared from mono-dispersed silica particles with size of 750 nm; the other system, denoted as Bi-silica system, contains the bimodal-dispersed silica particles which is the mixture of 300-nm and 750-nm mono-dispersed silica particles with ratio of 1:2. The Bi-silica coatings are formulated to create wider particle distribution of the co-blending pigments. The latex binder (Acronal-S504, BASF, approximate particle diameter of 0.2 μm, glass transition temperature, $T_g, = 4°C$) and the clay particle (Kaofine 90, Thiele, ratio of particle diameter to thickness is between 5 to 10, mean particle diameter of $\sim$ 0.2 μm [169]) are the same type used in the GCC system. All coating dispersions are kinetically stable [170] (pH of silica-based coatings are 9-9.5), and samples were sonicated for 10 minutes prior to deposition.

Table 6.1: Solid compositions of nine coating dispersions given in volume percent.

Sample	Silica (750 nm)	Silica (300 nm)	Clay	Latex	Total Solid
Mo-silica:clay-100:0	29.19			15.07	44.26
Mo-silica:clay-75:25	21.89		7.43	15.15	44.47
Mo-silica:clay-50:50	14.75		14.86	15.13	44.56
Mo-silica:clay-25:75	7.45		21.82	15.07	44.34
Bi-silica:clay-100:0	19.46	9.73		15.07	44.26
Bi-silica:clay-75:25	14.60	7.30	7.43	15.15	44.47
Bi-silica:clay-50:50	9.71	4.86	14.86	15.13	44.56
Bi-silica:clay-25:75	4.97	2.48	21.82	15.07	44.34
Mo-silica:clay-0:100 Bi-silica:clay-0:100			29.19	15.07	44.26

6.2.2 Drying Stress Measurement

The dynamic stress development of the coating was characterized using a beam deflection method [2, 146] with a polydimethyl siloxane (PDMS) walled cantilever [103]. The measurement takes place in a drying chamber with controlled temperature and relative humidity (RH) using nitrogen gas. Uniform drying with suppressed drying front movement was observed during the test using walled cantilevers. [103] The deflection of the substrate free end in response to the stress developed in the coating layer is measured using laser and detector.

In a typical experiment, 40 μL of liquid suspension is applied onto the walled cantilever substrate (5 mm $\times$ 45 mm coating area) which is plasma cleaned (Harrick Plasma

Inc., Ithaca, NY) for two minutes before use. All stress measurements were conducted at 23 °C ± 1°C and RH of 6 % ± 2% controlled by nitrogen flow. For each sample, 6-8 repeat runs were conducted. Representative stress development curves are reported, as well as the final and peak stress values with an error based on a 95% confidence interval.

6.2.3 Microstructure Characterization

Scanning electron microscopy (SEM) was used to characterize coating microstructure after the drying. Coatings were prepared on 5 mm × 7 mm silicon substrates following a similar procedure as that used to prepare coated cantilevers for stress measurement; however, the coatings here were dried at room condition (23 °C ± 1°C and RH of 40 % ± 5%). Also, for samples prepared for cross-sectional imaging, the substrate was scored at the back prior to coating deposition in order to achieve neat fracture surface. Approximately 10 nm of platinum was sputtered onto the coating surfaces to reduce charging during imaging. The samples were imaged using secondary electron mode a Hitachi S-4700 or Hitachi SU-8230 (Hitachi, Pleasanton, CA) field emission scanning electron microscope (FESEM).

6.2.4 Critical Cracking Thickness (CCT) Measurement

Cracking behavior of two silica based coatings with different levels of clay were characterized with the same approach used for GCC-based coatings. Coatings were deposited onto 5 mm × 45 mm walled silicon substrate with varied thickness and dried at room condition (23 °C ± 1°C and RH of 40 % ± 5%). The thickness was regulated by the amount of coating suspension deposited onto the substrate and measured after drying completes. The thickness was recorded as the critical cracking thickness when cracking was first observed in the sequence of samples with increasing amount of suspension deposition. The crack is observed by vision without microscopy. Due to the liquid pinning of the substrate wall, the edge of the coating is slightly thicker the rest of the coating area. The coating is not considered as a cracked one if the only cracks found are at the edge and are less than eighth of the coating width.

6.2.5 *In-situ* Thickness Measurement

Laser profilometer (KEYENCE LJ-V7001) was used to image the coating cross section profile. As discussed in Chapter 3.3, the full cross section of the center of the coating is measured to get one center point measurement using H orientation. The thickness of the coating layer was recorded every 10 second for the first 15 minutes of drying process; and then recorded every 20 second until 3 minutes after the tested sample reached final thickness. Plotting the thickness change as a function of time, the slope of the linear fit of the data from initial thickness to minimum thickness is taken as the shrink rate, while the time of the thickness to first reach minimum value is considered to be the shrink time. All samples were tested using same 5 mm $\times$ 45 mm walled silicon substrate under room condition (23 °C $\pm$ 1°C and RH of 40 % $\pm$ 5%).

6.3 Results and Discussion

The purpose of choosing these two silica coating systems is to investigate the effect of plate-like clay particle addition in the spherical particulate coating systems, eliminating the geometry constraint of irregular-shaped ceramic particles (like GCC). Also, the reveals the impacts of the shape and particle size distribution of the co-blending pigment by comparing the results to the GCC-based coatings (introduced in Chapter 5). Similar to the GCC-based coatings, both Mo-silica system and Bi-silica system have samples with four silica-clay ratios and are studied via characterizing the cracking behavior, microstructure, stress development and shrinkage during drying.

6.3.1 Cracking and Microstructure of Silica-Based Coatings with Clay Addition

As shown in Figure 6.1 and Figure 6.2, the large-scale silica coatings were applied on the PET film (Polyethylene Terephthalate) using a blade coater with 50 mil gap and dried under room condition (23°C and 38% RH). As indicated by the cracking patterns, more cracks formed as the relative amount of clay increases (silica-clay ratio decreases). These results are contrary to the trend observed in the GCC-latex system. With the dried film thickness around 380 μm, the cracking patterns provide the rough estimate of

the coating CCT. The more accurate CCT values were obtained by drying the coatings using small walled substrate with suppressed lateral drying effect. The measured CCT values are listed in Table 6.2.

Table 6.2: CCT of two silica-based coating systems with different level of clay additions drying under room condition.

Silica:Clay Ratio	Mo-silica System CCT (μm)	Bi-silica System CCT (μm)
100:0	>650 ± 20	>600 ± 20
75:25	590 ± 20	590 ± 20
50:50	350 ± 20	374 ± 20
25:75	260 ± 20	310 ± 20
0:100	371 ± 20	371 ± 20

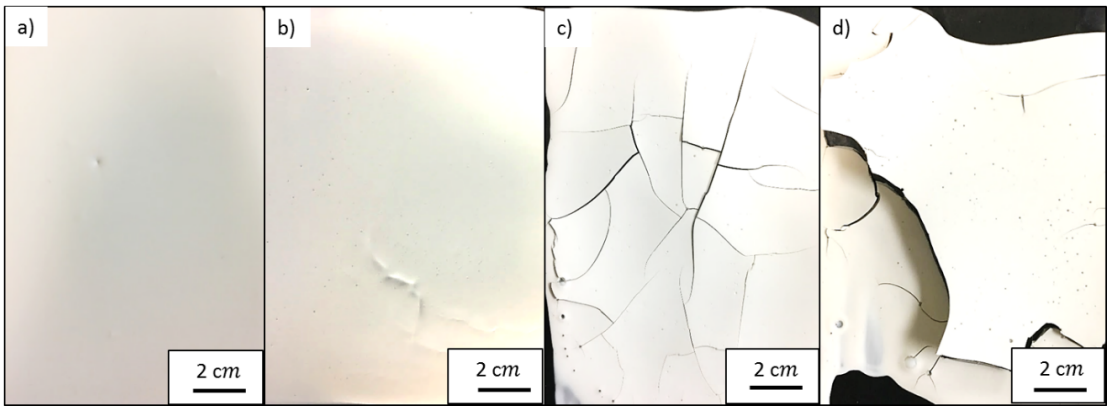

Figure 6.1: The cracking pattern observed on dried Mo-silica coatings with different silica-clay blending ratio. (a) Mo-silica:clay-100:0, (b) Mo-silica:clay-75:25, (c) Mo-silica:clay-50:50 and (d) Mo-silca:clay-25:75. Drying is conducted under room condition.

In both silica systems, the totally reversed trend of cracking resistance is observed comparing to GCC systems. However, according to the CCT values listed in Table 5.2 and Table 6.2, the silica-latex coatings have significant higher CCT than GCC-latex coatings in general. Even the GCC:clay-25:75 sample, the one with highest cracking resistance among the GCC-clay coating system (CCT of 220 ± 20 μm), has lower CCT than any of the silica-clay coatings and the clay-latex sample (pigment:clay ratio of 0:100). The CCT values of coatings containing single type of pigments, which are Mo-silica:clay-100:0, Bi-silica:clay-100:0, GCC:clay-100:0 and Mo-silica:clay-0:100, suggest that the cracking resistance is greatly attributed to the pigment's characteristic

microstructure and particle-particle bonds.

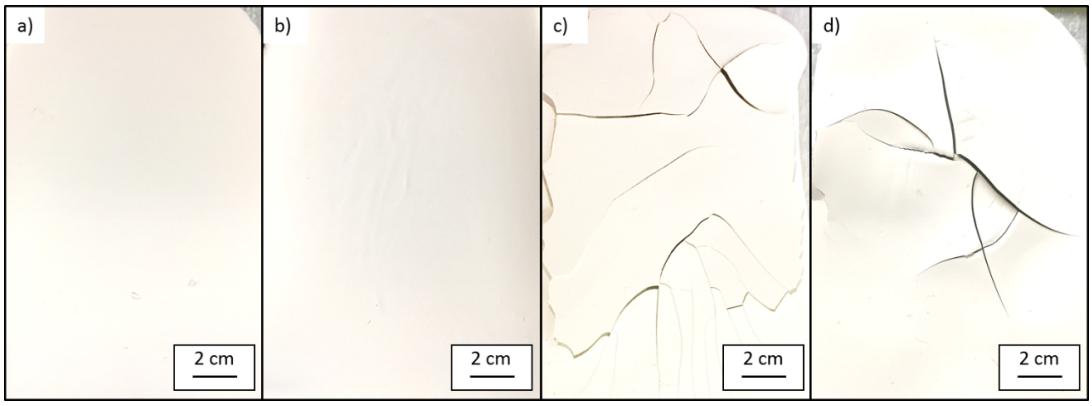

Figure 6.2: The cracking pattern observed on dried Bi-silica coatings with different silica-clay blending ratio. (a) Sample Bi-silica:clay-100:0, (b) Sample Bi-silica:clay-75:25, (c) Sample Bi-silica:clay-50:50 and (d) Sample Bi-silca:clay-25:75. Drying is conducted under room condition.

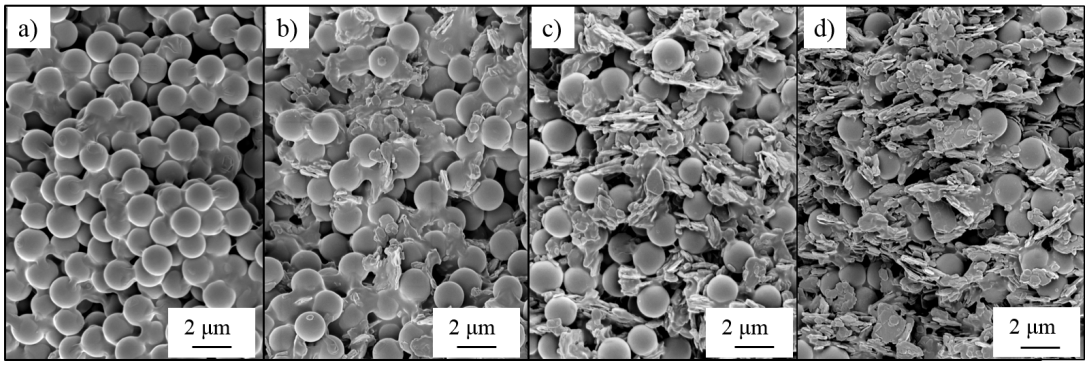

Figure 6.3: The cross-sectional SEM images of four Mo-silica samples with different silica-clay ratio. a) sample Mo-silica:clay-100:0; b) sample Mo-silica:clay-75:25; c) sample Mo-silica:clay-50:50; d) sample Mo-silica:clay-25:75. Drying is conducted under room condition.

As indicated by the CCT results, for the irregular-shaped GCC particulate coatings, decreasing GCC-clay ratio is actually replacing GCC particles with the clay particles which have better mechanical properties. Due to the similar irregular shape of the GCC and the clay pigments, particulate microstructure of coatings is not significantly impacted by varying blending ratio (as SEM images shown in Figure 5.2), thus the

cracking resistance is improved. And the reason that silica-based coatings have the reversed trend in CCT when changing pigment blending ratio is that the silica pigments already provide the coating with good cracking resistance (suggested by the CCT values of Mo-silica:clay-100:0 and Bi-silica:clay-100:0); adding clay particles actually disturbs the packing of the spherical particles and makes the particulate network less continuous (as shown in Figure 6.3 and 6.4), which sabotages the coating mechanical strength.

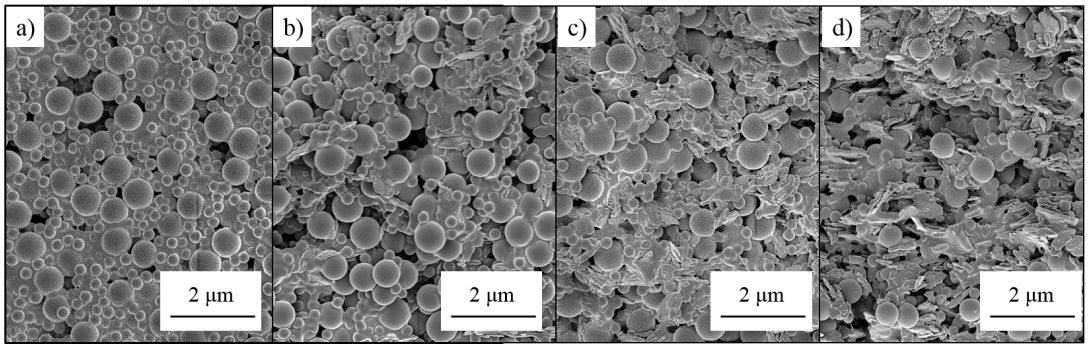

Figure 6.4: The cross-sectional SEM images of four Bi-silica samples with different silica-clay ratio. a) sample Bi-silica:clay-100:0; b) sample Bi-silica:clay-75:25; c) sample Bi-silica:clay-50:50; d) sample Bi-silica:clay-25:75. Drying is conducted under room condition.

In addition, the comparison between the cracking behavior of two silica-based coating systems shows the Bi-silica coatings, the coatings that contain silica particles with smaller averaged size and wider particle size distribution, have slightly better cracking resistance, which is in agreement with the previous work [89]. Comparing the cross-sectional SEM images of Mo-silica:clay-100:0 (Figure 6.3a) and Bi-silica:clay-100:0 (Figure 6.4a), with wider particle size distribution, the Bi-silica coating forms a more compacted microstructure and more particle-particle contact. With decreased silica:clay ratio, more open spaces are observed in the microstructures of two silica-based coating systems, but still, the Bi-silica coatings have a more densely packed microstructure comparing to single-silica-based coatings with the same blending ratio.

6.3.2 Stress Development and Microstructure Evolution During Drying

To better understand the cracking behavior of the silica-based coatings, in addition to the CCT values, the *in-situ* stress development was measured. The results for the stress measurement of Mo-silica coatings and Bi-silica coatings with four different silica-clay ratios are listed in Table 6.3 and Table 6.4, respectively. And the representative stress development curves of these two coating systems are shown in Figure 6.5 and Figure 6.6.

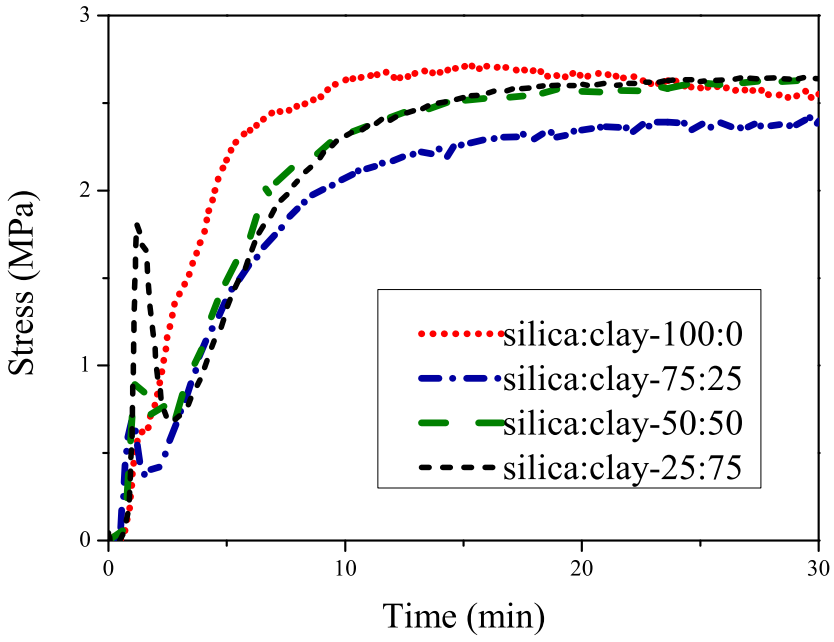

Figure 6.5: Stress development curves of Mo-silica coatings with different silica-clay blending ratio. The measurements were conducted under controlled drying condition (23 °C ± 1°C and RH of 6%± 2%) using nitrogen flow.

As indicated by the final stress values, no strong correlation is found between the magnitude of coatings final stress and clay addition concentration. However, illustrated by both the average stress peak values in Table 6.3 and Table 6.4, and stress peak magnitudes in Figure 6.5 and 6.6, the stress peak formation is stimulated by the increased

level of clay content. For sample Mo-silica:clay-100:0, no peak formation was observed; while sample Bi-silica:clay-100:0 only shows a peak with very small magnitude. This phenomenon may be related to a hypothesis brought up in the previous chapter: the peak formation due to the hindered shrinkage results from the complex particle shapes which comes from both the irregular shape of the co-blending pigment (i.e. the GCC pigments in the previous work) and the plate-like clay particles. Now, without the geometry constraint, latex deformation happens more efficiently under compacted spherical particle network with no delay, thus no stress peak or little stress peak is found for the stress development of silica:clay-100:0 samples. And with increasing amount of clay addition, the peak stress magnitude increases.

Table 6.3: Test results of coatings prepared from five Mo-silica-latex dispersions with different level of clay addition.

Sample	Stress (MPa)		Final thickness
	Peak	Final	(μm)
Mo-silica:clay-100:0	0	2.83 ± 0.18	90.00 ± 3.65
Mo-silica:clay-75:25	0.75 ± 0.16	3.34 ± 0.13	89.42 ± 4.40
Mo-silica:clay-50:50	1.04 ± 0.22	2.46 ± 0.32	93.35 ± 9.22
Mo-silica:clay-25:75	1.55 ± 0.16	2.61 ± 0.02	82.66 ± 2.98
Mo-silica:clay-0:100	2.30 ± 0.39	1.53 ± 0.17	86.86 ± 5.69

Table 6.4: Test results of coatings prepared from five Bi-silica-latex dispersions with different level of clay addition.

Sample	Stress (MPa)		Final thickness
	Peak	Final	(μm)
Bi-silica:clay-100:0	0	2.05 ± 0.19	86.19 ± 3.84
Bi-silica:clay-75:25	0.86 ± 0.14	1.47 ± 0.15	89.48 ± 3.55
Bi-silica:clay-50:50	1.22 ± 0.17	1.39 ± 0.10	99.77 ± 5.43
Bi-silica:clay-25:75	1.84 ± 0.14	1.68 ± 0.18	88.50 ± 4.60
Bi-silica:clay-0:100	2.30 ± 0.39	1.53 ± 0.17	86.86 ± 5.69

Comparing the stress peak magnitude of both silica-based coating systems, although the difference is not significant, the Bi-silica coatings always develop higher stress peak than the Mo-silica coatings with same silica:clay ratio. Capillary force, as the major contributing factor of the stress development in early drying stage, is enhanced in the

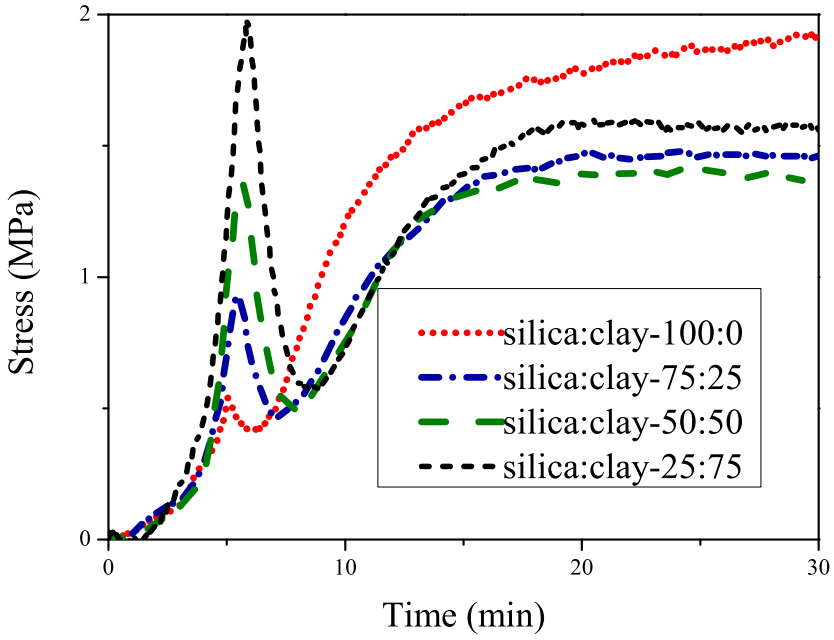

Figure 6.6: Stress development curves of Bi-silica coatings with different silica-clay blending ratio. The measurements were conducted under controlled drying condition (23 °C ± 1°C and RH of 6%± 2%) using nitrogen flow.

drying of Bi-silica coatings due to the smaller pore size and more compacted microstructure. However, the lower magnitude of the final stress in Bi-silica coatings is not fully understood. Since cracking is observed at the end of the drying stage, the coatings final stress magnitude is possibly more directly related to the cracking behavior rather than the stress peak values. The comparable final stress development measured in silica coatings with different silica:clay ratio cannot explain the cracking behavior, thus the shrinkage tests were conducted.

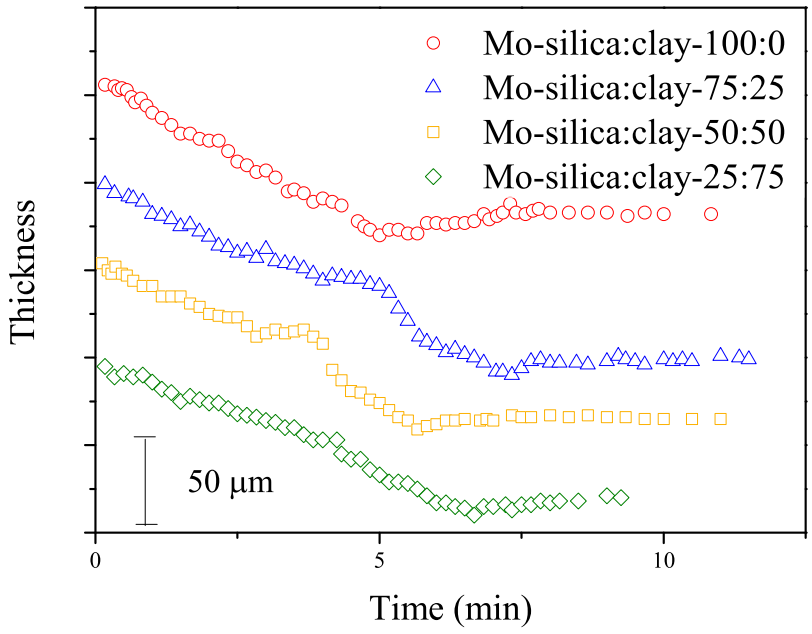

Figure 6.7: The shrinkage curves of four Mo-silica coatings with different silica-clay ratio are plotted together. All four curves are started at the same initial thickness but superpositioned this way to better present the data. The shrink rate (slope of the curve) of Mo-silica:clay-100:0, Mo-silica:clay-75:25, Mo-silica:clay-50:50 and Mo-silica:clay-25:75 are 17.6 μm/min, 14.4 μm/min, 15.7 μm/min and 12.9 μm/min, respectively.

The shrinkage tests were conducted to reveal the structure formation of the silica-based coatings. The shrinkage curve, as shown in Figure 6.7, is analysed to determine coating shrink rate, shrink time and total shrinkage. Suggested by the data listed in Table 6.5 and 6.6, the addition of the clay content slows down the shrinkage rate of the

silica-latex coatings, but no considerable change observed when further increasing the clay level. With lower silica-clay ratio, a slight increase can be found in the coating shrink time, which is the opposite trend seen in GCC-latex coatings (Table 5.4). All these dissimilarities are due to the pigment particle shape changes from irregular to spherical. For the silica-latex coatings, the clay addition is the major source of the geometry constraint. In addition to collapsing the particulate network, the spherical silica particles can be rearranged to create more shrinkage. However, with more clay particles blended into the particulate system, it becomes harder to rearrange the particles and orientate the clay; therefore, the shrinkage rate decreases and longer shrinking time is needed.

Table 6.5: Summary of shrinkage results of Mo-silica coatings with different silica-clay ratios. The measurements were conducted under room condition (23 °C ± 1°C and RH of 40%± 5%).

Sample	Shrink rate (μm/min)	Shrink time (min)	Total shrinkage (μm)
Mo-silica:clay-100:0	19.24 ± 1.64	4.40 ± 0.50	86.67 ± 9.26
Mo-silica:clay-75:25	13.95 ± 1.99	4.38 ± 0.18	88.00 ± 13.06
Mo-silica:clay-50:50	12.33 ± 3.00	5.67 ± 0.31	97.25 ± 4.08
Mo-silica:clay-25:75	12.37 ± 1.40	7.55 ± 1.35	83.25 ± 9.54

Table 6.6: Summary of shrinkage results of Bi-silica coatings with different silica-clay ratios. The measurements were conducted under room condition (23 °C ± 1°C and RH of 40%± 5%).

Sample	Shrink rate (μm/min)	Shrink time (min)	Total shrinkage (μm)
Bi-silica:clay-100:0	10.34 ± 0.82	9.45 ± 0.16	91.00 ± 12.67
Bi-silica:clay-75:25	6.42 ± 1.33	8.78 ± 0.76	80.62 ± 14.89
Bi-silica:clay-50:50	6.20 ± 0.50	9.43 ± 2.23	81.55 ± 19.80
Bi-silica:clay-25:75	8.75 ± 1.06	10.25 ± 1.35	65.00 ± 14.41

Although the coatings shrinking ability deceases with the increasing clay content, the total amount of shrinkage of silica-latex coatings with four blending ratios is comparable, indicating the different cracking behavior should be more related to the mechanical properties changes. As the coatings microstructure shown (Figure 6.3 and Figure 6.4), the addition of plate-like clay particles to spherical silica particulate network greatly interrupts the particle packing. The wide particle size of clay create pore spaces with

a range of size. For the larger pores created due to the plate-like clay, the binding of the deformed latex is less sufficient, which leads to a less continuous particulate network. Therefore, the silica-latex coatings with higher level of clay content has weaker mechanical properties and lower cracking resistance.

6.4 Summary

The effect of plate-like clay addition is studied in two coating systems prepared from spherical silica particles of different particle size distribution. The changes found in drying behavior with different silica-clay blending ratio are due to the addition of the plate-like particles. This would be related to from the previous work studying the clay addition in GCC coatings (introduced in Chapter 5). The comparison of the drying process of different coating systems with same pigment:clay ratio helps to reveal the influence of the shape and particle size distribution of the co-blending pigments.

As a result of increasing clay content, both silica coating systems have relatively similar stress development. But the plate-like shaped clay particles do hinder the particle rearrangement during drying by intensifying the particles shape constraint, and cause stress peak formation. While in the irregular-shaped GCC particulate systems, increasing clay content reduces the total shrinkage and appears to result in higher fracture toughness; in the silica particulate systems, the shrinkage is not significantly influenced because of the good mobility of spherical silica particles, but the continuity of the particulate network is greatly destroyed and lead to weak mechanical properties, thus reduced cracking resistance.

6.5 Acknowledgement

The authors would like to gratefully thank the support from the WestRock Company and the Coating Process Fundamentals Program. Acknowledgements also go to Gary Fugitt, Chris Frethem, and Wieslaw Suszynski for their contributions to this project. Some of this work were carried out in the Characterization Facility, University of Minnesota. The Hitachi SU8320 cryoSEM and cryo-specimen preparation system were provided by NSF MRI DMR-1229263.

Chapter 7

Particulate Coatings of Nano-sized Pigments

Abstract—Drying is a critical step in coating manufacturing. For particulate coating systems, how particles come together during drying can lead to different structures and properties. Prior work has been focused on the drying behavior of coatings prepared with micron-sized particles. In this research, aqueous coating systems containing nano-sized silica and zinc oxide particles are studied. Coating drying behavior, including weight loss and stress development, was monitored under controlled conditions (temperature and humidity). The cracking behavior was studied by measuring the critical cracking thickness and imaging using digital microscopy. SEM techniques were used to characterize the particle morphology and microstructure changes.

7.1 Introduction

The coatings prepared with nanoparticles are used in a considerable number of applications. Nanoparticles are generally considered particles with at least one dimension smaller than 100 nm [174]. Industrial interest in nanoparticle coatings, which are considered as the top applications retaining the intrinsic properties of the nanoparticle material, is driven by the enormous potential of the nanoparticles market [3]. For example, the high refractive index of silica and titanium dioxide makes them commonly used in producing anti-reflective coatings [175], [12] and sunscreen lotions [176], [177]; the conductivity of silver particles gives good performance in printed electronic devices [18], [178], [179]; and zinc oxide is often found in coatings of optical devices like solar cells [33], [75] due to the great performance of absorbing UV light. But what makes nanoparticle coatings standout is the high surface area to volume ratio offered by the small size of the particle.

High surface area or interface area is attractive in various coating applications because it provides the coating with enhanced mechanical, optical, physical and chemical properties. For instance, in paints prepared with pigments and binders, using nano-sized particles allows the application of thinner coatings on finer structured objects and broadens the choice of color and transparency [180]. And more interfaces between the pigments and binders provide stronger binding interaction and toughen the material [181, 182, 183, 184]. The ability of creating a low surface energy coating surface with roughness of nano-scale makes the paint possible to gain self-cleaning properties [185], which can further increase stain resistance [186], corrosion prevention [187, 188] and anti-biofouling functions [189, 174].

However, the small size of the particles also poses some challenges to producing uniform and defect-free coatings. As the particle size decreases, the shorter distance between particles enhanced the particle interaction, resulting in a strong tendency to build up agglomerates[190]. Common solutions are adjusting the surface groups of the particles [174], [187], introducing polymeric dispersants, and altering the suspension pH value. For some coatings, the level of the binder addition is limited in order to establish properties such as conductivity, UV absorbance and high-porosity. In these cases, cracking is the major concern as a result of the weaker mechanical strength due to less

binding in between the particulate microstructure and stronger stress development. Being able to characterize the drying and cracking behavior of the nanoparticle coatings is critical to understanding the microstructure and stress development. Therefore, the desired structure and properties can be established by optimizing the coating formulation and processing condition design.

7.2 Materials and Methods

7.2.1 Suspension formulation

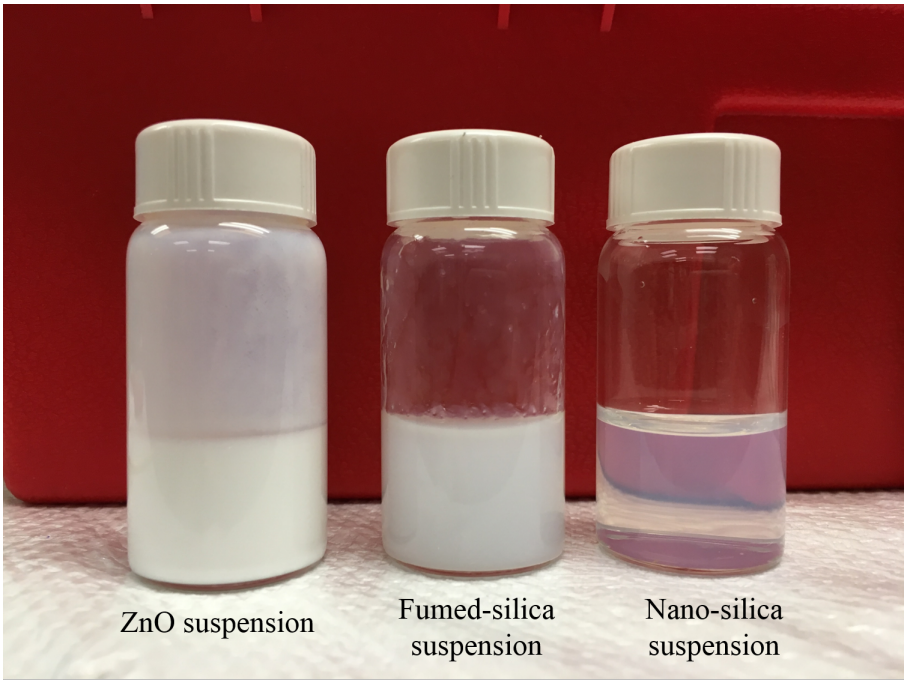

Figure 7.1: Experimental observations of the colloidal stability of three types of aqueous dispersions prepared from zinc oxide, fumed-silica and nano-silica particles.

In this work, the cracking and stress development of nanoparticulate coatings are investigated using suspensions of nano-zinc oxide particles, nano-silica particles and fumed-nanosized-silica particles with no binder addition. The approaches used for characterizing coatings of micro-sized particles (introduced in Chapter 4-6) are applied and evaluated, including beam deflection stress measurement, critical cracking thickness

(CCT) measurement, digital and scanning electron microscopy (SEM).

The nanoparticle coating systems investigated in this work were aqueous suspensions prepared from zinc oxide (US7100, US Research Nanomaterials, Inc.) with a size of 30-40 nm, nano-silica particles (AS-40, Ludox) with a size of 22 nm, and fumed-silica particles (CAB-O-SIL EH5, Cabot). The particles have no surface treatment. The suspensions were stabilized by electrostatic approach via adjusting pH [191], with no binder or additive added (pH of the zinc oxide coating is around 10, pH of nano-silica coating and fumed-silica coating are around 9). All suspensions were prepared to contain nanoparticles at a volume concentration of 2.13 %. Due to the different particle morphology, the three suspensions have different appearance as shown in Figure 7.1. All suspensions were sonicated for 10 minutes prior testing.

7.2.2 Stress Measurement

Beam deflection method was used to characterize the dynamic stress development of three nanoparticle coatings during drying. The working principle and experimental setup are introduced in detail in Chapter 3.2. The deflection of the substrate free end in response to the stress developed in the coating layer is measured using a laser and detector, and stress is calculated using the modified Corcoran Equation [2, 103]. The cantilever used in this study is on etched silicon substrate with 17 μmm-deep etched-in coating area, as shown in Figure 7.2. The substrate is made using photolithography method to produce wall with the smaller height.

Figure 7.2: Photograph of the cantilever using for beam deflection stress measurement. The cantilever is made from standard silicon substrate (dimension of 6 mm $\times$ 60 mm with thickness of 520 μm) with a coating area (5 mm $\times$ 45 mm) etched-in 17 μm in depth.

For each stress measurement test, 20 μL of liquid suspension is applied onto the

walled cantilever, which is plasma cleaned (Harrick Plasma Inc., Ithaca, NY) for two minutes before an experiment. All stress measurements were conducted at room condition at 23°C ± 1°C and RH of 15%± 2%.

7.2.3 Critical Cracking Thickness Measurement

The critical cracking thickness (CCT) values of these three coatings systems were measured. For zinc oxide suspension and nano-silica suspension, the tests were conducted using two different concentrations, 20 wt% and 2.13 vol%, respectively. The thickness was regulated by the amount of coating suspension deposited onto the substrate and measured after drying completes using digimatic indicator (C112TB, Mitutoyo). In this test, both the standard cantilever with PDMS wall and silicon substrate with etched-in coating area (cantilever substrate design discussed in detail in Section 3.1.4) were used to suppress lateral drying effect. The thickness was recorded as the critical cracking thickness when cracking was first observed in the sequence of samples with increasing amount of suspension deposition. Cracks were observed visually without a microscope. The coating is not considered as a cracked one if cracks are very tiny and only formed at the edge near the substrate wall due to the edge effect. (For example, bottom coating shown in Figure 7.3.)

7.2.4 Microstructure Characterization

Scanning electron microscopy (SEM) and digital microscopy were used to characterize coating microstructure and cracking after drying. For SEM sample, coatings were prepared on 5 mm × 7 mm silicon substrates following a similar procedure as that used to prepare coated cantilevers for stress measurement. Then the SEM samples were sputtered with approximately 10 nm of platinum onto the coating surfaces to reduce charging during imaging. The SEM samples were imaged using Hitachi SU-8230 (Hitachi, Pleasanton, CA) field emission scanning electron microscope (FESEM). And the appearance of the coating cracks was imaged using a digital microscope (Hirox) with the MX(G)-MARCOZVI lens.

7.3 Results

The CCT tests were first conducted using concentrated nano-silica suspension and zinc oxide suspension with 20 wt% under room condition (23°C ± 1°C and RH of 15%± 2%). The substrates used were PDMS walled substrate. The results and appearances of the two coatings are very distinct, as shown in Figure 7.3. As listed in Table 7.1, the CCT of concentrated zinc oxide coating is around 55 μm, which is very thick relative to its particle size. But for the concentrated nano-silica coating, the CCT is below 10 μm. The CCT of concentrated nano-silica was not accurately measured because of the limitation of the substrate. As shown in Figure 7.4, all coatings tested using the substrate with PDMS wall demonstrate cracks with considerable length. However, the amount of the deposited suspension could not be further reduced to create coating thinner than 10 μm with the whole coating area covered.

Table 7.1: Summary of CCT results of coatings prepared with different nanoparticles tested using different substrates.

	conc. zinc oxide	conc. nano-silica	zinc oxide	nano-silica	fumed-silica
CCT	55 μm	<10 μm	>35 μm	<2 μm	<5 μm
Substrate	PDMS wall	PDMS wall	Etched	Etched	Etched

The CCT tests are improved by reducing the wall height using etched substrates. Using the PDMS wall with the height much larger than the coating wet thickness, the liquid meniscus formed at the wall results to non-uniformity in coating drying and final thickness (as shown in Figure 7.4). The etched substrates were made to match the wall height to the coating wet thickness, which reduce the edge effect (as shown in Figure 7.5). The CCT of three dilutes suspensions are listed in Table 7.1. Still using this method, no accurate CCT values were obtained. The CCT of diluted nano-silica coatings and fumed-silica coatings were less than 2 μm and less than 5 μm, respectively. Coatings with thinner thickness could not be applied due to the incomplete coverage of the coating area. The CCT is reported as larger than 35 μm for diluted zinc oxide coating. No higher thickness is obtained because the excess amount of suspension leads to liquid overflow from the etched-in coating area.

As shown in Figure 7.5, the cracking pattern of the coating prepared from fumed silica particles is different to that observed in the other two coatings. When observed

only by eye, it is difficult to determine whether the fumed-silica coating layer is cracked or not. Using the digital microscopy, the coating is magnified with cracking clear presented. Top view pictures of cracked nano-silica coating and fumed-silica coating taken using a digital microscope are given in Figure 7.6 and 7.7, respectively. The cracking patterns of two coatings are different. Parallel cracks were seen in nano-silica coating (Figure 7.6), which indicate the cracks release stress preferentially in the parallel direction with no interaction. On the other hand, the "mud cracking" pattern with smaller cracking space observed in the fumed-silica coating (Figure 7.7)suggests the coating layer cracks under biaxial stress and possibly has lower fracture toughness [101].

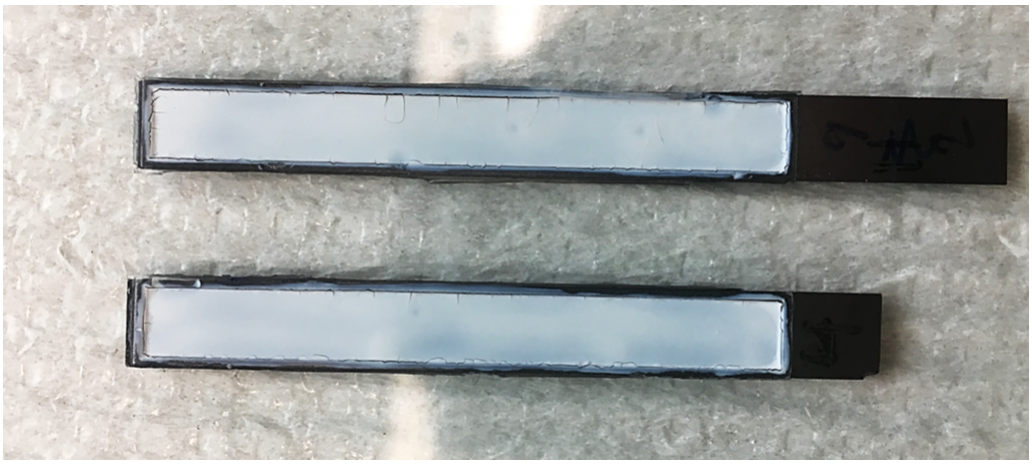

Figure 7.3: Photograph of concentrated zinc oxide coatings conducting CCT tests using standard walled substrate. Both coatings exhibit tiny cracks close to the PDMS wall, the top samples which the length of the cracks reach one third the coating width is considered cracked, while the bottom sample is considered as not cracking.

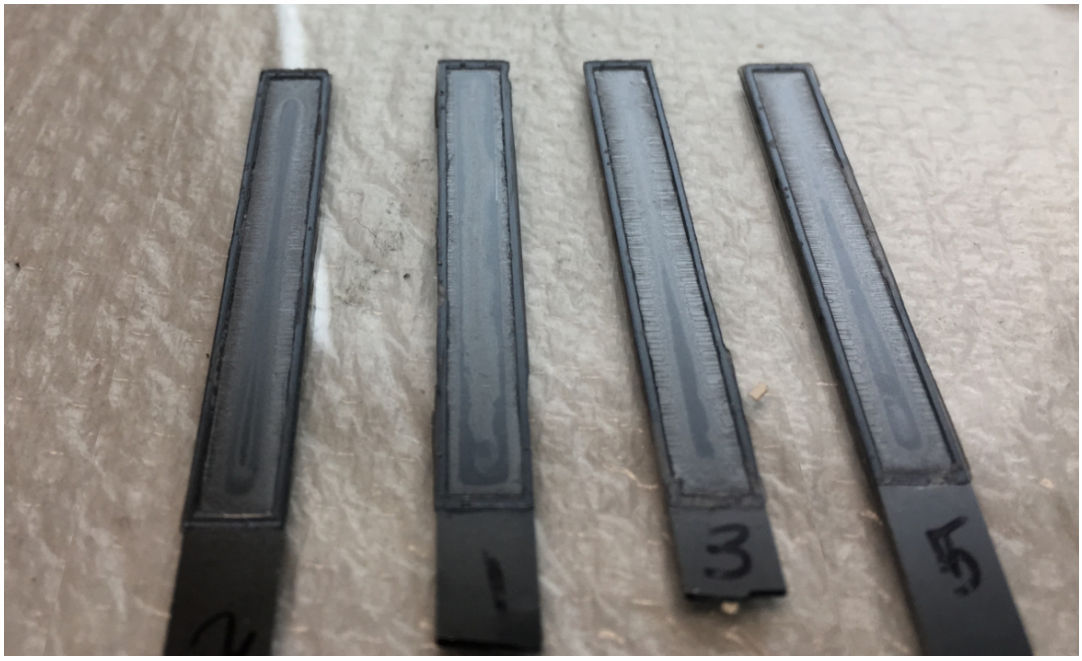

Figure 7.4: Photograph of concentrated nano-silica coatings testing CCT using standard walled substrate. All coatings exhibit cracks close to the PDMS wall with different length. Thicker the coating, longer the cracking. All four coatings shown are considered cracked according to the crack scale.

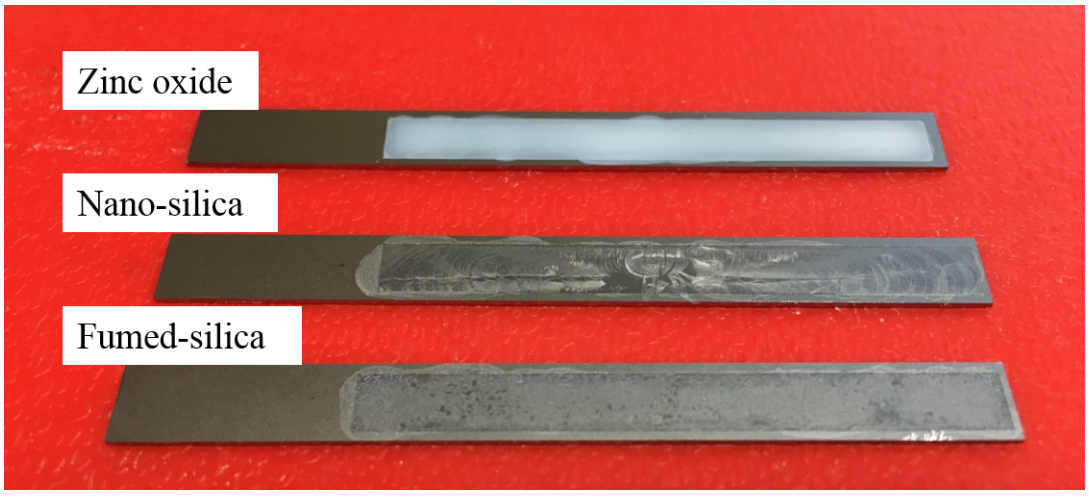

Figure 7.5: Photograph of three diluted coating systems testing CCT using etched substrate. No cracking is observed in the zinc oxide coatings. Both diluted silica-based coatings are considered cracked according to the crack scale.

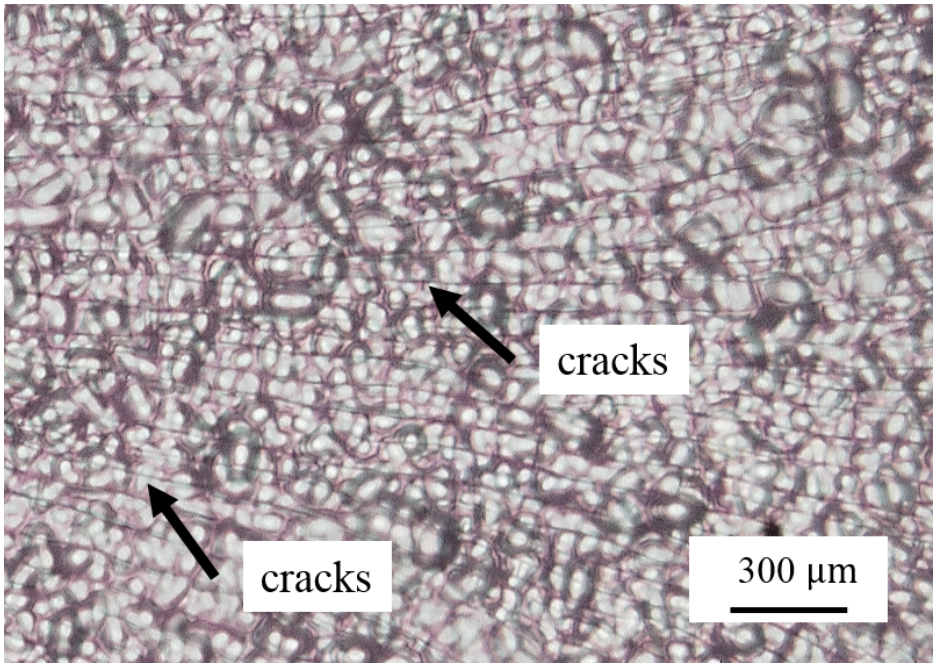

Figure 7.6: Topview digital microscopy image of cracked coating prepared from nano-silica particles with low concentration. Note: the small circles observed in the images are the patterns on the dull side of the silicon substrate.

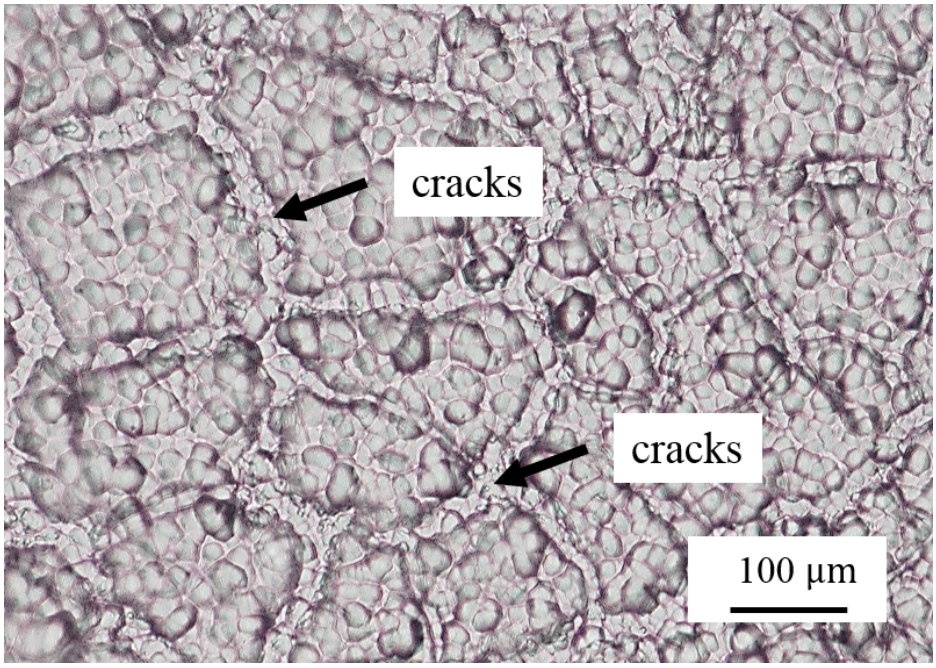

Figure 7.7: Topview digital microscopy image of cracked coating prepared from fumed-silica particles with low concentration. Note: the small circles observed in the images are the patterns on the dull side of the silicon substrate.

The microstructures of three diluted coatings were imaged using SEM technique. Figure 7.8, 7.9 and 7.10 show the morphologies of the nano-sized pigments and the particulate microstructures of the coatings of nano-silica, zinc oxide and fumed-silica, respectively.

The stress measurements were conducted using diluted suspensions of zinc oxide, nano-silica and fumed-silica. The tests were done using 20 μL of suspension drying under room condition (23°C $\pm$ 1°C and RH of 15%$\pm$ 2%) using etched cantilever substrates. However, the cracking was too severe in nano-silica coatings using that much amount of suspension, as shown in Figure 7.11. The shredded coating pieces delaminated from the silicon substrate leaving no detectable deflection for analysis. Cracking was also observed during the drying of fumed-silica coatings during stress measurement. But as the final fumed-silica coating shown in Figure 7.5, the coating layer is still in one piece and adhered to the substrate, thus the deflection can still be measured and analyzed. The results of averaged maximum stress and the final thickness of zinc oxide coating and fumed-silica coating are summarized in Table 7.2. Results are averaged over four trials.

Table 7.2: Summary of averaged stress peak values and final thickness of nanoparticle coatings.

	zinc oxide	fumed-silica *
Average Peak stress (MPa)	0.87 $\pm$0.10	0.19 $\pm$0.06
Thickness (μm)	7 $\pm$1	28 $\pm$2

* Fumed-silica samples cracked.

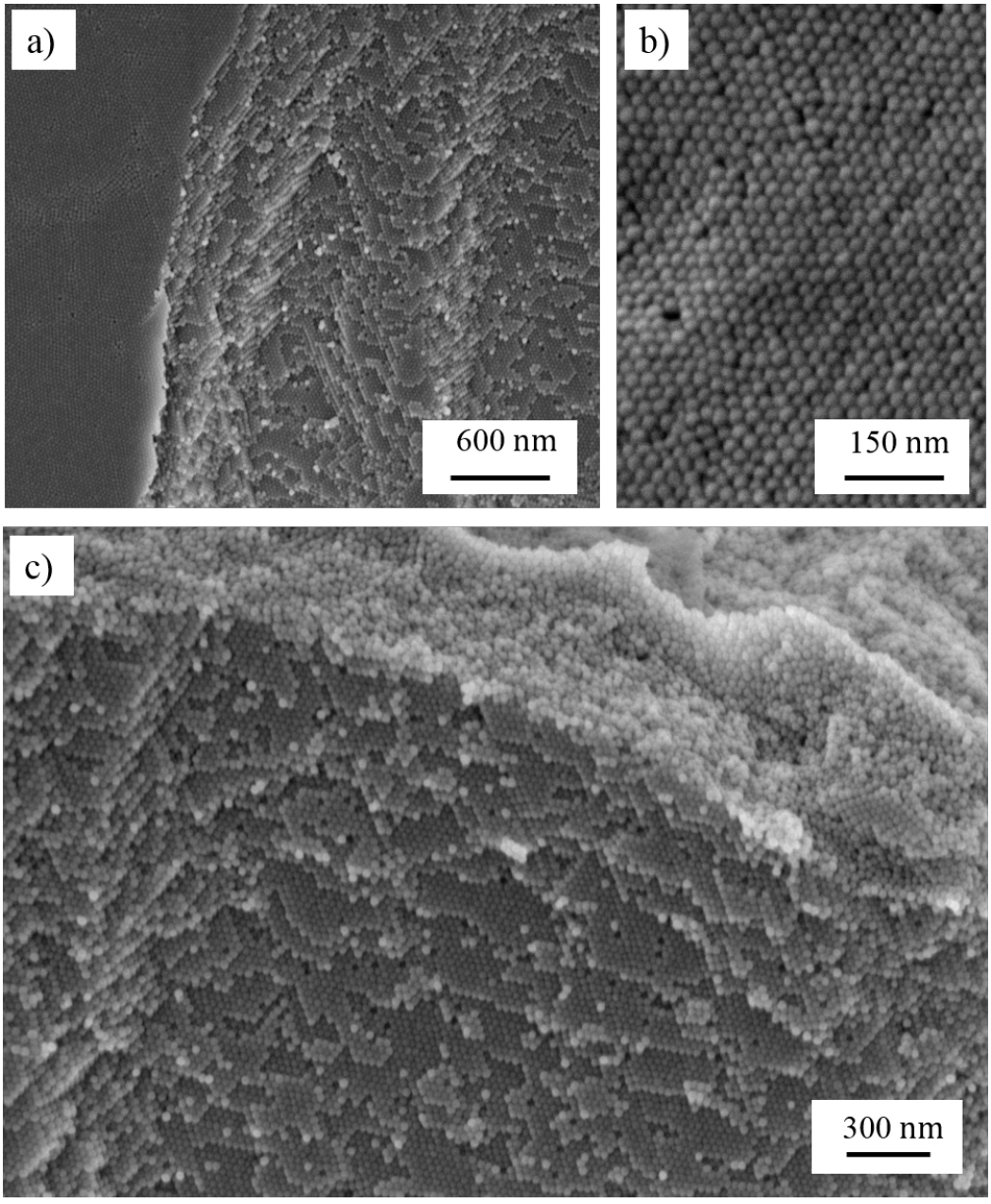

Figure 7.8: SEM images of coatings preparing from nano-silica particles drying under room condition. Pictures a) and b) are top-view micrograph of nano-silica coatings, picture c) is the cross-sectional micrograph of nano-silica coatings at a cracking surface.

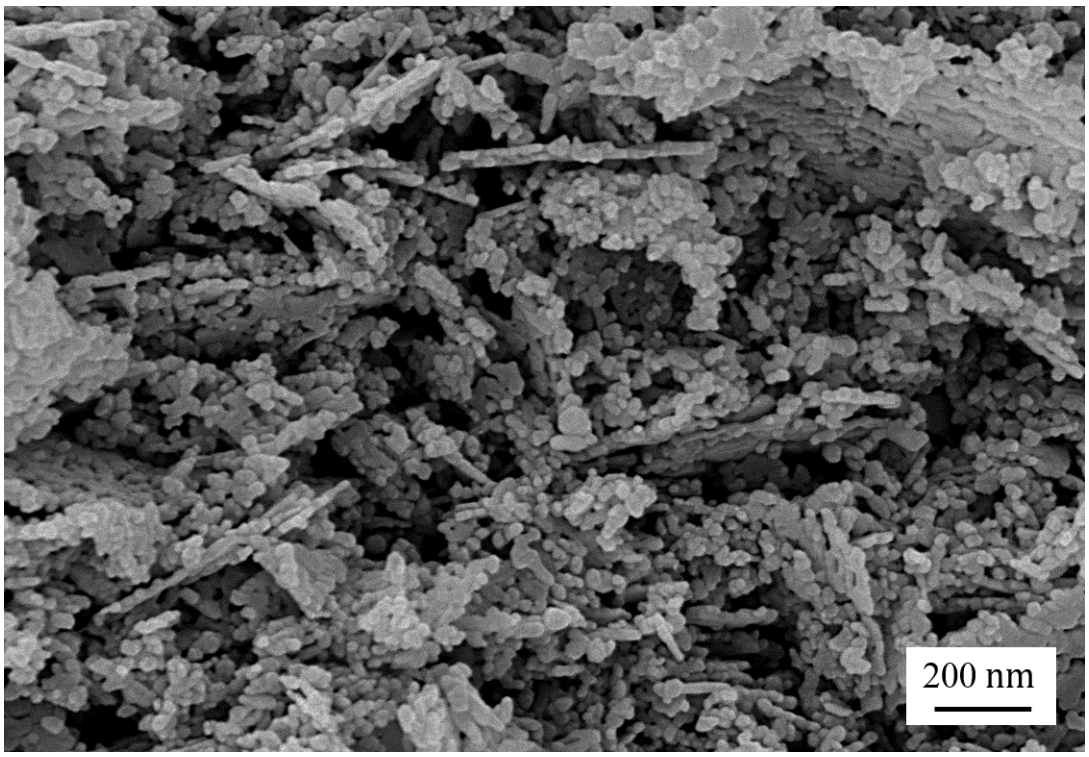

Figure 7.9: SEM cross-sectional micrograph of coatings preparing from zinc oxide particles drying under room condition (23°C ± 1°C and RH of 15%± 2%).

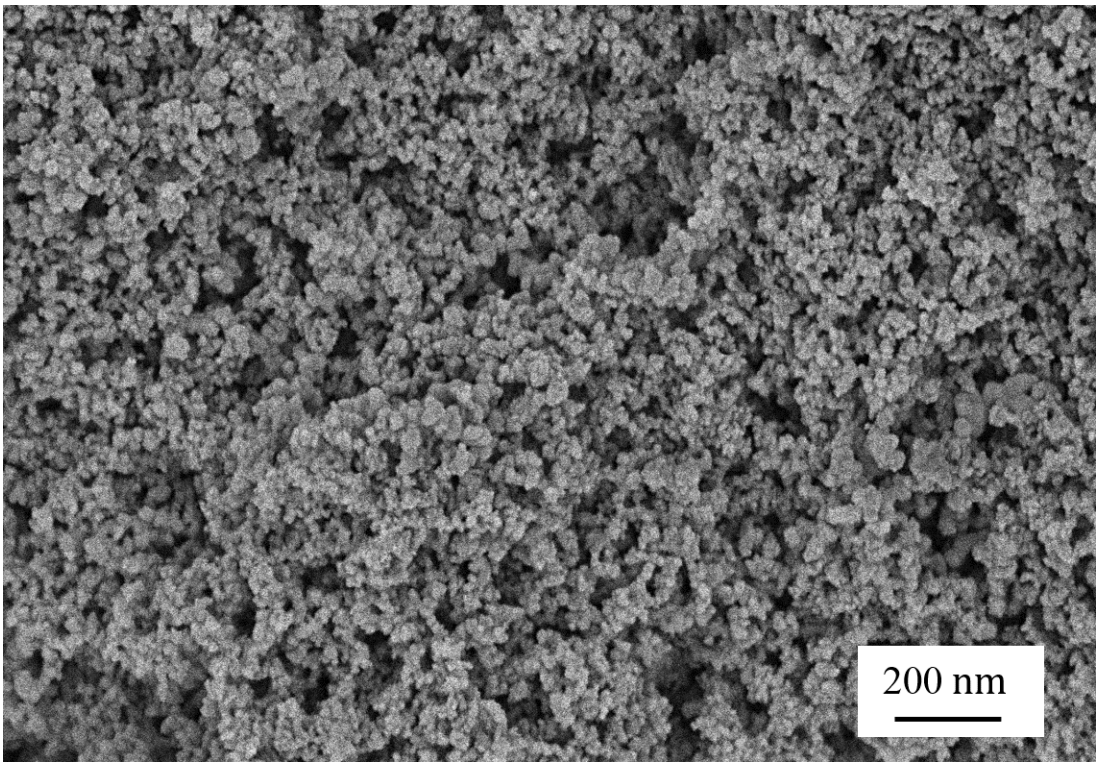

Figure 7.10: SEM cross-sectional micrograph of coatings preparing from fumed-silica particles drying under room condition (23°C ± 1°C and RH of 15%± 2%).

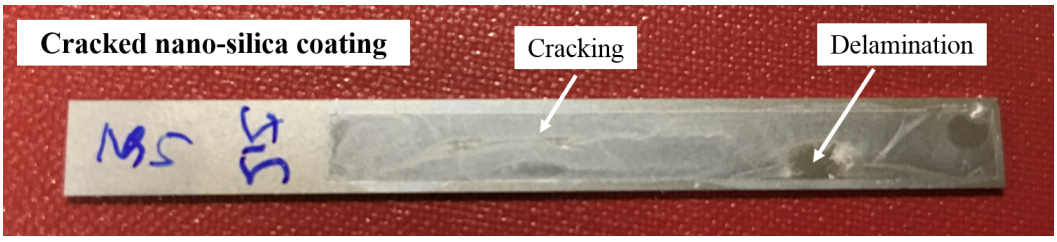

Figure 7.11: Photograph of the cracked coating of diluted nano-silica suspension after running stress measurement test. The stress test was conducted under room condition

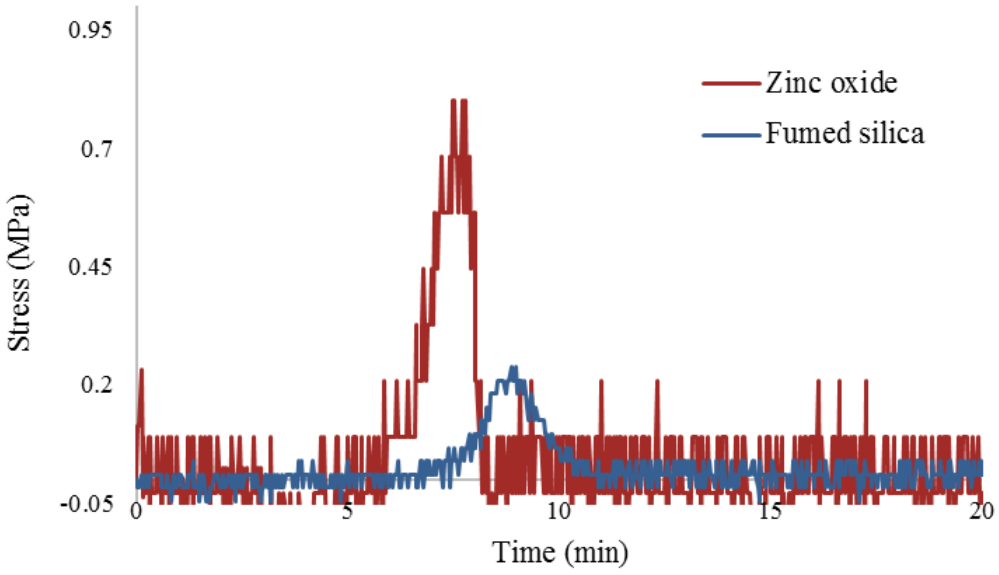

Figure 7.12: Example stress development curves of coatings prepared from zinc oxide particle and fumed-silica particles are plotted. The coating is deposited using 20 uL suspension and drying under room condition.

7.4 Discussion

7.4.1 Drying and Cracking Behaviors of Nanoparticle Coatings

Comparing the coating CCT values, which are closely related to the fracture toughness [101, 135], reveals the mechanical strength of the final coating layers. According to the results listed in Table 7.1, the coatings of zinc oxide particles with both concentrations show the best cracking resistance. These materials are able to form a defect-free coating with thickness three orders of magnitude larger than the particle size without any binder or additive. The CCT of nano-silica coatings and fumed-silica coatings, meanwhile, are much smaller, less than 10 μm. The significant difference observed in coating CCT arouses the interest in the microstructure of these coatings.

The distinct microstructure of coatings prepared from nano-silica particles, zinc oxide particles and fumed-silica particles are shown in Figure 7.8, 7.9 and 7.10, respectively. In nano-silica coatings, monodispersed spherical silica particles form a close-packing of a regular crystalline arrangements [192] and leave very small porespaces. The microstructure of zinc oxide coating, however, is very porous according to the SEM image. The particles are obviously not the isolated pigments in the size of 30-40 nm, as reported by the material data sheet, but form the plate-shape aggregates with the diameter about 300nm - 400nm with high aspect ratio (diameter to thickness). Efforts of establishing a dispersed, stable zinc oxide suspension were made via adjusting the pH of the zinc oxide suspension from 3 to 11 and sonicating for different amounts of time. However, similar microstructures formed by the plate-shape zinc oxide aggregates were observed using SEM. Instead of trying to break up the aggregates, zinc oxide coatings are then considered as the suspensions of nano-sized particles with different size and shape and the testing results are used for investigating the effect of particle geometry on coatings drying and cracking. The fumed-silica particles are produced in a flame and obtain a highly aggregated structure. The aggregates are typically in a size around 22 nm and geometric standard deviation of 1.45 [193], indicating a relatively small aspect ratio. The microstructure of fumed-silica coating is presented in Figure 7.10 which obtains the uniform porous structure.

With the smaller pores formed in the microstructure of fumed-silica coating, higher stress development is expected. However, according to the stress peak values listed in

the Table 7.2, zinc oxide coating develops higher stress (0.87 ±0.10 MPa) than fumed-silica coating (0.19 ±0.06 MPa). The shape of the stress curves presented in Figure 7.12 suggests the capillary force is the major contribution of the stress development of these two nanoparticle coatings. But as introduced in Chapter 2, coatings with smaller particles usually obtain higher stress because the smaller pore size leads stronger capillary pressure. In the comparison of the stress development between zinc oxide coating and fumed-silica coating, it is notable that the thicknesses of the two coatings are very different, which can cause a considerable alteration in stress estimation. The coating of highly aggregated fumed-silica particles has a much larger thickness than the zinc oxide coating with same volume concentration, suggesting a denser packing is formed in the zinc oxide coating with plate-shaped particles. Considering the stress and thickness results, the larger void space seen in Figure 7.9 is possible due to the disruption of the particulate microstructure caused by sample fracture. In addition, the cracking of the fumed-silica sample can also relieve some of the stains developed and leads to lower stress development.

The drying and cracking behaviors of the nanoparticle coatings prepared from mono-dispersed nano-silica, plate-shaped zinc oxide aggregates and highly aggregated fumed-silica were studied and compared. The nano-silica coating prepared with the smallest particle forms a very compacted microstructure and severe cracks during drying which is possibly due to the high stress development resulting from the strong capillary effect. Unfortunately, stress could not be measured in this coating due to cracking. The coating containing the zinc oxide aggregates with high aspect ratio develops very good crackng resistance. The plate-shaped aggregates promote the particle-particle interaction and develop relatively compacted packing. The crackings seen in the CCT test of the zinc-oxide coating suggest less non-uniformity in thickness comparing to the other two coatings. The surface tension measurements for coatings prepared from nano-silica and zinc oxide were taken with a digital tensiometer (Krss, K10ST) using the Wilhelmy method [194]. The surface tension of the diluted zinc oxide coating, which is 63.7 mN/m, is slightly lower than the diluted nano-silica coating (surface tension of 67.8 mN/m). Therefore the zinc oxide coating with the lower surface tension experiences less edge effect since the curved region near the edge of the liquid coating has a smaller capillary length but higher capillary rise [195, 117, 116]. In addition, it is also been found by other

researchers [92] that the particles with high aspect ratio were also found to suppress the "coffee ring" effect and improve the microstructure uniformity. The fumed-silica coatings, containing aggregates with lower aspect ratio, develops very porous structure and different cracking patterns. Considering it stress development measurement results, it is possible that the weak mechanical strength provided by the porous microstructure is the main cause for the cracking behavior.

7.4.2 Evaluation of Current Characterization Approaches

In this work, the beam deflection method and CCT measurement, which are typically used on coatings prepared with micro-sized particles, were applied to characterize nanoparticle coatings. Some limitations were found in the experimental setup and design that could affect the measurement accuracy.

Achieving coatings with uniform thickness and drying with such small thickness was challenging in this work. As discussed in the CCT measurement of nano-silica coatings, the height of the substrate wall was much larger than the wet coating thickness, which can result in significant non-uniformity in final thickness due to the liquid pinning. Decreasing the height of the wall can improve the coating uniformity but limit the wall material to silicon, which is much rigid than PDMS. The effect of using this more rigid wall design on the beam deflection magnitude needs to be further investigated using FEM analysis. In addition, with less coating suspension deposited onto the substrate, the coating area of the substrate needs to be reconsidered. According to the CCT results shown previously, the inability to wet the entire coating area becomes the limiting factor of precisely measuring the CCT of nanoparticle coatings. The dimension of the coating area or cantilever needs to be designed with several restrictions (discussed in Chapter 3) to keep the deflection-stress relationship used in the stress measurement valid.

The magnitude of the deflection in response to the stress development of the thin layer of the nanoparticle coatings can be small and exceed the ability of the current stress development apparatus. The deflection is still recognizable for coatings tested in this work. But as seen in Figure 7.12, the magnitude of the deflection oscillation representing the background noise from the instrument is distinguishable. A new cantilever design with a smaller width and larger length should be able to expand the lower testing limited of the stress measurement.

Measuring the thickness of the final coating is essential for both stress and cracking characterization. However, the nanoparticles coatings can be too porous and weak to support the thickness measurement using digimatic indicator. The indenting of the indicator can crush the porous microstructure and providing an underestimated value.

7.5 Summary

Using the coatings prepared with rigid nanoparticles of different particle morphologies, the coating stress development, microstructure and cracking resistance were investigated. Prepared from the mono-dispersed particles, the nano-silica coatings develop a very compacted particulate network but poor cracking resistance possibility due to the high magnitude of capillary-induced stress. Unfortunately, the stress development data of nano-silica coatings was unable to obtain due to the severe cracking defects. With the nanoparticles aggregated into plate-shape, the zinc oxide coatings show good cracking resistance even with high stress developed during drying. In the relative compacted microstructure of zinc oxide coatings, the high aspect ratio of the plate-shaped aggregates provides a larger contact area between particles, resulting in stronger mechanical strength. The fumed-silica coating has a very porous microstructure and exhibits intense cracking. The cracks sabotage the continuity of the microstructure of fumed-silica coatings thus the mechanical strength and give underestimated stress measurement result due to the strain relief. The results of this work show the importance of the morphology of nanoparticle to coating drying and mechanical properties.

Chapter 8

Conclusion and Future Directions

The work presented in this thesis has provided a detailed study of the roles of some coating formulation variables and processing conditions on drying and cracking behavior of the aqueous particulate coatings. Specifically, parameters of the non-deformable particles in coatings below the CPVC have been the major interests. The goal of this work is to understand the connections between the stress development, microstructure evolution and cracking formation of the coating drying process, and the how they are impacted by particles size and shape. The motivation is to better predict and control the coating performance by optimizing the formulation and designing efficient processing condition. In this chapter, the key findings of the research work are summarized and the possible future directions are discussed.

8.1 Summary

In this work, several particulate coating systems were studied to reveal the effect of formulation variables and processing conditions to the drying and cracking behavior. The study relays on the understanding and characterization of the dynamic changes taken place in coating tensile stress, particulate structure and mechanical strength during drying. The beam deflection method conducted using walled cantilever can measure the stress development during uniform drying. [103] More cantilever designs were developed and evaluated with altered material and dimension to enable the stress measurement of varied coating systems studied in this work. A new approach of characterizing the

microstructure evolution is developed using laser profilometry. Although it cannot capture the particulate microstructure change as well as the cryoSEM technique, the laser profilometer can be used on the coating drying under the exact same condition as in stress measurement, making the correlation of the stress and shrinkage much easier.

Using the particulate coating systems prepared from ground calcium carbonate (GCC) particles, formulation variables such as the particle size, particle size distribution, binder addition, additives addition were investigated. The effect of particle size distribution on coating stress development, microstructure and mechanical strength is the major focus. With the presence of binders, coatings containing particles of wide particle size distribution have a higher stress. The origin of the high-stress level is found to be related to the compacted particle packing. Because of the smaller pore sizes, larger capillary pressures drive the more constrained shrinkage, thus higher stress development. Increase the particle size distribution can improve the coating mechanical strength by forming compacted microstructure, but can also lead to the cracking problem due to the stimulate stress development.

An alternative method has been used in industrial coating design to improve the performance of GCC-based coatings, which is adding platy-shaped clay particles. The role of clay addition, which can also be considered as formulation variable of particle shape, in changing coating drying and cracking behavior was also investigated. The increased amount of clay content with enhanced particle shape complexity was found to intensify the geometry constraints and disrupt the particle rearrangement of the particulate coatings. The hindered shrinkage of the particulate network is responsible for the stress partial relaxation during drying and less cracking formation.

The study of the particle shape effect continues with the investigation of adding clay particles into spherical-shaped silica coating systems instead of the irregular-shaped GCC particles. In this case, more severed cracking was observed when adding clay into silica-based coatings. Blending two pigments with distinct shapes sabotages the continuity of the particulate network and reduces the coating mechanical strength, which altered the coating cracking resistance. In addition, the intrinsic mechanical properties of the particles were found to impact the coating cracking behavior as well.

In the last chapter of this thesis, attention was shifted from the particulate coatings

with the micron-sized particle to those prepared from nano-sized particles. The formulation variables of particle size and shape were investigated in three coating systems containing only rigid nanoparticles. The results of critical cracking thickness and stress development proved the important role of the particle shape. But limitations were also discovered for applying the current stress and cracking characterization approaches on nanoparticle coatings.

8.2 Future Research Directions

8.2.1 Effect of Intrinsic Mechanical Properties of Pigments on Coating Cracking Resistance

A follow-up project can be done to further study the clay addition effect. As introduced in Chapter 6, the different cracking behaviors observed in GCC-based coatings and silica-based coatings by increasing clay content are attributed to both the shape and the intrinsic mechanical properties of the co-blended pigments. However, if the coating systems contain sufficient amounts of binder particles to form a continuous film without pores, the impact of the co-blending pigment shape will be greatly eliminated. In this case, the effect of the particle intrinsic mechanical properties can be revealed by comparing the cracking behavior. Furthermore, by comparing the impact on cracking resistance only by co-blending pigment mechanical properties, to the results of in the previous clay study, the effect of co-blending pigment shape to clay addition can be determined.

8.2.2 Effect of Coating Thickness on Stress Development of Particulate Coatings

The stress development for particulate coatings measured via beam deflection method is found to be influenced by coating thickness. In the drying of soft particulate coatings, complete coalescence forms a homogeneous film with no strain gradient along the thickness direction. Thus the stress development, in this case, should be independent of the coating thickness. However, for capillary-induced stress development, the constrained shrinkage of the particulate network is caused by the curved menisci formation between

particles. It is interesting to find out whether the stain resulted from the capillary effect is uniformly distributed throughout the coating thickness. The mechanism of capillary induced shrinkage for particulate coatings can be explored by characterizing the stress development of coatings with different thickness and estimating the thickness in the order of particle size.

Without the uniform strain assumption, some modifications may need to be done to the equation (the modified Corcoran Equation is currently used) used for deflection-stress calculation. in Corcoran's work, to simplify the calculation, the stress is considered to be concentrated in the center of the coating layer, which is fine when the coating layer is thin. However, it is worthwhile noting that the assumption may not be valid when the strain is depth-depended. Using the relationship derived by Boerman and Perera [97], the Corcoran Equation (Equation 8.1) could be modified as presented below (Equation 8.2).

$$\sigma = \frac{E_s t^3}{6c(t+c)(1-\upsilon_s)r} + \frac{E_c(t+c)}{2(1-\upsilon_c)r} \tag{8.1}$$

$$\sigma = \frac{E_s t^3}{6c(t+c)(1-\upsilon_s)r} + \frac{E_c(3t^2+6tc+4c^2)}{6(t+c)(1-\upsilon_c)r} \tag{8.2}$$

where E is the elastic modulus and υ is the Poisson ratio. The subscripts s and c denote the substrate and the coating layer, respectively. t and c represent the thickness of the substrate and the coating. and the average coating stress σ is related to the curvature of the coated substrate r.

8.2.3 Cracking and Mechanical Properties of Coatings

As achieving the defect-free coatings motivates the coating study, being able to measure the mechanical properties of the coatings layer and characterize the cracking behavior is essential. Some approaches were used in this work to estimate the coating mechanical properties, for example, nanoindentation, CCT test, tensile test using free-stand coating layer, comparing coating deflection using substrates with different thickness. More effort can be made in exploring more mechanical testing methods. For example, if a free-standing coating is available, vibrating membrane technology could be applied to test the elastic modulus value [109]. Otherwise, the modulus could be determined using the

strain gages and DMA to get the strain difference between the coating and substrate [108]. Equation 8.3 derived by Chiu enabled the estimation of the coating modulus.

$$E_c = E_s R \frac{KR + 2K - R}{2R - K + 1} \tag{8.3}$$

$$K = -\frac{\varepsilon_s}{\varepsilon_c} R = \frac{t}{c} \tag{8.4}$$

where ε is the strain detected by strain gage.

References

[1] RW Hoffman. Stress distributions and thin film mechanical properties. *Surface and Interface Analysis*, 3(1):62–66, 1981.

[2] EM Corcoran. Determining stresses in organic coatings using plate beam deflection. *Journal of Paint Technology*, 41(538):635, 1969.

[3] Facts about the paint coatings industry. American Coating Association(ACA), 2017.

[4] T Page McAndrew. Corrosion prevention with electrically conductive polymers. *Trends in Polymer Science*, 1(5):7–12, 1997.

[5] XQ Cao, R Vassen, and D Stoever. Ceramic materials for thermal barrier coatings. *Journal of the European Ceramic Society*, 24(1):1–10, 2004.

[6] Joseph Keddie and Alexander F Routh. *Fundamentals of latex film formation: processes and properties*. Springer Science & Business Media, 2010.

[7] CN Chen, CP Chen, T-Y Dong, TC Chang, MC Chen, HT Chen, and IG Chen. Using nanoparticles as direct-injection printing ink to fabricate conductive silver features on a transparent flexible pet substrate at room temperature. *Acta Materialia*, 60(16):5914–5924, 2012.

[8] Aristippos Gennadios, Milford A Hanna, and Lyndon B Kurth. Application of edible coatings on meats, poultry and seafoods: a review. *LWT-Food Science and Technology*, 30(4):337–350, 1997.

[9] Duan Jianglian and Zhang Shaoying. Application of chitosan based coating in fruit and vegetable preservation: a review. *J. Food Process. Technol*, 4(5), 2013.

[10] Brian L Bates, Anthony O Ragheb, Joseph M Stewart IV, William J Bourdeau, Brian D Choules, James D Purdy, and Neal E Fearnot. Coated medical device, 2015. US Patent 8,974,522.

[11] Daniel C Leslie, Anna Waterhouse, Julia B Berthet, Thomas M Valentin, Alexander L Watters, Abhishek Jain, Philseok Kim, Benjamin D Hatton, Arthur Nedder, Kathryn Donovan, et al. A bioinspired omniphobic surface coating on medical devices prevents thrombosis and biofouling. *Nature biotechnology*, 32(11):1134, 2014.

[12] Brian G Prevo, Emily W Hon, and Orlin D Velev. Assembly and characterization of colloid-based antireflective coatings on multicrystalline silicon solar cells. *Journal of Materials Chemistry*, 17(8):791–799, 2007.

[13] Richard R Berube, John S Babiec Jr, M Phillip Jameson, Andrew R Negele, and Mitchell J Willis. Calcined kaolin clay filler pigment for enhancing opacity and printing properties of newsprint and mechanical papers, April 30 1991. US Patent 5,011,534.

[14] Zongxue Yu, Liang Lv, Yu Ma, Haihui Di, and Yi He. Covalent modification of graphene oxide by metronidazole for reinforced anti-corrosion properties of epoxy coatings. *RSC Advances*, 6(22):18217–18226, 2016.

[15] Y Natsume and H Sakata. Zinc oxide films prepared by sol-gel spin-coating. *Thin solid films*, 372(1-2):30–36, 2000.

[16] GangYin Yan, Xin Zhang, Peng Huang, Lei Wang, Fang Qi, and BoXue Feng. Influence of deposition time on the morphology and optical properties of sio2-zno composite photonic crystals. *Chinese Science Bulletin*, 56(6):562–566, 2011.

[17] Lili Hu, Toshinobu Yoko, Hiromitsu Kozuka, and Sumio Sakka. Effects of solvent on properties of solgel-derived tio2 coating films. *Thin Solid Films*, 219(1):18 – 23, 1992.

[18] Woo Jin Hyun, Sooman Lim, Bok Yeop Ahn, Jennifer A Lewis, C Daniel Frisbie, and Lorraine F Francis. Screen printing of highly loaded silver inks on plastic substrates using silicon stencils. *ACS applied materials & interfaces*, 7(23):12619–12624, 2015.

[19] Ting Chen, Margaret Joyce, Paul D Fleming, Do Ik Lee, and Steven Bloembergen. Pigmented formulations containing biobased nanoparticle binders for curtain coating applications; part 2: Curtain stability study. In *Paper Conference and Trade Show, PaperCon 2016*. TAPPI Press, 2016.

[20] Chao Liu, Haishun Du, Lv Dong, Xin Wang, Yuedong Zhang, Guang Yu, Bin Li, Xindong Mu, Hui Peng, and Huizhou Liu. Properties of nanocelluloses and their application as rheology modifier in paper coating. *Industrial & Engineering Chemistry Research*, 56(29):8264–8273, 2017.

[21] Tingji Tang, Feng Liang, Loan Vo, and Philip D Nguyen. Compositions and methods for controlling particulate migration in a subterranean formation, August 2 2016. US Patent 9,404,031.

[22] F Boudjouan, A Chelouche, T Touam, D Djouadi, S Khodja, M Tazerout, Y Ouerdane, and Z Hadjoub. Effects of stabilizer ratio on photoluminescence properties of sol-gel zno nano-structured thin films. *Journal of Luminescence*, 158:32–37, 2015.

[23] Wiley. *Processing and Finishing of Polymeric Materials, 2 Volume Set*, volume 1. John Wiley & Sons, 2011.

[24] Pablo Carpio, Emilie Bannier, Mara Dolores Salvador, Amparo Borrell, Rodrigo Moreno, and Enrique Snchez. Effect of particle size distribution of suspension feedstock on the microstructure and mechanical properties of suspension plasma spraying ysz coatings. *Surface and Coatings Technology*, 268:293 – 297, 2015. 6th Rencontres Internationales de la Projection Thermique.

[25] Leon L Shaw, Daniel Goberman, Ruiming Ren, Maurice Gell, Stephen Jiang, You Wang, T Danny Xiao, and Peter R Strutt. The dependency of microstructure and

properties of nanostructured coatings on plasma spray conditions. *Surface and coatings technology*, 130(1):1–8, 2000.

[26] Weihua Li and Satish Kumar. Thin-film coating of surfactant-laden liquids on rotating cylinders. *Physics of Fluids*, 27(7):072106, 2015.

[27] Alexander F Routh. Drying of thin colloidal films. *Reports on Progress in Physics*, 76(4):046603, 2013.

[28] George L Brown. Formation of films from polymer dispersions. *Journal of Polymer Science Part A: Polymer Chemistry*, 22(102):423–434, 1956.

[29] Tuoqi Li, Michael J Heinzer, Erica M Redline, Feng Zuo, Frank S Bates, and Lorraine F Francis. Microstructure and performance of block copolymer modified epoxy coatings. *Progress in Organic Coatings*, 77(7):1145–1154, 2014.

[30] Dinguo Chen. Anti-reflection (ar) coatings made by sol–gel processes: a review. *Solar Energy Materials and Solar Cells*, 68(3-4):313–336, 2001.

[31] LF Francis, AV McCormick, DM Vaessen, and JA Payne. Development and measurement of stress in polymer coatings. *Journal of Materials Science*, 37(22):4717–4731, 2002.

[32] Ernesto Caner, Ramin Farnood, and Ning Yan. Effect of the coating formulation on the gloss properties of coated papers. In *International Printing and Graphic Arts Conference, Miami, FL*, 2006.

[33] Yasmina Dkhissi, Steffen Meyer, Dehong Chen, Hasitha C Weerasinghe, Leone Spiccia, Yi-Bing Cheng, and Rachel A Caruso. Stability comparison of perovskite solar cells based on zinc oxide and titania on polymer substrates. *ChemSusChem*, 9(7):687–695, 2016.

[34] Do Ik Lee. The effects of latex coalescence and interfacial crosslinking on the mechanical properties of latex films. *Polymer*, 46(4):1287–1293, 2005.

[35] Sarah T Eckersley and Alfred Rudin. Mechanism of film formation from polymer latexes. *JCT, Journal of coatings technology*, 62(780):89–100, 1990.

[36] RL Smith. Review of glycol ether and glycol ether ester solvents used in the coating industry. *Environmental health perspectives*, 57:1, 1984.

[37] T Salthammer. Emission of volatile organic compounds from furniture coatings. *Indoor Air*, 7(3):189–197, 1997.

[38] Kevin W McCreight, Rebecca Stockl, Carlo Testa, and Kab Sik Seo. Development of low voc additives to extend the wet edge and open time of aqueous coatings. *Progress in Organic Coatings*, 72(1-2):102–108, 2011.

[39] H Lei, JA Payne, AV McCormick, LF Francis, WW Gerberich, and LE Scriven. Stress development in drying coatings. *Journal of Applied Polymer Science*, 81(4):1000–1013, 2001.

[40] Robert D Deegan, Olgica Bakajin, Todd F Dupont, Greg Huber, Sidney R Nagel, and Thomas A Witten. Contact line deposits in an evaporating drop. *Physical review E*, 62(1):756, 2000.

[41] Yuri O Popov. Evaporative deposition patterns: spatial dimensions of the deposit. *Physical Review E*, 71(3):036313, 2005.

[42] Hua Hu and Ronald G Larson. Analysis of the microfluid flow in an evaporating sessile droplet. *Langmuir*, 21(9):3963–3971, 2005.

[43] Alexander F Routh and William B Zimmerman. Distribution of particles during solvent evaporation from films. *Chemical Engineering Science*, 59(14):2961–2968, 2004.

[44] Richard Buscall and Lee R White. The consolidation of concentrated suspensions. part 1.the theory of sedimentation. *Journal of the Chemical Society, Faraday Transactions 1: Physical Chemistry in Condensed Phases*, 83(3):873–891, 1987.

[45]

[46] Christine M Cardinal, Yoon Dong Jung, Kyung Hyun Ahn, and LF Francis. Drying regime maps for particulate coatings. *AIChE journal*, 56(11):2769–2780, 2010.

[47] Lucas Goehring, William J Clegg, and Alexander F Routh. Solidification and ordering during directional drying of a colloidal dispersion. *Langmuir*, 26(12):9269–9275, 2010.

[48] Yue Ma, HT Davis, and LE Scriven. Microstructure development in drying latex coatings. *Progress in Organic Coatings*, 52(1):46–62, 2005.

[49] Felix Buss, Christine C. Roberts, Kathleen S. Crawford, Katharina Peters, and Lorraine F. Francis. Effect of soluble polymer binder on particle distribution in a drying particulate coating. *Journal of Colloid and Interface Science*, 359(1):112 – 120, 2011.

[50] Xiao Liu, Weiping Liu, Amanda J. Carr, Dayalis Santiago Vazquez, Dmytro Nykypanchuk, Pawel W. Majewski, Alexander F. Routh, and Surita R. Bhatia. Stratification during evaporative assembly of multicomponent nanoparticle films. *Journal of Colloid and Interface Science*, 515:70 – 77, 2018.

[51] Susanna Baesch, Kyle Price, Philip Scharfer, Lorraine Francis, and Wilhelm Schabel. Influence of the drying conditions on the particle distribution in particle filled polymer films: Experimental validation of predictive drying regime maps. *Chemical Engineering and Processing: Process Intensification*, 123:138–147, 2018.

[52] Susanna Baesch, Philip Scharfer, Wilhelm Schabel, and Lorraine Francis. Influence of the drying conditions on the particle distribution in particle-filled polymer films: Predictive simulation of the particle distribution during drying. *Journal of Composite Materials*, 51(24):3391–3403, 2017.

[53] Stefan Jaiser, Marcus Mller, Michael Baunach, Werner Bauer, Philip Scharfer, and Wilhelm Schabel. Investigation of film solidification and binder migration during drying of li-ion battery anodes. *Journal of Power Sources*, 318:210 – 219, 2016.

[54] Sean X Pan, HT Davis, and LE Scriven. Modeling moisture distribution and binder migration in drying paper coatings. *Tappi journal (USA)*, 1995.

[55] SC Nowicki, HT Davis, and LE Scriven. Microscopic determination of transport paraheters in drying porous media. *Drying Technology*, 10(4):925–946, 1992.

[56] George W Scherer. Theory of drying. *Journal of the American Ceramic Society*, 73(1):3–14, 1990.

[57] John C Berg. *An introduction to interfaces & colloids: the bridge to nanoscience*. World Scientific, 2010.

[58] William B Haines. Studies in the physical properties of soils: Iv. a further contribution to the theory of capillary phenomena in soil. *The Journal of Agricultural Science*, 17(2):264–290, 1927.

[59] William B Haines. Studies in the physical properties of soil. v. the hysteresis effect in capillary properties, and the modes of moisture distribution associated therewith. *The Journal of Agricultural Science*, 20(1):97–116, 1930.

[60] Erin Glaser Arlinghaus. *Microflows, pore and matrix evolution in latex coatings*. 2004.

[61] Stefan Lampenscherf, Wolfgang Pompe, and David S Wilkinson. Stress development due to capillary condensation in powder compacts: A two-dimensional model study. *Journal of the American Ceramic Society*, 83(6):1333–1340, 2000.

[62] LA Pekurovsky and LE Scriven. On capillary forces and stress in drying latex coating. ACS Publications, 2001.

[63] Alexander F Routh and William B Russel. A process model for latex film formation: Limiting regimes for individual driving forces. *Langmuir*, 17(23):7446–7447, 2001.

[64] Alexander F Routh and William B Russel. Deformation mechanisms during latex film formation: Experimental evidence. *Industrial & engineering chemistry research*, 40(20):4302–4308, 2001.

[65] JW Vanderhoff, HL Tarkowski, MC Jenkins, and EB Bradford. Theoretical consideration of interfacial forces involved in coalescence of latex particles. *Rubber Chemistry and Technology*, 40(4):1246–1269, 1967.

[66] Sarah T Eckersley and Alfred Rudin. Mechanism of film formation from polymer latexes. *JCT, Journal of coatings technology*, 62(780):89–100, 1990.

[67] RE Dillon, LA Matheson, and EB Bradford. Sintering of synthetic latex particles. *Journal of Colloid Science*, 6(2):108–117, 1951.

[68] DP Sheetz. Formation of films by drying of latex. *Journal of Applied Polymer Science*, 9(11):3759–3773, 1965.

[69] Xiaobo Gong, H Ted Davis, and LE Scriven. Role of van der waals force in latex film formation. *Journal of Coatings Technology and Research*, 5(3):271–283, 2008.

[70] Lyudmila A Pekurovsky. *Capillary forces and stress development in drying latex coating.* PhD thesis, University of Minnesota, 2005.

[71] WK Asbeck and Maurice Van Loo. Critical pigment volume relationships. *Industrial & Engineering Chemistry*, 41(7):1470–1475, 1949.

[72] Giuliano M Laudone, G Peter Matthews, and Patrick AC Gane. Effect of latex volumetric concentration on void structure, particle packing, and effective particle size distribution in a pigmented paper coating layer. *Industrial engineering chemistry research*, 45(6):1918–1923, 2006.

[73] Ludwig Huggenberger, Werner Kogler, and Manfred Arnold. Future role of gound calcium carbonate in paper coating. *Tappi*, 62(5):37–41, 1979.

[74] Emine Bakan, Daniel Emil Mack, Georg Mauer, Robert Mücke, and Robert Vaßen. Porosity–property relationships of plasma-sprayed gd2zr2o7/ysz thermal barrier coatings. *Journal of the American Ceramic Society*, 98(8):2647–2654, 2015.

[75] Babar Hussain, Abasifreke Ebong, and Ian Ferguson. Zinc oxide as an active n-layer and antireflection coating for silicon based heterojunction solar cell. *Solar Energy Materials and Solar Cells*, 139:95–100, 2015.

[76] KK Gaikwad and S Ko. Overview on in polymer-nano clay composite paper coating for packaging application. *J Material Sci Eng*, 4(151):2169–0022, 2015.

[77] JC Husband, JS Preston, LF Gate, A Storer, and P Creaton. A study of in-plane and z-direction strength of coating layers with varying latex content. In *6th International Paper and Coating Chemistry Symposium, Stockholm*, pages 10–16, 2006.

[78] Qunna Xu, Qianqian Fan, Jianzhong Ma, and Ziqiang Yan. Facile synthesis of casein-based tio2 nanocomposite for self-cleaning and high covering coatings: Insights from tio2 dosage. *Progress in Organic Coatings*, 99:223–229, 2016.

[79] Qiaoling Kang, Yan Bao, Miao Li, and Jianzhong Ma. Effect of wall thickness of hollow tio2 spheres on properties of polyacrylate film: Thermal insulation, uv-shielding and mechanical property. *Progress in Organic Coatings*, 112:153–161, 2017.

[80] Rahimeh Nosrati, Ali Olad, and Hamideh Najjari. Study of the effect of tio2/polyaniline nanocomposite on the self-cleaning property of polyacrylic latex coating. *Surface and Coatings Technology*, 316:199–209, 2017.

[81] Gerardo del Rio and Alfred Rudin. Latex particle size and cpvc. *Progress in Organic Coatings*, 28(4):259 – 270, 1996.

[82] Ming Lei, Lorraine F. Francis, and L. E. Scriven. Correlation of hardness with mfft and cpvc of latex/ceramic coatings. *Journal of Coatings Technology*, 75(945):95–102, 2003.

[83] Ederley Velez Oritz and Restrepo Julian. Towards a new model for the calculation of cpvc in latex coatings. *Surface Coatings International. JOCCA Journal of the Oil & Colour Chemist's Association; 98, 3; 133-136*, 2017.

[84] Hui Luo. *Microstructure development in particulate composite coatings by cryo-SEM*. University of Minnesota, 2007.

[85] Raymond C Chiu, TJ Garino, and MJ Cima. Drying of granular ceramic films: I, effect of processing variables on cracking behavior. *Journal of the American Ceramic Society*, 76(9):2257–2264, 1993.

[86] Alexander F Routh and William B Russel. Horizontal drying fronts during solvent evaporation from latex films. *AIChE Journal*, 44(9):2088–2098, 1998.

[87] Kyle K Price, Alon V McCormick, and Lorraine F Francis. Cryosem investigation of latex coatings dried in walled substrates. *Langmuir*, 28(28):10329–10333, 2012.

[88] Raymond C Chiu and Michael J Cima. Drying of granular ceramic films: Ii, drying stress and saturation uniformity. *Journal of the American Ceramic Society*, 76(11):2769–2777, 1993.

[89] Yan Wu and Lorraine F Francis. Effect of particle size distribution on stress development and microstructure of particulate coatings. *Journal of Coatings Technology and Research*, 14(2):455–465, 2017.

[90] Robert D Deegan. Pattern formation in drying drops. *Physical review E*, 61(1):475, 2000.

[91] JM Salamanca, E Ciampi, DA Faux, PM Glover, PJ McDonald, AF Routh, ACIA Peters, R Satguru, and JL Keddie. Lateral drying in thick films of waterborne colloidal particles. *Langmuir*, 17(11):3202–3207, 2001.

[92] PJ Yunker, AG Yodh, and T Still. Colloidal shape effects in evaporating drops. *Physics of Complex Colloids*, 184:447, 2013.

[93] Manish Chopra, Lei Li, Hua Hu, Mark A Burns, and Ronald G Larson. Dna molecular configurations in an evaporating droplet near a glass surface. *Journal of Rheology*, 47(5):1111–1132, 2003.

[94] Ralf Blossey and Andreas Bosio. Contact line deposits on cdna microarrays: a twin-spot effect. *Langmuir*, 18(7):2952–2954, 2002.

[95] Raymond C Rowe. Film/tablet adhesion, film thickness, internal stresses and bridging of the intagliationsa unified model with practical implications. *European journal of pharmaceutical sciences*, 30(3-4):236–239, 2007.

[96] Ladislas P Kubin, Robin L Selinger, John L Bassani, and Kyeongjae Cho. Multiscale modeling of materials2000. *Mater. Res. Soc. Proc. 653, Materials Research Society, Warrendale, PA*, 2001.

[97] Annelies E Boerman and Dan Y Perera. Measurement of stress in multicoat systems. *Journal of Coatings Technology*, 70(881):69–75, 1998.

[98] Edward D Cohen, Edwin J Lightfoot, and Edgar B Gutoff. A primer on forming coatings. *Chemical engineering progress*, 86(9):30–36, 1990.

[99] CH Hare. Internal stress-related coating system failures. *Journal of Protective Coatings & Linings*, 13(10), 1996.

[100] AG Evans, MD Drory, and MS Hu. The cracking and decohesion of thin films. *Journal of materials research*, 3(5):1043–1049, 1988.

[101] Michael D Thouless. Cracking and delamination of coatings. *Journal of Vacuum Science & Technology A: Vacuum, Surfaces, and Films*, 9(4):2510–2515, 1991.

[102] H Lei, LF Francis, WW Gerberich, and LE Scriven. Stress development in drying coatings after solidification. *AIChE journal*, 48(3):437–451, 2002.

[103] Kyle K Price, Yan Wu, Alon V McCormick, and Lorraine F Francis. Stress development in hard particle coatings in the absence of lateral drying. *Journal of the American Ceramic Society*, 98(7):2214–2222, 2015.

[104] E Santanach Carreras, F Chabert, DE Dunstan, and GV Franks. Avoiding mud cracks during drying of thin films from aqueous colloidal suspensions. *Journal of colloid and interface science*, 313(1):160–168, 2007.

[105] Karnail B Singh and Mahesh S Tirumkudulu. Cracking in drying colloidal films. *Physical review letters*, 98(21):218302, 2007.

[106] Karnail B Singh, Laxman R Bhosale, and Mahesh S Tirumkudulu. Cracking in drying colloidal films of flocculated dispersions. *Langmuir*, 25(8):4284–4287, 2009.

[107] Monica Schneider, Johannes Maurath, Steffen B Fischer, Moritz Weiß, Norbert Willenbacher, and Erin Koos. Suppressing crack formation in particulate systems by utilizing capillary forces. *ACS applied materials & interfaces*, 9(12):11095–11105, 2017.

[108] Chin-Chen Chiu. Determination of the elastic modulus and residual stresses in ceramic coatings using a strain gage. *Journal of the American Ceramic Society*, 73(7):1999–2005, 1990.

[109] A Jagota, S Mazur, and RJ Farrisf. A vibrational technique for stress measurement in films. *MRS Online Proceedings Library Archive*, 188, 1990.

[110] G Gerald Stoney. The tension of metallic films deposited by electrolysis. In *Proc. R. Soc. Lond. A*, volume 82, pages 172–175. The Royal Society, 1909.

[111] Karan Jindal. Stress development in particulate, nano-composite and polymeric coatings. 2009.

[112] Jason Alan Payne. *Stress evolution in solidifying coatings*. 1998.

[113] Kyle Kirk-Arthur Price. *Stress and microstructure development in particle-based coatings*. PhD thesis, University of Minnesota, 2014.

[114] Matthew A Hopcroft, William D Nix, and Thomas W Kenny. What is the young's modulus of silicon? *Microelectromechanical Systems, Journal of*, 19(2):229–238, 2010.

[115] Diane Melissa Vaessen. Stress and structure development in polymeric coatings. 2002.

[116] Josiah Willard Gibbs. *The scientific papers of J. Willard Gibbs*, volume 1. Longmans, Green and Company, 1906.

[117] JF Oliver, C Huh, and SG Mason. Resistance to spreading of liquids by sharp edges. *Journal of Colloid and Interface Science*, 59(3):568–581, 1977.

[118] Zhixin Wang. *Polydimethylsiloxane mechanical properties measured by macroscopic compression and nanoindentation techniques*. University of South Florida, 2011.

[119] Hitachi High-Technologies Corporation. *Ultra-high Resolution Scanning Electron Microscope Regulus Series*.

[120] Robert P Apkarian. Introduction: High resolution cryo-sem in the biological sciences. *Microscopy and Microanalysis*, 9(4):272–272, 2003.

[121] J Bastacky, C Wodley, R LaBrie, and C Backhus. A bibliography of low-temperature scanning electron microscopy (ltsem, cryo-sem) and scanning electron microscopy of frozen hydrated biological systems. *Scanning*, 9(5):219–225, 1987.

[122] Robert P Apkarian, Elizabeth R Wright, Victor A Seredyuk, Susan Eustis, L Andrew Lyon, Vincent P Conticello, and Fredric M Menger. In-lens cryo-high resolution scanning electron microscopy: methodologies for molecular imaging of self-assembled organic hydrogels. *Microscopy and Microanalysis*, 9(4):286–295, 2003.

[123] Patrick Echlin. Recent advances in specimen coating techniques. *Scanning Electron Microscopy*, 1:79–90, 1981.

[124] Erwin Sutanto, Yue Ma, HT Davis, and LE Scriven. Cryogenic scanning electron microscopy of early stages of film formation in drying latex coatings. ACS Publications, 2001.

[125] Hui Luo, LE Scriven, and Lorraine F Francis. Cryo-sem studies of latex/ceramic nanoparticle coating microstructure development. *Journal of colloid and interface science*, 316(2):500–509, 2007.

[126] Xiaobo Gong, H Ted Davis, and LE Scriven. Role of van der waals force in latex film formation. *Journal of Coatings Technology and Research*, 5(3):271–283, 2008.

[127] Patrick Echlin. *Low-temperature microscopy and analysis*. Springer Science & Business Media, 2013.

[128] KP Ryan, DH Purse, SG Robinson, and JW Wood. The relative efficiency of cryogens used for plunge-cooling biological specimens. *Journal of Microscopy*, 145(1):89–96, 1987.

[129] Patrick Echlin. *Low-temperature microscopy and analysis*. Springer Science & Business Media, 2013.

[130] Bugao Xu, DF Cuminato, and NM Keyes. Evaluating fabric smoothness appearance with a laser profilometer. *Textile Research Journal*, 68(12):900–906, 1998.

[131] Jose M Rodriguez, Richard V Curtis, and David W Bartlett. Surface roughness of impression materials and dental stones scanned by non-contacting laser profilometry. *dental materials*, 25(4):500–505, 2009.

[132] Abraham B Bashaiwoldu, F Podczeck, and JM Newton. The application of non-contact laser profilometry to the determination of permanent structural change induced by compaction of pellets: Ii. pellets dried by different techniques. *European journal of pharmaceutical sciences*, 22(1):55–61, 2004.

[133] KEYENCE Corporation. *Ultra-High Speed In-line Profilometer LJ-V7000 Series, User's Manual*.

[134] Tess Marconie. Evaluating the use of a non-contact laser profilometer to measure shrinkage of particulate coatings. Unpublished Manuscript, 2017.

[135] MS Hu, Michael D Thouless, and Anthony G Evans. The decohesion of thin films from brittle substrates. *Acta Metallurgica*, 36(5):1301–1307, 1988.

[136] Ya Yan, Shi-Zhao Kang, and Jin Mu. Preparation of high quality ag film from ag nanoparticles. *Applied surface science*, 253(10):4677–4679, 2007.

[137] R Pilliar. Surgical prosthetic device with porous metal coating, 1974.

[138] Maria Bardosova, Frank C Dillon, Martyn E Pemble, Ian M Povey, and Richard H Tredgold. Langmuirblodgett assembly of colloidal photonic crystals using silica particles prepared without the use of surfactant molecules. *Journal of colloid and interface science*, 333(2):816–819, 2009.

[139] Karel Van Acker, D Vanhoyweghen, Retal Persoons, and J Vangrunderbeek. Influence of tungsten carbide particle size and distribution on the wear resistance of laser clad wc/ni coatings. *Wear*, 258(1-4):194–202, 2005.

[140] Zhaoqing Lu, Meiyun Zhang, Renrong Wang, and Guoquan Wu. Particle size distribution and packing structure of calcium carbonate pigments: effect on art paper characteristics. *Appita Journal: Journal of the Technical Association of the Australian and New Zealand Pulp and Paper Industry*, 61(5):379, 2008.

[141] Sanjay Tyagi, AK Ray, and YV Sood. Surface characteristics of coating layers formed by coating pigments with different particle sizes and size distribution. *Journal of coatings technology and research*, 7(6):747–756, 2010.

[142] Nina Barth, Carsten Schilde, and Arno Kwade. Influence of particle size distribution on micromechanical properties of thin nanoparticulate coatings. *Physics Procedia*, 40:9 – 18, 2013. European Conference on Nano Films - ECNF2012.

[143] Pär Wedin, Carlos J Martinez, Jennifer A Lewis, John Daicic, and Lennart Bergström. Stress development during drying of calcium carbonate suspensions containing carboxymethylcellulose and latex particles. *Journal of colloid and interface science*, 272(1):1–9, 2004.

[144] Joseph Cesarano, Ilhan A Aksay, and Alan Bleier. Stability of aqueous α-al2o3 suspensions with poly (methacrylic acid) polyelectrolyte. *Journal of the American Ceramic Society*, 71(4):250–255, 1988.

[145] Carlos J Martinez and Jennifer A Lewis. Shape evolution and stress development during latex-silica film formation. *Langmuir*, 18(12):4689–4698, 2002.

[146] Jason A Payne, Alon V McCormick, and Lorraine F Francis. In situ stress measurement apparatus for liquid applied coatings. *Review of scientific instruments*, 68(12):4564–4568, 1997.

[147] Andy D Ward and Stanley W Trimble. *Environmental hydrology*. Crc Press, 2003.

[148] C Jeffrey Brinker and George W Scherer. *Sol-gel science: the physics and chemistry of sol-gel processing*. Academic press, 2013.

[149] Christine C Roberts and Lorraine F Francis. Drying and cracking of soft latex coatings. *Journal of Coatings Technology and Research*, 10(4):441–451, 2013.

[150] GM Laudone, GP Matthews, and PAC Gane. Coating shrinkage during evaporation: Observation, measurement and modelling within a network structure. In *Proceedings of the 2003 TAPPI 8th Advanced Coating Fundamentals Symposium*, pages 8–10, 2003.

[151] J Watanabe and P Lepoutre. A mechanism for the consolidation of the structure of clay–latex coatings. *Journal of Applied Polymer Science*, 27(11):4207–4219, 1982.

[152] HH Murray and WD Keller. Kaolins, kaolins and kaolins in: Murray hh, bundy, wm & harvey, cc,(eds), kaolin genesis and utilization. *The Clay Minerals Society, Boulder, CO*, 1993.

[153] Haydn H Murray. Overviewclay mineral applications. *Applied Clay Science*, 5(5-6):379–395, 1991.

[154] Haydn H Murray and Jessica Elzea Kogel. Engineered clay products for the paper industry. *Applied Clay Science*, 29(3-4):199–206, 2005.

[155] IR Wilson. Current world status of kaolin from south-west england. *GEOSCIENCE IN SOUTH WEST ENGLAND*, 10(4):417–423, 2003.

[156] K Rissa, T Lepistö, and K Yrjölä. Effect of kaolin content on structure and functional properties of water-based coatings. *Progress in organic coatings*, 55(2):137–141, 2006.

[157] JC Husband, LF Gate, N Norouzi, and D Blair. The influence of kaolin shape factor on the stiffness of coated papers. *Tappi Journal*, 8(6):12–17, 2009.

[158] WM Bundy. The diverse industrial applications of kaolin. pp. 43à47 in: Kaolin genesis and utilization (hh murray, w. bundy & c. harvey, editors). special publication 1. *The Clay Minerals Society, Boulder, Colorado, USA*, 1993.

[159] Krassimir D Danov and Peter A Kralchevsky. Capillary forces between particles at a liquid interface: General theoretical approach and interactions between capillary multipoles. *Advances in colloid and interface science*, 154(1-2):91–103, 2010.

[160] AG Hiorns, NJ Elton, L Coggon, and DJ Parsons. Analysis of differences in coating structure induced through variable calendering conditions. In *COATING PAPERMAKERS CONFERENCE*, pages 583–602. TAPPI PRESS, 1998.

[161] WM Bundy, WD Johns, and HH Murray. Physico-chemical properties of kaolinite and relationship to paper coating quality. *Tappi*, 48(12):688–695, 1965.

[162] P Lepoutre and M Rigdahl. Analysis of the effect of porosity and pigment shape on the stiffness of coating layers. *Journal of materials science*, 24(8):2971–2974, 1989.

[163] M Inoue and P Lepoutre. Influence of structure and surface chemistry on the cohesion of paper coatings. *Journal of adhesion science and technology*, 6(7):851–857, 1992.

[164] JC Husband, JS Preston, LF Gate, D Blair, and P Creaton. Factors affecting the printing strength of kaolin-based paper coatings. *TAGA Journal*, 84, 2008.

[165] Patrick AC Gane, Jeremy J Hooper, and Andreas Grunwald. Coating pigment orientation: A comparative analysis of the application mechanisms and properties of blade and roll coatings. *Tappi journal.–*, 1997.

[166] HH Morris, P Sennett, and RJ Drexel. Delaminated claysphysical properties and paper coating properties. *Tappi*, 48(12):92A–99A, 1965.

[167] Dan Eklund. Pigment particle size–its significance in paper coating. *Cellulose chemistry and technology*, 1975.

[168] Hyun-Kook Lee, Margaret K Joyce, and Paul D Fleming. Influence of pigment particle size and pigment ratio on printability of glossy ink jet paper coatings. *Journal of imaging science and technology*, 49(1):54–60, 2005.

[169] Prakash B Malla and Siva Devisetti. High surface area aggregated pigments, 2002. US Patent 6,478,865.

[170] Brian Rand and Ian Eric Melton. Particle interactions in aqueous kaolinite suspensions: I. effect of ph and electrolyte upon the mode of particle interaction in homoionic sodium kaolinite suspensions. *Journal of Colloid and Interface Science*, 60(2):308–320, 1977.

[171] Peter Rättö, Hornatowska Joanna, Changhong Xiao, and Terasaki Osamu. Cracking mechanisms of clay-based and gcc-based coatings. *Nordic Pulp & Paper Research Journal*, 26(4):485–492, 2011.

[172] P Lepoutre and M Rigdahl. Analysis of the effect of porosity and pigment shape on the stiffness of coating layers. *Journal of materials science*, 24(8):2971–2974, 1989.

[173] Zhaohui Tong and Yulin Deng. Synthesis of water-based polystyrene- nanoclay composite suspension via miniemulsion polymerization. *Industrial & engineering chemistry research*, 45(8):2641–2645, 2006.

[174] Swati Gaur and AS Khanna. Functional coatings by incorporating nanoparticles. *Nano Research & Applications*, 1(1), 2015.

[175] Daeyeon Lee, Michael F Rubner, and Robert E Cohen. All-nanoparticle thin-film coatings. *Nano letters*, 6(10):2305–2312, 2006.

[176] Gerhard J Nohynek and Eric K Dufour. Nano-sized cosmetic formulations or solid nanoparticles in sunscreens: a risk to human health? *Archives of toxicology*, 86(7):1063–1075, 2012.

[177] Catia Contado and Antonella Pagnoni. Tio2 in commercial sunscreen lotion: flow field-flow fractionation and icp-aes together for size analysis. *Analytical chemistry*, 80(19):7594–7608, 2008.

[178] Shengyou Tan, Xihong Zu, Guobin Yi, and Xiaochun Liu. Synthesis of highly environmental stable copper–silver core–shell nanoparticles for direct writing flexible electronics. *Journal of Materials Science: Materials in Electronics*, 28(21):15899–15906, Nov 2017.

[179] Alexander Kamyshny and Shlomo Magdassi. Conductive nanomaterials for printed electronics. *Small*, 10(17):3515–3535, 2014.

[180] Dietrich Bertram and Horst Weller. Zwischen molekül und festkörper. *Physik Journal*, 1(2):48, 2002.

[181] Songlin Liu, Xiaoshan Fan, and Chaobin He. Improving the fracture toughness of epoxy with nanosilica-rubber core-shell nanoparticles. *Composites Science and Technology*, 125:132–140, 2016.

[182] Nadiim Domun, H Hadavinia, T Zhang, T Sainsbury, GH Liaghat, and S Vahid. Improving the fracture toughness and the strength of epoxy using nanomaterials–a review of the current status. *Nanoscale*, 7(23):10294–10329, 2015.

[183] Sijia Huang, Lian Bai, Milana Trifkovic, Xiang Cheng, and Christopher W Macosko. Controlling the morphology of immiscible cocontinuous polymer blends via silica nanoparticles jammed at the interface. *Macromolecules*, 49(10):3911–3918, 2016.

[184] Lian Bai, John W Fruehwirth, Xiang Cheng, and Christopher W Macosko. Dynamics and rheology of nonpolar bijels. *Soft Matter*, 11(26):5282–5293, 2015.

[185] Brendan P Dyett, Alex H Wu, and Robert N Lamb. Toward superhydrophobic and durable coatings: effect of needle vs crater surface architecture. *ACS applied materials & interfaces*, 6(12):9503–9507, 2014.

[186] Akira Nakajima, Kouki Abe, Kazuhito Hashimoto, and Toshiya Watanabe. Preparation of hard super-hydrophobic films with visible light transmission. *Thin Solid Films*, 376(1-2):140–143, 2000.

[187] SS Pathak and AS Khanna. Synthesis and performance evaluation of environmentally compliant epoxysilane coatings for aluminum alloy. *Progress in Organic Coatings*, 62(4):409–416, 2008.

[188] Shailesh K Dhoke, AS Khanna, and T Jai Mangal Sinha. Effect of nano-zno particles on the corrosion behavior of alkyd-based waterborne coatings. *Progress in Organic Coatings*, 64(4):371–382, 2009.

[189] Lily D Chambers, Keith R Stokes, Frank C Walsh, and Robert JK Wood. Modern approaches to marine antifouling coatings. *Surface and Coatings Technology*, 201(6):3642–3652, 2006.

[190] Steffen Pilotek and Frank Tabellion. Nanoparticles in coatings. *European Coatings Journal*, (4):170–179, 2005.

[191] Jiakuan Sun, Bhaskar V. Velamakanni, William W. Gerberich, and Lorraine F. Francis. Aqueous latex/ceramic nanoparticle dispersions: colloidal stability and coating properties. *Journal of Colloid and Interface Science*, 280(2):387 – 399, 2004.

[192] Henry Cohn, Abhinav Kumar, Stephen D Miller, Danylo Radchenko, and Maryna Viazovska. The sphere packing problem in dimension 24. *arXiv preprint arXiv:1603.06518*, 2016.

[193] David Boldridge. Morphological characterization of fumed silica aggregates. *Aerosol Science and Technology*, 44(3):182–186, 2010.

[194] Ludwig Wilhelmy. Ueber die abhängigkeit der capillaritäts-constanten des alkohols von substanz und gestalt des benetzten festen körpers. *Annalen der Physik*, 195:177–217, 1863.

[195] JB Cain, DW Francis, RD Venter, and AW Neumann. Dynamic contact angles on smooth and rough surfaces. *Journal of Colloid and Interface Science*, 94(1):123–130, 1983.

[196] Stefan Johansson, Fredric Ericson, and Jan-Åke Schweitz. Influence of surface coatings on elasticity, residual stresses, and fracture properties of silicon microelements. *Journal of Applied Physics*, 65(1):122–128, 1989.

[197] Andre Marcel Helbling, Michael Robert Hills, Friederike Theresia Stollmaier, and Thomas Martin Stephan Annen. Use of starch dispersions as binder in coating compositions and process for preparing the starch dispersions, November 30 2004. US Patent 6,825,252.

[198] Zegui Yan, Qiujuan Liu, Yulin Deng, and Arthur Ragauskas. Improvement of paper strength with starch modified clay. *Journal of Applied Polymer Science*, 97(1):44–50, 2005.

[199] Robert Billmers and Victor Mackewicz. Paper coating composition comprising a blend of modified high amylose starch and polyvinyl alcohol, 2002. US Patent App. 09/568,111.

[200] Roy L Whistler and James R Daniel. Starch. *Kirk-Othmer Encyclopedia of Chemical Technology*, 1978.

Appendix A

Cantilever Design for Thicker Coatings

A research project was to determine the drying stress of coatings with thickness ranged from 0.5 mm to 2 mm, while the available stress measurement was prepared for only thin coatings. So before the actual measurement, some preliminary work was done to make sure the theories and apparatus used in the thin coating stress measurement would still be valid in the thick coating measurement. In this appendix, the results of the viability check, the necessary modification, as well as the concerns and recommendations are discussed.

A.1 Theory

The current stress measurement used in our lab is the cantilever beam deflection method based on the Corcoran's work [2].

In addition to the assumptions discussed in Chapter 3.1.1, two more assumptions made by Corcoran during the equation derivation were discussed in this section before applying this equation to the thick coating measurement.

To simplify the calculation, the stress is considered to be concentrated in the center of the coating layer, which is fine when the coating layer is thin. However, it is worthwhile noting that strain is depth-depended when determining the thick coating stress. Using the relationship derived by Boerman and Perera [97], the Corcoran Equation (Equation

A.1) could be modified as presented below (Equation A.2).

$$\sigma = \frac{E_s t^3}{6c(t+c)(1-\upsilon_s)r} + \frac{E_c(t+c)}{2(1-\upsilon_c)r} \tag{A.1}$$

$$\sigma = \frac{E_s t^3}{6c(t+c)(1-\upsilon_s)r} + \frac{E_c(3t^2+6tc+4c^2)}{6(t+c)(1-\upsilon_c)r} \tag{A.2}$$

where E is the elastic modulus and υ is the Poisson ratio. The subscripts s and c denote the substrate and the coating layer, respectively. t and c represent the thickness of the substrate and the coating. and the average coating stress σ is related to the curvature of the coated substrate r.

Another assumption made by Corcoran [2] is that the modulus of the coating and the substrate are similar, which sets the position of the neutral axis, l, to be at the center of the total thickness as shown in Equation A.3.

$$l = \frac{t+c}{2} \tag{A.3}$$

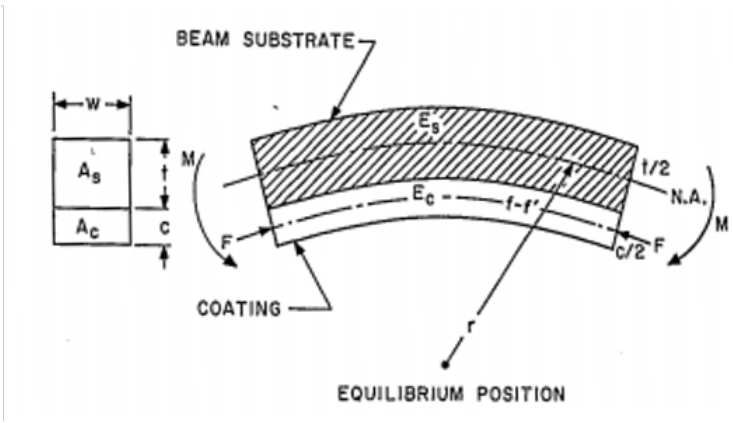

Figure A.1: Schematic diagram of the neutral axis position of the coated substrate in Corcorans work [2].

As shown in Figure A.1, with the increase of the coating thickness, the difference of the modulus would raise the deviation between the actual neutral axis and the center of the total thickness. According to Chiu [108], the actual neutral axis could be determined

using Equation A.4. Derived using actual neutral axis, we get modified Equation A.5. [112, 196]

$$l = \frac{E_s t^2 - E_c c^2}{2E_s t + 2E_c c} \tag{A.4}$$

$$\epsilon = \frac{D_e}{rc(l + \frac{c}{2})} + \frac{E_c^\star}{r(l + c/2)} \tag{A.5}$$

where:

$$D_e = \frac{1}{3}[E_s^\star(1 + \upsilon_s)t^3 + E_c^\star(1 + \upsilon_c)c^3] - l^2[E_s^\star(1 + \upsilon_s)t + E_c^\star(1 + \upsilon_c)c] \tag{A.6}$$

$$E_i^\star = \frac{E_i}{1 - \upsilon_i} \tag{A.7}$$

A.2 Apparatus

The current walled substrate used in the coating stress measurement has a dimension of 5 mm × 44 mm × 0.52 mm (width × length × thickness) with a 0.25 mm height PDMS wall. To be applied in the thicker coating measurement, other than increasing the height of the PDMS wall, the dimension of the substrate also needs to be modified. Several aspects are taken into consideration, for example, the edge effect of the stress distribution, the dimension of the PDMS wall, the length-width ratio of the substrate and the deflection limitation.

A.2.1 Edge Effect of the Stress Distribution

As discussed in Chapter 3.1.1, to ensure the measured stress is mainly contributed by in-plane stress, the width of the substrate need to be at least 2 unit of the coating thickness. Then the 2 mm-thick sample requires the actual coating area to be at least 4 mm wide.

A.2.2 Width of the PDMS Wall

Being able to hold the 2 mm thick coating, the PDMS wall should be at least the same height. Taken into consideration the extra height gained by cutting off the PDMS at the coating area, it is reasonable to set the depth of the wall-mold to be 2 mm. In order

to make sure the PDMS wall could be peel out of the mold, the width of the wall is chosen to be 1.5 mm. (Further modification may need)

A.2.3 Width-to-Length Ratio

The concern of choosing the length of the substrate was the curvature of the cantilever cross-section would affect deflection measurements between experiments if the laser was not accurately positioned to the center of the substrate. According to the work done by Payne [112], the width-to-length ratio reaches 0.2 when the edge deflection exceeds the midpoint deflection by greater than one percent in the case of 0.25 mm thick substrate. And the critical ratio increases with substrate thickness. To ensure no erroneous effects, the ratio of 18% is recommended.

A.2.4 Deflection Limitation

Taking all aspects mentioned above into consideration, we could set the dimension of the substrate to be 8 mm wide and 63.5 mm long, with the free length of 47.5 mm and clamping length of 16 mm, as shown in the Figure A.2 below.

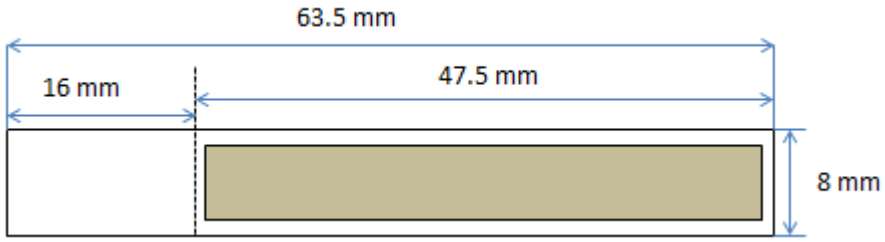

Figure A.2: Schematic diagram of substrate dimension. The actual coating area is indicated by shadow.

When the substrate curvature is estimated using the cantilever deflection, several approximations are made. A critical deflection value exists to limit the error caused by the approximation. The curvature of the cantilever and two-point-supported beam are shown in equation A.8 and A.8, respectively.

$$r = \frac{L^2}{2d} \tag{A.8}$$

$$r = \frac{L^2}{8d} \tag{A.9}$$

Where d is the deflection detected by the laser, and L is the length of the coating area as shown in Figure A.3. During the calculation, c is approximated to be equal to L in the cantilever case (L need to substituted by $L/2$ in case of two points supported case). With the deflection gets larger, the difference between L and c is increased. To limit the error within 0.1%, d needs to be less than $8\%L$, which is 3.8 mm in our case.

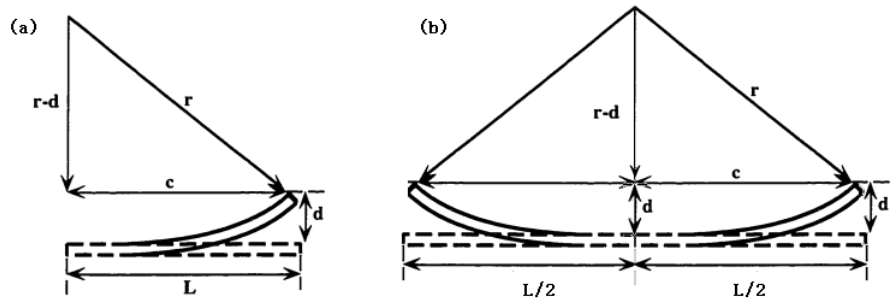

Figure A.3: Schematic diagram of curvature estimation of the cantilever beam and two-point-supported beam.

The plate theory used in equation A.5 also has the assumption of the small deflection [111], which is the deflection needs to be smaller than 10-25% of the substrate thickness. Thus, the deflection limitation decreases to 0.05 mm.

To get a better sense of the deflection of 0.05 mm, we could try to relate the stress value with this deflection magnitude by reversing the calculation. Using Equation A.5, with the modulus of the coating and the substrate to be 1.5 GPa and 170 GPa; Poissons ratio υ_s and υ_v to be 0.064 and 0.3; density of the sample to be 4 g/cm^3.

For a 2 mm-thick coating, deflection caused by its own weight is about 1.2 $\times 10^{-3}$ mm, which is 2.4% the total maximum deflection. To simplify the calculation, we assume all 0.05 mm deflection is caused by stress, and we get a stress value of 0.41 MPa while the typical drying stress of alumina coating is $1 \sim 2$ MPa. For the case of 0.5 mm thick coating, the corresponding stress to that maximum deflection would be 0.44 MPa.

Apparently, it is necessary to increase the substrate thickness used in this measurement. For the substrate with same properties but the thickness of 1 mm, the maximum

deflection increases to 0.1 mm. For the 2 mm-thick coating, the stress causing this much deflection is about 5.48 MPa.

In summary, the substrate whose dimension is shown in Figure A.2 could be used to test the thick coating stress. But the thickness of the substrate needs to be considered based on the maximum stress value.

A.2.5 Mechanical Properties

As shown in Equation A.5, the elastic modulus and Poissons ratio of the coating material are needed to estimate the drying stress. Different methods could be used to test the coating mechanical properties depending on the material. If a free-standing coating is available, vibrating membrane technology could be applied to test the elastic modulus value [109]. Otherwise, the modulus could be determined using the strain gages and DMA to get the strain difference between the coating and substrate [108]. Equation A.10 derived by Chiu enabled the estimation of the coating modulus.

$$E_c = E_s R \frac{KR + 2K - R}{2R - K + 1} \tag{A.10}$$

$$K = -\frac{\varepsilon_s}{\varepsilon_c} R = \frac{t}{c} \tag{A.11}$$

where ε is the strain detected by strain gage.

However, there is no direct approach found testing the Poissons ratio of the green ceramic body. The stress difference made by choosing different Poissons ratio values of 0.3 and 0.1 is approximately 10%. But as long as the same Poissons ratio is used through all the measurements, the relative stress change made by altering drying conditions would not be affected.

Considering the work presented above, it is recommended to start the experiment using 1 mm thick silicon substrate (8 mm $\times$ 63.5 mm) with 2-mm-high PDMS walls. Equation A.5 and Equation A.8 could be used to estimate the stress value from the cantilever deflection. Be aware of the maximum deflection, since the error of the measurement could be significantly increased if the cantilever displacement exceeding the 25% of the substrate thickness.

Appendix B

Shrinkage Data Analysis

By taking 800 data points per time frame, the shrinkage data obtained by measuring the 20-minute-drying of a coating is large. A Matlab code wrote by Tess Marconie, the undergraduate student at the University of Minnesota, was used to analyze the data [134]. The outputs include the coating thickness versus the time plot, shrink rate, initial thickness, and shrink time. The MATLAB codes and more explanation of the different inputs are shown in this Appendix.

Code used for analyzing shrinkage data measured by V orientation:

```
function F = shrinkageV(A,e,filename)

% Tess Marconie 2017
%   A is the matrix from the experiment. The first row of the matrix
%   contains the time values, each repeated twice (ex: 0 0 10 10 20 20).
%   In the 0 0 column is the plain substrate profile. Under each time
%   value is the profile from that time.
%   e is the number of points to be used to find the slope.
%   filename is the name of the .mat file that the outputs will save in.


B=A(2:end,4:2:end);

t=A(1,(3:2:end));

Y=zeros(size(t,2),size(B,1));
Y(:,1)=t;

for i=1:size(B,1)
 Y(:,i+1)=(B(i,:)-A(i+1,2))*1000;
end
```

```
for j=1:size(B,1)
 [v,w]=min(Y(:,j+1));
 st(j)=Y(w,1);
 P(j,:)=polyfit(Y(1:e,1),Y(1:e,j+1),1);
 f(j)=mean(Y((end-1):end,j+1));
 d(j)=P(j,2)-f(j);
end

shrinktime=mean(st);
sdshrinktime=std(st);
slope=mean(P(:,1))*60;
sdslope=std(P(:,1))*60;
thick=mean(f);
sdthick=std(f);
shrinkage=mean(d);
sdshrinkage=std(d);
intercept=mean(P(:,2));
sdintercept=std(P(:,2));

save(filename,'A','Y','shrinktime','sdshrinktime','slope','sdslope','th
ick','sdthick','shrinkage','sdshrinkage','intercept','sdintercept','e')
;

end
```

When using this code, first do one calculation with an arbitrary value of e. Then plot the shrinkage curve using the output Y from the code above in the code below. Determine which value of e should be used. Then, rerun the code.

```
function F = shrinkplotV(Y,filename)

s=(size(Y,1));
P=zeros(s,1);
P(:,1)=Y(:,1);

y = mean(Y(:,2:end),2);
P(:,2)=y;
plot(P);

plot(P(:,1),P(:,2),'o');

save (filename,'P')

end
```

Code used for analyzing shrinkage data measured by H orientation:

```
function F = shrinkageH(A,csg,cs,c1,c2,td,e,filename)

%Tess Marconie 2017
%   A is the matrix from the experiment. The first row of the matrix
%   contains the time values, each repeated twice (ex: 0 0 10 10 20 20).
%   In the 0 0 column is the plain substrate profile. Under each time
value
%   is the profile from that time.
%   For the variables csg, cs, c1, and c2, all x values from the profile
%   are numbered 1-800. Select the desired point and input the
%   corresponding number from 1-800.
%   csg is some point on the plain substrate profile where the height of
%   the platform can be determined.
%   cs is the center of the plain substrate.
%   c1 is some point on the timed profiles where the height of the
platform can
%   can be determined.
%   c2 is the center point of the drying coating.
%   td is the time difference from the times present in A, if necessary
%   e is the number of points to be used to find the slope.
%   filename is the name of the .mat file that the outputs will save in.

B=A(2:end,4:2:end);

t(:,1)=(A(1,(3:2:end))-td);

Y = zeros(size(t,1),2);
Y(:,1)=t;

s=(mean(A((cs-5):(cs+5),2))-mean(A((csg-5):(csg+5),2)))*1000;

for i=1:size(t)
 Y(i,2)=(mean(B((c2-10):(c2+10),i))-mean(B((c1-5):(c1+5),i)))*1000-s;
end

plot(Y(:,1),Y(:,2),'o');

P=polyfit(Y(1:e,1)/60,Y(1:e,2),1);

f=mean(Y(end-15:end));

[v,w]=min(Y(:,2));
st=Y(w,1);

d=P(2)-min(Y(:,2));

save(filename,'t','Y','P','f','d','st','A','c1','c2','td','e','s');

end
```

Appendix C

Effect of Starch and Nanoclay Additions on Drying of GCC Coatings with Latex

The effects of additives, alcogum (Alco) and polyvinyl alcohol (PVOH), were discussed in Chapter 4 [89]. Addition of Alco was found have no significant effect on the coating stress development, while PVOH significantly increased the coating stress. In this appendix, the results of investigating different additives, starch and nanoclay, are presented.

The compositions of three GCC-based coatings compared in this appendix are listed in Table C.1. Coating GGC-W is considered as a control sample to compare the effect of adding starch (denoted as S, Penford gum 290, Penford. Ethylated Starch) and nanoclay (denoted as N, Montmorillonite. Nanocor PGV. Diameter of 1 nm and plate diameter in the range of 200-250 nm. Shape factor around 200-250). GCC-W (Hydrocarb 60, Omya. Modal diameter of 2.5 μm, wide particle size distribution) is the same particles used in Chapter 4.

As the stress results listed in Table C.1, both of these additives increase the stress level, presumably by promoting shrinkage. Starch causes a more significant increase in the stress development of the GCC-latex sample comparing to nanoclay. SEM images (Figure C.1) show the microstructures of these three coatings, and stress development

curves are shown in Figure C.2.

Table C.1: Comparison of average stress for coatings prepared with GCC and SA latex with different particle size distribution.

Sample	GCC-W	SA	Starch	Nano-clay	Thickness (μm)	Stress (MPa)	Comment
W-SA	29.19	15.07			64.9 ± 6.6	3.41 ± 0.26	No defects (40μL)
					43.3 ± 9.4	4.29 ± 0.95	No defects (30μL)
W-SA-S	29.27	13.62	1.45		51.3 ± 8.9	12.28 ± 1.47	Cracks (30μL)
W-SA-N	27.97	15.07		1.34	68.6 ± 1.0	4.61 ± 0.96	no defects (40μL)

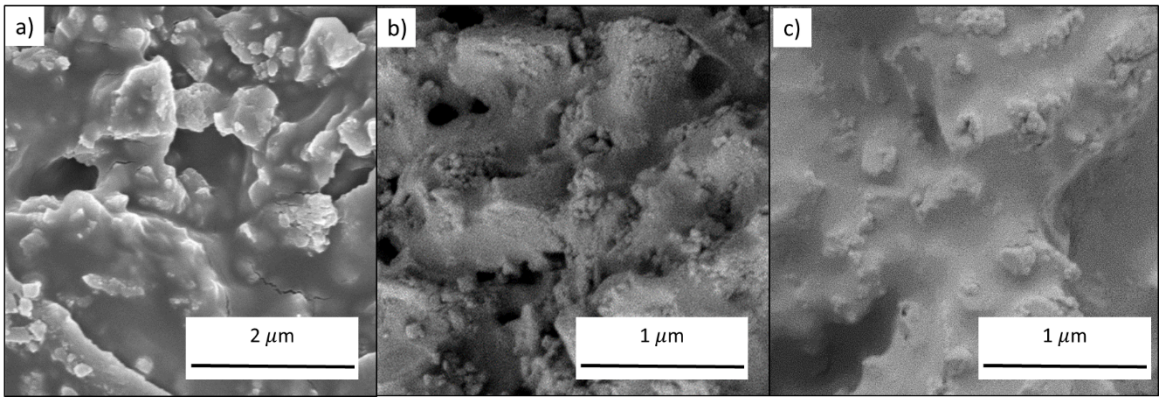

Figure C.1: SEM images of coating cross sections for GCC-W coatings with a) no additives (W-SA), b) starch added (W-SA-S) and c) nanoclay added (W-SA-N)

Very small amounts of nanoclay and starch appear to have significant effects on microstructure and stress. As shown in Figure C.1, the coatings with nanoclay added (Figure C.1c) appears to have smaller pores in between GCC particles compared to the coating with no additives (Figure C.1a). The reduced pore size may be responsible for the larger stress development; stress development data in Figure C.2 show an intermediate peak that is likely due to a capillary effect. Starch addition [197, 198, 199, 200] is known to affect coatings stability and viscosity. And it may be responsible for the higher stress values by enhancing shrinkage during drying. The data show that the starch-containing coating has the lowest dried thickness among all three coatings listed in Table C.1, indicating higher shrinkage. But dried thickness is not the most accurate

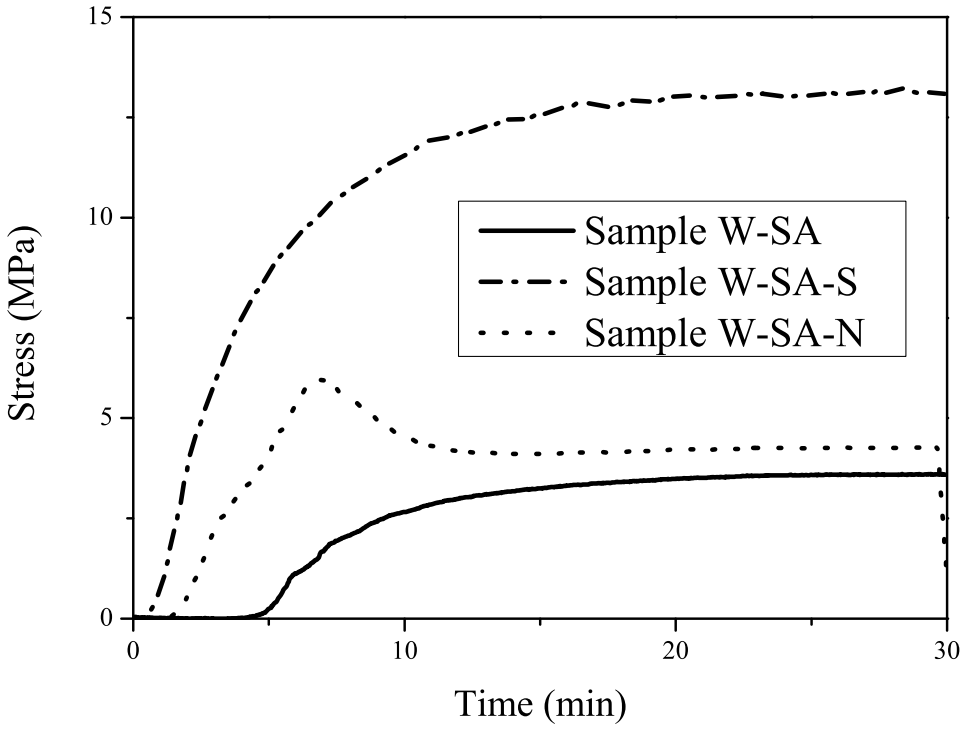

Figure C.2: Comparison of stress development curves of GCC-W coatings without additive (W-SA) with starch (W-SA-S) and nanoclay (W-SA-N). Stress curves measured using 40 μL of suspension volume of S-SA, 30 μL of suspension volume of W-SA-S, and 40 μL of suspension volume of S-SA-N.

way to characterize shrinkage and more work would be needed to verify the shrinkage effect. The stress development for the starch-containing coating shows continuous stress increase during drying, which indicates constrained shrinkage dominates the stress development.